RICE UNIVERSITY

Non Local Mechanics in the Time and Space Domain-Fracture Propagation via a Peridynamics Formulation: A Stochastic\Deterministic Perspective

by

Georgios I. Evangelatos

A THESIS SUBMITTED
IN PARTIAL FULFILLMENT OF THE
REQUIREMENTS FOR THE DEGREE

Doctor of Philosophy

APPROVED, THESIS COMMITTEE:

Pol D. Spanos, L.B. Ryon Professor of
Mechanical Engineering and Civil Engineering

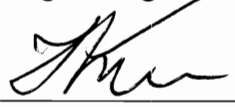

Ilinca Stanciulescu, Assistant
Professor of Civil Engineering

Andrew J. Dick, Assistant
Professor of Mechanical Engineering

Houston, Texas USA
April 2011

ABSTRACT

Non Local Mechanics in the Time and Space Domain-Fracture Propagation via a Peridynamics Formulation: A Stochastic\Deterministic Perspective

by

Georgios I. Evangelatos

Novel numerical methods for treating fractional differential and integrodifferential equations arising in non local mechanics formulations are proposed. For fractional differential equations arising in modeling oscillatory systems incorporating viscoelastic elements governed by fractional derivatives, the devised scheme is based on the Grunwald-Letnikov fractional derivative representation, dual time meshing technique and Taylor expansion. The proposed algorithm transforms the governing fractional differential equation into a second order differential equation with appropriate effective coefficients. The enhanced efficiency of the scheme hinges upon circumventing the calculation of the non local fractional derivative operator. Several examples of application are provided.

Further, the concept of non locality, specifically viscoelasticity, governed by fractional derivatives is utilized to accurately model polyester materials. Specifically, the linear standard solid (Zener model) is extended to capture non linear viscoelastic behavior. Then, experimental data of polyester ropes are utilized using the Gauss Newton and Levenberg-Marquart minimization algorithm to determine the model parameters.

Next, for integrodifferential equations arising in peridynamics theory of mechanics, an approach is formulated based on the inverse multi-quadric (IMQ)

radial basis function (RBF) expansion and the Kansa collocation method. The devised scheme utilizes interpolation functions and basis function expansion for the spatial discretization of the peridynamics equation. This significantly reduces the computational effort required to numerically treat the peridynamics equations. Further, the proposed method is extended to account for mechanical systems with random material properties operating under random excitation. For this, the stochastic peridynamics governing equation of motion is solved using the benchmark Monte Carlo analysis and tools of stochastic analysis. The stochastic analysis is done by numerical evaluation of the requisite Neumann expansion using pertinent Monte Carlo simulations.

Further, the usefulness of the radial basis function (RBF) collocation method in conjunction with a polynomial chaos expansion (PCE) is explored in stochastic mechanics problems. It is shown that the proposed approach renders further solution improvements in solving stochastic mechanics problems vis-a-vis the stochastic finite element method and the element free Galerkin method.

Acknowledgements

I would like to thank my research advisor and thesis committee chair Professor *Pol D. Spanos* for his mentorship during my graduate studies at Rice University. I am grateful, I had the opportunity to experience graduate studies in an environment of success that promoted innovative ideas and free thinking on a day to day basis. Further, the unrestricted academic freedom and the opportunity I had to focus on areas outside the ordinary taught me invaluable lessons both in my academic and personal life. For this life changing experience that he offered, I am thankful.

Thanks are also due to Professor *Ilinca Stanciulescu* for participating in the thesis committee and submitting constructive comments. Our extensive discussions on my work and her insight were particularly helpful. Her ideas and deep understanding of my work were particularly encouraging. Further, I would like to express my deep appreciation to Professor *Andrew J. Dick* for participating on my committee and providing me with insightful feedback.

I also want to thank all my professors and friends at Rice University for making my stay here an incredible, once in a life time, experience. Specifically, I like to thank my friends *Konstantinos Tsianos*, *Nikolaos Soultanidis, Konstantinos Bekris*, and *Agathoklis Giaralis* for our constructive interaction and endless discussions.

Furthermore, it is a great pleasure to express my true love and appreciation to my family for their unconditional love, support, encouragement and belief in me. Special thanks go to my brothers *Panagiotis Evangelatos* and *Dionisis Evangelatos* for all their efforts and struggles to support and help me achieve my full potential and realize my dreams. Thanks are also due to *Jessica Garcia* for her sincere love, care, patience and understanding. Last but not least, I want to express the infinite debt that I owe to my parents *Ioannis Evangelatos* and *Virginia Evangelatos*. Their vision, ideals, character and perseverance equipped me with an unparalleled desire and drive to realize my dreams; this thesis is dedicated to them.

Table of Contents

List of Figures

List of Tables

Chapter 1

Introduction

1.1 Thesis Perspective

Modeling material behavior has been one of the most important aspects of engineering. Indeed, theoretical models that capture material behavior under a variety of excitations are extremely important in designing buildings, aircraft, ships, and mechanical and structural components. Material modeling is usually based on experimental results and in some kind of linear/non linear regression method to identify the model parameters. In general, for materials of linear behavior that can exhibit purely viscous, elastic or viscoelastic behavior, the experiments are conducted in the frequency domain. However, for materials of non linear behavior, experimental results must be utilized both in the time and frequency domain. Specifically, non linear regression methods are used to accurately identify the model parameters. Further the identification of the most accurate model requires extensive experimental results.

Since the beginning of the 20^{th} century, purely viscous and purely elastic behavior of materials has been well studied. Specifically, viscous materials such as crude oil and honey resist shear flow, and the underlying shear stress depends linearly on the strain rate. For purely elastic materials the stress depends linearly on the applied strain. Therefore, extensive experiments quickly showed that some materials exhibit both behaviors and are called viscoelastic. Specifically, for such materials the strain is time dependent upon application of stress. Naturally, these

kinds of materials are frequency dependent, in the sense that, sinusoidal excitations of the same amplitude but of different frequency would change the strain response. Further, the purely viscous behavior is captured in the time domain as a linear function of the first derivative of the stress. In the frequency domain, this relationship is a linear function of the frequency. However, experiments on viscoelastic materials in the frequency domain showed that certain materials exhibit this linear relationship with respect to the frequency raised to a power, which is different than one. Specifically, this linear behavior has been exhibited for arbitrary powers of the frequency. Naturally, one can pose the question regarding the physical meaning of this in the time domain. In this context, the concept of fractional derivatives and fractional integrals is discussed herein.

Fractional calculus is the branch of mathematics that studies the possibilities of taking real or complex number powers of a differential operator. Leibniz has intuitively introduced the notion that, the operation of differentiation and integration can be construed as a parameter dependent, generalized non local operation which is equivalent to any linear operation for certain parameters. Specifically, the operation of differentiation in the classical calculus can be construed as the operation of integration of order negative one in the fractional calculus. Obviously, such a potent generalization can lead to operations of fractional order beyond those of positive or negative integer orders. In this regard, is has been known since the early 19^{th} century that the fractional order derivatives or integrals are represented in the frequency domain in terms of linear functions

with respect to fractional powers of the frequency. Obviously, this relationship between the fractional calculus and the fractional orders of the frequency in the frequency domain was utilized in modeling materials with frequency dependent behavior. Specifically, viscoelastic materials that behave, to a certain extent, viscously and elastically are accurately captured by fractional derivatives.

Naturally, the concept of non locality has been extended in the space domain. In local mechanics (Classical mechanics) theory, a single point in the domain is in direct contact with only its immediate neighbor points, and thus spatial derivatives exist in such a continuum. In non-local mechanics, however, a single point in the medium is under direct influence from points further away in addition to its immediate neighboring points. Non-local theories have been initially developed in the second half of the 20^{th} century, and since then several researchers have contributed to this concept. In a pioneering publication, Stewart Silling extended the concept of non-local mechanics (see Silling 2000). Until then, the non-locality concept was used as a generalization of the local mechanics, and assumed that spatial derivatives of a certain finite neighborhood around the point of interest can be used. He proposed a fully non-local modeling called peridynamics in which no spatial derivatives are needed, and therefore the inherent problem of a discontinuity in the domain can be circumvented. The model involves a formulation of a partial integrodifferential equation which holds for continuous and discontinuous domains with no additional treatment like enrichment etc.

Note that, peridynamics is a fully non-local approach. The first part of the name traces back to the Greek word 'περι' meaning around. In this context, this theory approximates the forces on a certain point by utilizing the deformations of a finite area around this point. Specifically, the infinitesimal volume represented by a point is assumed to be interacting with all the infinitesimal volumes around this point though 'bonds'. The concept of the bond is not an entirely novel idea; just as in molecular dynamics, the bond represents the interaction of two particles being in a predetermined distance which is called the horizon. Naturally, every point has infinitely many bonds that connect it to its neighboring particles. Any kind of external force that is applied on the reference body will deform the bonds and rearrange them in a new equilibrium state. The constitutive equation of each bond originates from the partial differentiation of a micro-potential function, representing the energy stored in the bond after every deformation. Due to the fact that the force equilibrium at each point yields an integral equation, and the infinitesimal mass has some predetermined density and exhibits acceleration, the governing equation of motion of peridynamics is a partial integrodifferential equation. Specifically, it is a second order differential equation with respect to time and an integral equation with respect to space.

Unlike classical continuum mechanics, peridynamics does not assume any continuity in the reference body. Classical mechanics assumes a continuous medium and thus the governing equation of motion is a partial differential equation with respect to both time and space. Naturally, the differential operation in discontinuous domains introduces singularities, and this is the reason why

classical mechanics has significant problems when it comes to fracture propagation or fracture initiation. However, due to the partial integrodifferential equation of peridynamics, no singularities are introduced when the reference body is discontinuous. The same equation holds for both cases; that is, whether the body is cracked or un-cracked.

Having established the governing equation, numerical methods can be employed to obtain an approximate solution. Specifically, the spatial discretization of partial integral and differential equations can be carried out using the finite elements method (FEM), the boundary elements method (BEM), element free Galerkin methods and collocation methods. The solution is obtained in the time domain utilizing a numerical time integration scheme such as finite differences method (FDM), Newmark, Runge Kutta etc. Mesh-free techniques present several advantages vis-a-vis the finite element method. Specifically, for the mesh-free methods no mesh is needed for the solution of the partial differential equation. Further, the solution obtained by mesh-free methods is continuous and differentiable in the entire domain of the solution due to the global support of the expansion basis. However, for mesh-free methods no rigorous convergence order estimates have been established. Thus, before the solution is accepted several other equations of the same kind need to be examined for the accuracy of the method to be established. Typically, the governing equations are not solved directly (strong form) and some technique is used such as weighted residual methods, Galerkin, Hamilton's principle etc, the strong form is transformed to a weak form. Weak forms are easier to solve due to their reduced

consistency demands. Specifically, a $2k^{th}$ differential equation requires a $2k^{th}$ consistency in its strong form solution. However, it requires only k^{th} order consistency in its weak form. This notion has been expanded in mesh-free methods with quite accurate results. In this regard, stochastic extension of such methods has been provided and their interesting properties have been presented in (Belytscko et all 2000, Rahmnan and Rao 2000, Rahman and Rao 2001). However, the Kansa collocation method has been proven quite recently a quite promising tool for solving partial, hyperbolic, parabolic and integral equations with notable accuracy while it allows for the advantages of the rest of the mesh-free methods to be retained (see Kansa 1990).

The Kansa collocation method directly solves the strong form equation by simply placing collocation points in the domain and imposing the strong form equation in each point. The solution is expanded on the radial basis functions and a set of arbitrary linear or non linear functions that must be compatible with the essential boundary conditions of the problem. Then, a linear set of algebraic equations is solved for the expansion coefficients. The solution on the domain is obtained by using the radial basis functions as interpolation functions in conjunction to the expansion coefficients. The method recently became a potent numerical mesh-free method due to the convergence order estimates for the radial basis functions (RBF) were rigorously introduced in (Franke and Schaback 1998). Further, the stability of the solution is guaranteed if the collocation nodes are distributed and not overlapping (Kansa 1990).

1.2 Problem statement

1.2.1 Viscoelasticity

Viscoelastic materials governed by fractional derivatives incorporated as constituents in oscillating structures fundamentally change the governing equation of motion of the system. The governing equation yields a linear/non linear fractional differential equation. Equations of this kind, present two main difficulties. First, the initial conditions are not displacements and velocities as it is the case of ordinary or partial differential equations. Initial conditions are functions that approximate the displacement of the oscillator before the application of the excitation and thus before t=0. Therefore, the initial conditions of fractional differential equations are functions which are called 'pre-histories'. Second, due to the non local property of the fractional operator, the computational cost of integrating in time a non linear fractional differential equation is of prohibitive difficulty. Specifically, equations governing the motion of multi-degree-of-freedom systems incorporating elements governed by fractional derivatives are quite computationally demanding to solve.

1.2.2 Modeling polyester ropes utilizing non linear viscoelasticity concept

The introduction of polyester mooring lines as permanent anchoring systems of offshore platforms and floating production storage and offloading vessels (FPSO) significantly reduced the costs of the construction of the anchored system. However, the design phase has been more complex due to the high non

linearity of the material. Specifically, the stiffness of polyester depends on the mean load, the amplitude and the frequency of the excitation. Further, for static loading the material exhibits permanent in-elastic deformation due to the construction creep. In this regard, there have been several efforts to model the stiffness of polyester using laboratory obtained experimental data. Extensive experiments on polyester yarns and strands clearly indicated hysteretic characteristics, fading memory effects, relaxation and frequency dependent behavior of polyester ropes. Also, it has been concluded that the effects of construction creep of the polyester are of significant importance, and the stiffness dependency on loading of high frequencies is less important than that of lower frequencies. Further, the polyester rope is becoming stiffer with increasing number of load cycles, and during storm cycling loads the viscoelastic-plastic effects are of significant importance since they introduce length recovery of the polyester rope. In this regard, a simple model is used by designers to capture the modulus of elasticity of polyester. In this model, the stiffness of polyester depends on the mean load, amplitude and period of the excitation. This model is accurate when pre-tension loading has been applied on the rope to effectively remove the construction stretch. Next, an accurate estimation of the static modulus of elasticity can be obtained since most of the deformation for static loads is fully recoverable. Obviously, the stiffness of the stretched rope will determine the offset of the anchored vessel under static loads induced by slowly changing currents. However, for dynamic loads such as wind and waves an accurate estimate of the polyester stiffness is needed, and since polyester exhibits non

linear frequency dependent behavior, non linear viscoelasticity concepts must be utilized.

1.2.3 Peridynamics theory of mechanics

In this chapter solid mechanics applications are considered with particular interest in fracture and crack propagation problems. Specifically, note that the problem of modeling dynamic or static systems that contain discontinuities is fundamental in mechanics. Fractured surfaces and propagating cracks are discontinuities which disrupt the domain of the differential equations and create mathematical singularities. There are several approaches to deal with these kinds of discontinuities. Two classical ones are the finite element method (FEM) with re-meshing of the continuous domain, and the extended finite element method (XFEM), which circumvents the constant re-meshing of the domain and uses the same mesh by simply adjusting the stiffness of the cracked element. However, all of these approaches have been based on local mechanics theory. In local mechanics theory, a single point in the medium is in direct contact with only its immediate neighboring points, and thus spatial derivatives exist in such a continuum. In non-local mechanics, however, a single point in the medium is in the region of influence of points further away in addition to its immediate neighboring points. Peridynamics is a fully non-local mechanics concept in which no spatial derivatives are needed, and therefore the inherent problem of a discontinuity in the domain can be circumvented. The model involves a formulation of a partial integrodifferential equation which holds for discontinuous

domains with no additional treatment like enrichment etc. The primary difficulty of the peridynamics formulation is attributed to the concept of the 'bonds'. Since 'bonds' are connecting only two infinitesimal volumes, the material is modeled as a Cauchy crystal (see Silling 2000) and thus has a fixed Poisson ratio of ¼. This presents a severe limitation in the bond based formulation of peridynamics. Also, another difficulty introduced by the integrodifferential equation is imposing the boundary conditions. Since only bonds exist in the modeled body, the typical fixed rotations, displacements etc, are now significantly more difficult to implement. In addition, the computational cost of forming all the necessary bonds and of solving for the displacements is significantly higher than those of any other method such as FEM or Meshless Galerkin etc.

1.2.4 Stochastic mesh-free methods

In the preceding regard, mechanical systems involving stochastic parameters are considered in this chapter. Particular attention is devoted to the computational tools for the treatment of the underlying stochastic differential equations. Specifically, the stochastic finite element method and stochastic mesh-free methods are considered. In many respects, the finite element method (FEM) revolutionized the field of applied mechanics and the manner in which solutions of ordinary and partial differential equations are obtained. The finite element method is a powerful computational tool that can treat static/dynamic and linear/nonlinear problems and is used in diverse areas of engineering and applied mathematics. Of course, there are two major challenges in dealing with the FEM.

First, the domain of the differential equation must be discretized in smaller parts, and usually the more refined the discretization is, the better the solution becomes. Further, in many problems the meshing of the domain is a much more copious step of the method than the solution step of the problem. Second, once the domain is discretized and the solution is obtained at the nodes, displacements and derivatives inside the discretized domain are obtained from the shape functions and the nodal displacements. However, continuity across element boundaries is not guaranteed for all fields of interest. These two major challenges have been addressed in the formulation of meshless techniques, where the Galerkin approach and collocation methods are introduced and the shape functions are spanning the entire domain. For this, nodes are distributed inside the domain at the points of interest and the solution on the points is expanded on the basis functions. This formulation leads to an equivalent stiffness matrix of the degrees of freedom represented by the nodes and circumvents the laborious meshing of the domain. For stochastic problems, however, the difficulty of inverting the random stiffness matrix remains. Indeed, the difficulty of meshing the random field has been circumvented by using mesh-free methods. However, since the stiffness matrix inversion is a non linear operation, Monte Carlo simulations are still needed for determining the statistics of the response.

1.3 Thesis Outline

The thesis comprises seven chapters, two appendices A and B and the cited publications list. Figures and tables are shown at each chapter at the point of reference in the text and lists of figures and tables are included in the manuscript after the table of contents.

Chapter 1 provides an introduction to the thesis and outlines the motivation, the objectives, and the importance of this research effort. Specifically, it includes a summary of viscoelasticity, frequency dependence and material modeling. In this context, the difficulties in modeling polyester materials and the importance of their applications are discussed. Next, it introduces the fully non local peridynamics theory, its advantages in modeling discontinuities, and its disadvantages when it comes to the numerical solution of the underlying governing equations. Finally a discussion is included on the mesh-free methods and their potential extensions to treat stochastic mechanics problems.

Chapter 2 provides an introduction to fractional derivatives and their applications in modeling viscoelastic, frequency dependent materials. In this context, the representations of fractional derivatives in the frequency and in the time domain are presented. Then, the utility of the Grunwald-Letnikov representation is shown in the benchmark time integration algorithm G1. This algorithm is used to integrate in time linear/non linear fractional differential equations. Equations of this kind arise in oscillating systems which comprise viscoelastic elements governed by fractional derivatives. Next, an accelerated numerical integration scheme is devised to accurately solve non linear fractional

differential equations in the time domain. Extensive numerical simulations are presented to prove the convergence of the proposed numerical scheme. Also, simulations of linear and non linear single-degree-of-freedom systems under earthquake excitation are considered, with results supporting the effectiveness of the devised scheme.

Chapter 3 is devoted to utilizing the experience gained by the studies of non linear fractional differential equations and fractional calculus to model polyester ropes used in the oil and gas industry. There lines are used for station keeping of offshore platforms and floating production systems. In this context, an introduction is included to understand the problem arising from using polyester instead of steel or chain as anchoring systems. Then, real 'in service' data of an offshore platform operating in the Gulf of Mexico during the Hurricane Katrina and Rita are used to establish and solve an inverse identification problem. The identification problem involves the determination of the static modulus of elasticity of polyester ropes. Next, a non linear viscoelastic model is used to capture the polyester behavior, and pertinent data are used to determine the model parameters. Numerical simulations of the proposed scheme vis a vis the laboratory experimental results of polyester ropes are considered. The results clearly demonstrate the effectiveness this approach.

Chapter 4 is dedicated to introducing the concept of non locality in the space domain. Specifically, the fully non local peridynamics theory of mechanics is introduced and its superior capability in modeling fracture is discussed. Then, the bond based peridynamics theory is used to model a crack propagation problem

for both deterministic and stochastic excitations. Next, a potent spatial discretization method is introduced for the discretization of the partial integrodifferential equation arising from the peridynamics modeling. Further, an extension to the bond based method is presented to resolve the Poisson ratio limitations arising from the ordinary bond based peridynamics theory.

Chapter 5 considers deterministic and stochastic examples to demonstrate the effectiveness of the proposed approach and the effectiveness of the peridynamics theory in modeling propagating cracks. Also, examples are presented to show the capability of the proposed spatial discretization of the peridynamics theory for treating probabilistically propagating cracks.

Chapter 6 introduces the mesh-free Galerkin and collocation methods. It discusses their effectiveness when dealing with mechanical components where the mesh is a complex process, and elaborates on the advantages of mesh-free methods. Then, the Kansa collocation method is extended to treat stochastic differential equations arising from systems of stochastic material properties operating under deterministic or stochastic excitations. Numerical results are presented to illustrate the effectiveness of the Kansa collocation method in conjunction with the polynomial chaos and Neumann expansion.

Chapter 7 has the concluding remarks of this work, and discusses future extensions and possible applications. In this regard, first, it presents the directions in the research field of fractional differential equations and their applications in modeling real materials with complex behavior. Second, it elaborates on the extension of linear models to non linear models of viscoelasticity. Third, it points

out the advantages of using peridynamics in modeling fracture initiation or fracture propagation. Finally, it discusses the potential gains of using mesh-free techniques for treating stochastic problems and specifically the advantages rendered by the Kansa collocation method.

Finally, the first appendix pertains to the offshore platform application. The second describes the novel spatial discretization method devised herein for solving the partial integrodifferential equations arising from the peridynamics formulation. Specifically, the proposed numerical integration scheme for the stiffness determination, the Kansa collocation method, and the implicit assumptions of the linear peridynamics theory are outlined.

Chapter 2

Fractional Calculus

2.1 Introduction

For several decades it has been known that the behavior of certain materials can be modeled accurately by using the concept of fractional derivatives. Specifically, in the beginning of the 20th century Nutting (1921) observed that the stress relaxation of such materials can be modeled by fractional powers of time, and Gemant (1936) stated that, the stiffness and damping properties of viscoelastic materials can be represented properly by using fractional powers of frequency.

Gemant (1936) specifically suggested the use of fractional derivatives in the constitutive equation of materials. Scott-Blair (1949) suggested the application of fractional derivatives of time to reproduce the observations of Nutting (1921) and Gemant (1938). Further Caputo (1974) reported a good agreement with experimental results when he used fractional derivatives for the description of the behavior of viscoelastic materials. For most of the 20th century the option of using fractional derivatives in conjunction to viscoelasticity was more of a curve fitting tool. Next, Bagley and Torvik (1986) offered a physical foundation of this concept. Subsequently, the use of fractional derivatives to model viscoelasticity was commonly advocated in (Galucio et all 2004; Bossemayer 2001; Adolfson et all 2005). Also the fractional derivative viscoelastic model was used to characterize the frequency dependent complex moduli of elastomers (see Lu 2006); and a quite good correlation between testing and prediction was reported.

In recent years, the concept of fractional operator has been incorporated in many other engineering applications. For instance, fractional Fourier transform was considered in the optics and the signal processing research communities (see Almeida 1994; Namias 1998; Pei et all 1999). Furthermore, the concept of fractional dimension was used to represent other data such as those pertaining to coastlines, clouds, particles of dust in the air, the network of neurons in the human body, and to pattern recognition and data classification (see Barnsley 1988). Also, the concept of fractional lower-order statistical moments was used to study non-Gaussian processes in signal processing applications (see Chao and Nikias 1993). Another application of the fractional derivative concept pertains to the case of fading memory materials. That is, in the case in which the stress does not depend only on the current strain but also on the previous strain history. This occurs in such a manner that the current stress depends more critically on the recent strain history than on the distant strain history (see Enelund and Olson 1999). Further, a diffusion equation of fractional order was proposed to model fluid infiltration in porous media (see Gerolymatou and Vardoulakis 2006); as well as, in modeling viscoelastic fluids having fractional order derivatives in their constitutive equations. Fluids of this nature are used as primary components of dampers and their hysteretic behavior is accurately captured by the use of fractional derivatives (see Makris et all 1993).

Finally in terms of modeling, in seismic base isolation techniques the application of fractional derivatives to viscoelasticity was first introduced (see Koh and Kelly 1990), and extensive research in viscous damping models was

reported (Makris 1994; Makris and Constantinou 1991; Makris and Constantinou 1992). Further, high damping rubber dampers are common in structural mechanics applications, and the option of employing generalized derivatives to capture the hysteretic behavior of such materials was proven quite successful (see Hwang and Wang 1998). Furthermore, modeling non linear rate dependent materials such as asphalt mixtures (see Wenbiao et all 2010; Darabi et all 2011), polyethylene, carbon black filled rubber (see Ciambella 2010), soft tissue (see Ciambella 2010), dry isotropic soils (Ciambella 2010) and polymeric materials (see Ayoub 2010) was quite successful.

Several studies have been reported describing various approaches to represent numerically fractional derivatives. Depending on the individual approach selected, the particular algorithms vary. Algorithms incorporating the Caputo representation (Podlubny 1999) may utilize a composite trapezoid rule to make calculations efficiently and reliably (Zaid 2006; Murio 2006), and were used in solving linear multi term fractional differential equations (Katsikadelis 2009; Shitikova 2001). Algorithms implementing the Riemann Liouville and Grunwald Letnikov (Podlubny 1999) representation were developed to solve fractional differential equations governing the motion of oscillatory systems (Koh and Kelly 1990; Makris and Constantinou 1992).

In this regard, a new efficient algorithm for numerical integration of the equation of motion of non linear systems with restoring forces governed by fractional derivatives in the time domain is devised herein. This approach is based on the Grunwald-Letnikov representation of a fractional derivative and on the

well known Newmark numerical integration scheme for structural dynamic problems. A Taylor expansion is used at every time step to represent the near past terms of the solution; thus a dual mesh of the time domain is introduced, the coarse mesh is used for the time integration and the fine mesh is used for the fractional derivative approximation. It is shown that with this formulation the problem yields an equivalent non linear system without fractional terms which involves effective values of mass, damping, and stiffness coefficients as a predictive approach and a correction on the excitation. The major advantage of this approach is that, a rather small number of correction terms are required for the numerical propagation of the solution, and the calculation of the effective values of mass damping and stiffness is performed only once.

2.2 Fractional Derivatives

In many respects the concept of fractional derivatives can be associated with the generalization of the factorial function. Specifically, Euler's gamma function defined the factorial for non integer and complex numbers. There are three representations of fractional derivatives with various advantages and disadvantages. Prior to proceeding to pertinent equations, certain symbols are introduced.

The α order differentiation of the function f with respect to time is denoted by the symbol $D^{\alpha}_{\beta,t} f(t)$, where β, t are the two limits related, or as defined in (Oldham and Spanier; Podlubny 1999; Miller and Ross), the terminals. The value α can be positive or negative and it is the order of integration or

differentiation depending on the sign. Specifically, when α is positive the symbol represents differentiation of the function, and when α is negative it represents integration of the function. In fact, the fractional integration of a function is defined as the convolution integral of the function f with the function t^p and can be written in the form:

$$D_{0,t}^{-a}x(t)=\frac{1}{\Gamma(a)}\int_0^t(t-\tau)^{a-1}x(\tau)d\tau \quad . \qquad (2.1)$$
$$a>0$$

In the preceding context, next, several alternative representations of the fractional derivative of order α (alpha) can be given.

First the Riemann-Liouville representation involves the equation

$${}_{RL}D_{0,t}^{a}x(t)=\frac{1}{\Gamma(m-a)}\frac{d^m}{dt^m}\int_0^t(t-\tau)^{m-a-1}x(\tau)d\tau\,, \qquad m-1\le a<m\in Z^+$$

(2.2)

where Z^+ denotes the set of real positive numbers.

An interpretation of the scheme of Equation (2.2) can be that in order to determine this derivative, the function x(t) is integrated $(m-a)$ times and then it is differentiated m times. That is,

$$\frac{d^m}{dt^m}D_{0,t}^{-(m-a)}x(t)={}_{RL}D_{0,t}^{a}x(t)\,. \qquad (2.3)$$

Second, the Caputo's representation can be cast in the form

$${}_{C}D_{0,t}^{a}x(t)=D_{0,t}^{-(m-a)}\frac{d^m}{dt^m}x(t)=\frac{1}{\Gamma(m-a)}\int_0^t(t-\tau)^{m-a-1}x^{(m)}(\tau)d\tau\,, \qquad (2.4)$$

where $x^{(m)}$ represents the m order derivative of the function x(t).

Third, the Grunwald-Letnikov representation can be cast in the form

$$ {}_{GL}D^{a}_{0,t}x(t) = \sum_{k=0}^{m-1} \frac{x^{(k)}(0)t^{-a+k}}{\Gamma(-a+k+1)} + \frac{1}{\Gamma(m-a)} \int_{0}^{t} (t-\tau)^{m-a-1} x^{(m)}(\tau) d\tau \qquad (2.5) $$

$m-1 \le a < m \in Z^{+}$

Expanding the series in Equation (2.5) yields

$$ {}_{GL}D^{a}_{0,t}x(t) = \lim_{h \to 0} h^{-a} \sum_{k=0}^{n} (-1)^{k} \binom{a}{k} x(t-kh). \qquad (2.6) $$

It is seen that the only difference between the RL and the C derivative definitions is the sequence of the differentiation. Specifically, in the Caputo's case, first the function is differentiated (m) times and then it is integrated $(m-a)$ times, whereas in the RL case the function is integrated $(m-a)$ and then it is differentiated (m) times. Next, adopting the representation of Equation (2.6) yields

$$ {}_{GL}D^{a}_{0,t}x(t) = \lim_{h \to 0} h^{-a} \sum_{k=0}^{N} GL^{(a)}_{k} x(t-kh), \qquad (2.7) $$

and

$$ GL^{(a)}_{k} = (-1)^{k} \binom{a}{k}; \qquad (2.8) $$

Equation (2.8) represents the Grunwald Letnikov (Grunwald 1867) coefficients formula, with the factorial symbol defined by the equation

$$ (-1)^{k} \binom{a}{k} = (-1)^{k} \frac{a(a-1)(a-2)(a-3)...(a-k+1)}{k!}. \qquad (2.9) $$

Manipulating Equation (2.9) and using the Gamma function property

$$\Gamma(z) = z\Gamma(z-1), \tag{2.10}$$

yields a recursive form for the evaluation of the GL coefficients. That is,

$$GL_k = \frac{\Gamma(k-a)}{\Gamma(-a)\Gamma(k+1)} = \frac{k-a-1}{k}\frac{\Gamma(k-a-1)}{\Gamma(-a)\Gamma(k)} = \frac{k-a-1}{k}GL_{k-1}. \tag{2.11}$$

Note that by definition, $\binom{a}{0} = 1$. Thus, the first GL coefficient is known

$GL_{k=0} = 1$.

Further, it is clear that $\frac{k-a-1}{k} < 1$ which justifies the 'fading memory' property of the fractional derivatives.

Note that, an efficient computation of the fractional derivative of a function can be achieved using the frequency domain. In this regard, the fractional derivative of order α of the function x(t) yields

$$D^{a}_{-\infty,t}x(t) = \frac{1}{2\pi}\int_{-\infty}^{+\infty}(i\omega)^{\alpha}X(\omega)e^{i\omega t}d\omega, \tag{2.12}$$

where

$$X(\omega) = \int_{-\infty}^{+\infty}x(\tau)e^{-i\omega\tau}d\tau. \tag{2.13}$$

2.3 Benchmark Integration Algorithm

Obviously the modeling versatility of the concept of fractional derivatives can be utilized further upon developing schemes for dynamic analyses of systems endowed with fractional derivative terms. In this context, next, a non linear single- degree- of- freedom system is considered, with damping forces governed

by fractional derivatives. Specifically, the equation of motion of a single degree of freedom non linear oscillator is given by the equation

$$m\ddot{x} + cD^{a}_{0,t}x + q(x) = f(t), \tag{2.14}$$

where m is the mass coefficient, and c is a constant which can be viewed as a damping coefficient if α is equal to 1 or as a stiffness coefficient if α is equal to 0; q is the nonlinear restoring force, and f(t) is the exciting force. Given the f(t) it is sought to determine the time history x(t) of the system response. For this purpose time axis is divided in N segments of length

$$\Delta t = \frac{T}{N}, \tag{2.15}$$

and two consecutive steps are considered, the (i+1) and the i step. Subtracting from the i+1 equation of equilibrium the i equation yields.

$$m\Delta\ddot{x}_i + c({}_{GL}D^{a}_{0,t_i}x_i - {}_{GL}D^{a}_{0,t_{i-1}}x_{i-1}) + \Delta q(x)_i = \Delta f_i, \tag{2.16}$$

where

$$\Delta x_i = x_{i+1} - x_i \ . \tag{2.17}$$

Combining Equation (2.7) and Equation (2.16) yields the equation of motion for the (i+1) step. That is,

$$m\Delta\ddot{x}_{i+1} + c\Delta t^{-a}\left(\sum_{k=0}^{i+1} GL_k x(t_{i+1} - k\Delta t) - \sum_{k=0}^{i} GL_k x(t_i - k\Delta t)\right) + \Delta q(x)_{i+1} = \Delta f_{i+1} \tag{2.29}$$

.

Introducing the term P

$$P = \left(\sum_{k=0}^{i+1} GL_k x(t_{i+1} - k\Delta t) - \sum_{k=0}^{i} GL_k x(t_i - k\Delta t) \right), \tag{2.30}$$

and expanding the series for the fractional derivatives one obtains

$$P = GL_0 \Delta x_{i+1} + GL_1 \Delta x_i + GL_2 \Delta x_{i-1} + \ldots + GL_i \Delta x_1 + GL_{i+1} x_0 . \tag{2.31}$$

Note, that the last term of P stands alone since its counterpart does not have the same GL coefficient. Further, P can be cast in the form

$$P_k = \sum_{k}^{i} GL_k \Delta x_{i+1-k} + GL_{i+1} x_0 . \tag{2.32}$$

Note that P_1 is known since it represents the linear combination of the GL terms with all the previous steps. Combining Equation (2.29) and (2.30), moving P_1 to the right hand side and keeping the first term $GL_0 \Delta x_{i+1}$ in the left hand side with the rest of the unknowns yields

$$m\Delta \ddot{x}_{i+1} + c\Delta t^{-a} GL_0 \Delta x_{i+1} + \Delta q(x)_{i+1} = \Delta f_{i+1} - c\Delta t^{-a} P_1 . \tag{2.33}$$

Combining Equation (2.32) and (2.33) yields

$$m\Delta \ddot{x}_{i+1} + (c\Delta t^{-a})\Delta x_{i+1} + \Delta q_{i+1} = \Delta p_{i+1}, \tag{2.34}$$

where

$$\Delta q_{i+1} = q(x_{i+1}) - q(x_i), \tag{2.35}$$

and

$$\Delta p_{i+1} = \Delta f_{i+1} - c\Delta t^{-a} P_1 . \tag{2.36}$$

The described procedure combines the truncated Grunwald-Letnikov fractional derivative approximation (G1-Algorithm) (Podlubny 1999; Oldham and Spanier;

Miller and Ross 1993) with the Newmark algorithm. The main advantage of this approach is that the non linearity is readily handled by Newton-Raphson iterations (see Spanos and Evangelatos 2010). Note that in the pioneering work of Koh and Kelly (1990) the fractional derivative was represented by the Riemann-Liouville formula and the final form is quite similar to Equation (2.34); the GL coefficients in the term P are weights arising from estimates of the integrals shown in Equation (2.2). In a similar manner the problem was addressed in Makris (1994) where the G1-algorithm has been used with quite good results, vis a vis frequency domain solutions, for linear elastic systems. Further note, that the solution for linear viscoelastic systems involving the generalized Kelvin and Maxwell models with fractional parameters was determined using the Laplace integral transform (see Rossikhin and Shitikova 2001). In (Makris and Constantinou 1991; Makris and Constantinou 1992) the non linear case of viscous models was addressed.

2.4 Accelerated Numerical Integration

Consider the time domain discretized in two separate meshes; one coarse mesh for the Newmark time integration scheme, and one fine mesh for the fractional derivative estimation. The integration step is of length Δt and is shown in Figure (2.1) as the interval between the tall vertical lines. The step of length h is the fine mesh and is the interval between the short vertical lines, each time step

of length Δt includes p steps of length h, thus $\Delta t/h=p$, Figure (2.1) helps visualize the dual meshing technique.

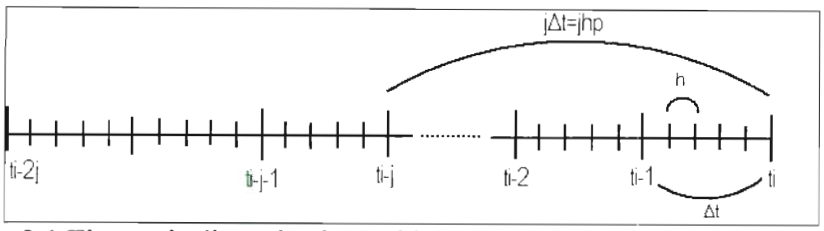

Figure 2.1 Time axis discretization, with both the integration time step and the fractional derivative estimation mesh.

The accelerated algorithm is based on representing the past terms needed for the Grunwald-Letnikov approximation of the fractional derivative at one point by the Taylor expansion of the same point in time. Since, the Newmark scheme determines the displacement velocity and acceleration at each time step, a Taylor expansion can be performed for at least up to second order terms. However, the range of an accurate approximation is limited and is shown in Figure (2.1) as $j\Delta t$; therefore, it is assumed that a small number j of previous steps can be accurately captured by a Taylor expansion, and since several past terms are needed for an accurate approximation, more than one Taylor expansions are needed. The overall number of past terms needed for the fractional derivative estimation is denoted by kj and, thus, k Taylor expansions are needed.

2.4.1 Numerical integration scheme

Next, consider a non linear fractional differential equation representing the equation of motion of a single degree of freedom system under an arbitrary excitation. Specifically,

$$m\ddot{x} + g(x^{(\alpha)}) + q(x) = f(t), \tag{2.37}$$

where g and q denote the arbitrary functions representing the restoring forces from the viscoelastic and elastic elements and m the mass of the oscillating system. Clearly considering the equation of motion at two consecutive time instants i+1 and i one derives

$$m\Delta\ddot{x}_i + \Delta g(x^{\alpha})_i + \Delta q(x)_i = \Delta f_i, \tag{2.39}$$

where, Δx_i is given by Equation (2.17) and the time step is given by Equation (2.15).

Using the secant stiffness coefficient during this small time step, Equation (2.39) yields

$$m\Delta\ddot{x}_i + K_i^g \Delta x_i^{(a)} + K_i^q \Delta x_i = \Delta f_i, \tag{2.41}$$

where K_i^g, K_i^q denote the secant stiffness coefficients at time step i from the non linear functions g and q respectively. Note that the time step Δt is much larger than the step h of the fine mesh and therefore, $\frac{\Delta t}{h} = p$ where p>>1. Next, adopting the Grunwald-Letnikov representation of the fractional derivative and using Equation (2.7) in the fine mesh one derives the vector inner product form,

$$x_i^{(a)} = h^{-\alpha}\begin{bmatrix} GL_0^{(\alpha)} & \dots & GL_{kjp}^{(\alpha)} \end{bmatrix}\begin{bmatrix} x_i \\ \dots \\ x_{i-p} \\ \dots \\ x_{i-2p} \\ \dots \\ x_{i-kjp} \end{bmatrix}, \tag{2.42}$$

where, p is the number of past terms of length h in a time integration step of length Δt. The number j represents the previous time steps of length Δt that can be approximated accurately by a backwards Taylor expansion using the displacement, velocity and acceleration at a certain time step i. Note that, the number k represents the overall chunks of j time steps that must be taken into consideration to accurately approximate the fractional derivative at a given point. Proceeding to approximating the j*p*h past terms which are of time length jΔt, using a Taylor expansion one can obtain those terms utilizing the displacement, velocity and acceleration at a given time step i. The Taylor backwards expansion yields the first jΔt past terms with respect to the current step x_i. Specifically,

$$x_{i-1} = x_i - h \cdot x_i^{(1)} + h^2/2 \cdot x_i^{(2)} + O(h^3) \tag{2.43a}$$

$$x_{i-2} = x_i - 2h \cdot x_i^{(1)} + 4h^2/2 \cdot x_i^{(2)} + O(h^3) \tag{2.43b}$$

$$x_{i-3} = x_i - 3h \cdot x_i^{(1)} + 9h^2/2 \cdot x_i^{(2)} + O(h^3) \tag{2.43c}$$

$$x_{i-jp} = x_i - jph \cdot x_i^{(1)} + j^2p^2h^2/2 \cdot x_i^{(2)} + O(h^3), \tag{2.43d}$$

where the number inside the brackets represents the order of the derivative and the power of the time step h respectively. The set of Equations (2.43) can be cast

in a matrix form, and assuming that the $O(h^3)$ can be truncated since the mesh of the time axis for the estimation of the fractional derivative is fine and the past terms $jph << 1$ is quite small, yields

$$\begin{bmatrix} x_i \\ x_{i-1} \\ x_{i-2} \\ x_{i-3} \\ \cdots \\ x_{i-jp+1} \end{bmatrix} = \begin{bmatrix} 1 & 0 & 0 \\ 1 & -h & h^2/2 \\ 1 & -2h & 4h^2/2 \\ 1 & -3h & 9h^2/2 \\ 1 & \cdots & \cdots \\ 1 & -(jp-1)h & (jp-1)^2 h^2/2 \end{bmatrix} \begin{bmatrix} x_i \\ x_i^{(1)} \\ x_i^{(2)} \end{bmatrix}. \tag{2.44}$$

In the same manner the displacements from the step i-jp to the i-2jp+1 can be cast in a matrix form in terms of the displacement, velocity and acceleration of the i-jp step. Equation (2.44) yields the relationship of these past terms to the Taylor expansion matrix, herein called connectivity matrix, and the displacement, velocity and acceleration of the given step. The same approach can be followed for all the past terms until the i-kjp term. However, it is possible to include higher order derivatives than the acceleration. This can be proven quite helpful in approximating more past terms. Thus, the connectivity matrix of the remaining past terms will have one more column if one selects to include the jerk in the computation. Equation (2.45) helps to elucidate this concept.

$$\begin{bmatrix} x_{i-jp} \\ x_{i-jp-1} \\ x_{i-jp-2} \\ x_{i-jp-3} \\ \cdots \\ x_{i-2jp+1} \end{bmatrix} = \begin{bmatrix} 1 & 0 & 0 & 0 \\ 1 & -h & h^2/2 & -h^3/6 \\ 1 & -2h & 4h^2/2 & -8h^3/6 \\ 1 & -3h & 9h^2/2 & -27h^3/6 \\ 1 & \cdots & \cdots & \cdots \\ 1 & -(jph-1) & (jp-1)^2 h^2/2 & -(jp-1)^3 h^3/6 \end{bmatrix} \begin{bmatrix} x_{i-j} \\ x_{i-j}^{(1)} \\ x_{i-j}^{(2)} \\ x_{i-j}^{(3)} \end{bmatrix} \tag{2.45}$$

Note, that the connectivity matrix is of dimensions jp x 3 for the first p terms, and of dimensions jp x 4 for the rest of the past terms if someone includes the jerk. Furthermore, note that the connectivity matrix is constant through out the time integration and it is once built in the beginning. These constant connectivity matrices are called H_0 and H. It can be seen that every set of j past steps of length Δt can be obtained in terms of the matrices H_0, H and the displacement, velocity and acceleration of the underlying time steps. Substituting Equation (2.44), (2.45) etc into Equation (2.42) one obtains

$$x_i^{(a)} = h^{-\alpha}\left[1 \quad .. \quad GL_{jp-1}^{(\alpha)}\right]\left[H_0\right]\begin{bmatrix} x_i \\ x_i^{(1)} \\ x_i^{(2)} \end{bmatrix} + h^{-\alpha}\left[GL_{jp}^{(\alpha)} \quad .. \quad GL_{2jp-1}^{(\alpha)}\right]\left[H\right]\begin{bmatrix} x_{i-j} \\ x_{i-j}^{(1)} \\ x_{i-j}^{(2)} \\ x_{i-j}^{(3)} \end{bmatrix} +$$

$$.. + h^{-\alpha}\left[GL_{(k-1)jp}^{(\alpha)} \quad .. \quad GL_{kjp-1}^{(\alpha)}\right]\left[H\right]\begin{bmatrix} x_{i-(k-1)j} \\ x_{i-(k-1)j}^{(1)} \\ x_{i-(k-1)j}^{(2)} \\ x_{i-(k-1)j}^{(3)} \end{bmatrix}. \quad (2.46)$$

Note that the GL coefficients are fixed after the order of the fractional derivative alpha is fixed and the connectivity matrices H_0 and H are fixed after the time axis is divided by choosing h, Δt, j and k. The vector matrix multiplication will produce a vector 1x3 and a vector 1x4 therefore Equation (2.46) yields

$$x_i^{(a)} = \begin{bmatrix} G_{01}^{(\alpha)} & G_{02}^{(\alpha)} & G_{03}^{(\alpha)} \end{bmatrix}\begin{bmatrix} x_i \\ x_i^{(1)} \\ x_i^{(2)} \end{bmatrix} + \begin{bmatrix} G_{11}^{(\alpha)} & G_{12}^{(\alpha)} & G_{13}^{(\alpha)} & G_{14}^{(\alpha)} \end{bmatrix}\begin{bmatrix} x_{i-j} \\ x_{i-j}^{(1)} \\ x_{i-j}^{(2)} \\ x_{i-j}^{(3)} \end{bmatrix} + \ldots$$

$$\ldots+\begin{bmatrix} G_{(k-1)1}^{(\alpha)} & G_{(k-1)2}^{(\alpha)} & G_{(k-1)3}^{(\alpha)} & G_{(k-1)4}^{(\alpha)} \end{bmatrix}\begin{bmatrix} x_{i-(k-1)j} \\ x_{i-(k-1)j}^{(1)} \\ x_{i-(k-1)j}^{(2)} \\ x_{i-(k-1)j}^{(3)} \end{bmatrix}, \quad (2.47)$$

where

$$G_{0l}^{(\alpha)} = \sum_{q=0}^{jp-1} GL_q^{(\alpha)} H_0^{q,l} \quad (2.48)$$

and

$$G_{l_1 l_2}^{(\alpha)} = \sum_{q=jpl_1}^{jp(l_1+1)-1} GL_q^{(\alpha)} H^{q,l_2} . \quad (2.49)$$

Note, $H_0^{q,l}$ denotes the entry of the H_0 matrix at the q^{th} row and l^{th} column. Equivalently, H^{q,l_2} denotes the entry of the H matrix at the q^{th} row and $l_2{}^{th}$ column. Next, forming the difference of the fractional derivatives from two consecutive time steps yields

$$\Delta x_i^{(a)} = \begin{bmatrix} G_{01}^{(\alpha)} & G_{02}^{(\alpha)} & G_{03}^{(\alpha)} \end{bmatrix}\begin{bmatrix} \Delta x_i \\ \Delta x_i^{(1)} \\ \Delta x_i^{(2)} \end{bmatrix} + \begin{bmatrix} G_{11}^{(\alpha)} & G_{12}^{(\alpha)} & G_{13}^{(\alpha)} & G_{14}^{(\alpha)} \end{bmatrix}\begin{bmatrix} \Delta x_{i-j} \\ \Delta x_{i-j}^{(1)} \\ \Delta x_{i-j}^{(2)} \\ \Delta x_{i-j}^{(3)} \end{bmatrix} + ..$$

$$\ldots+\begin{bmatrix} G_{(k-1)1}^{(\alpha)} & G_{(k-1)2}^{(\alpha)} & G_{(k-1)3}^{(\alpha)} & G_{(k-1)4}^{(\alpha)} \end{bmatrix}\begin{bmatrix} \Delta x_{i-(k-1)j} \\ \Delta x_{i-(k-1)j}^{(1)} \\ \Delta x_{i-(k-1)j}^{(2)} \\ \Delta x_{i-(k-1)j}^{(3)} \end{bmatrix}. \quad (2.50)$$

Further, combining Equation (2.41) with Equation (2.50) yields

$$(m + K_i^g G_{03}^{(\alpha)})\Delta \ddot{x}_i + K_i^g G_{02}^{(\alpha)} \Delta \dot{x}_i + (K_i^g G_{01}^{(\alpha)} + K_i^q)\Delta x_i = \Delta f_i - \Delta f_{cor}, \quad (2.51)$$

where

$$\Delta f_{cor} = K_i^g \begin{bmatrix} G_{11}^{(\alpha)} & G_{12}^{(\alpha)} & G_{13}^{(\alpha)} & G_{14}^{(\alpha)} \end{bmatrix} \begin{bmatrix} \Delta x_{i-j} \\ \Delta x_{i-j}^{(1)} \\ \Delta x_{i-j}^{(2)} \\ \Delta x_{i-j}^{(3)} \end{bmatrix} + \ldots$$

$$\ldots + K_i^g \begin{bmatrix} G_{(k-1)1}^{(\alpha)} & G_{(k-1)2}^{(\alpha)} & G_{(k-1)3}^{(\alpha)} & G_{(k-1)4}^{(\alpha)} \end{bmatrix} \begin{bmatrix} \Delta x_{i-(k-1)j} \\ \Delta x_{i-(k-1)j}^{(1)} \\ \Delta x_{i-(k-1)j}^{(2)} \\ \Delta x_{i-(k-1)j}^{(3)} \end{bmatrix}. \quad (2.52)$$

The equation of motion is integrated in time using the Newmark time integration scheme where, mass, damping and stiffness are substituted by the effective values shown in Equation (2.51). The solution of this equivalent second order differential equation can be considered as a prediction, and a correction in the same time step of the excitation is due to the additional past terms. The above algorithm requires a small number of correction terms for every integration step in time, and the complete information at these steps such as displacement, velocity and acceleration. Further, the steps needed are separated by a number of j steps. There is a convenient way to circumvent the saving of the velocity and acceleration at each time step. This is done by approximating these quantities using the displacements at neighboring points. However, since the velocity and the acceleration are readily given by the Newmark algorithm it is deemed appropriate to describe the method avoiding the jerk and the approximation through the displacements of the steps. Thus, the correction is considered to be given by the equation

$$\Delta f_{cor} = K_i^g \begin{bmatrix} G_{11}^{(\alpha)} & G_{12}^{(\alpha)} & G_{13}^{(\alpha)} \end{bmatrix} \begin{bmatrix} \Delta x_{i-j} \\ \Delta x_{i-j}^{(1)} \\ \Delta x_{i-j}^{(2)} \end{bmatrix} + \ldots$$

$$\ldots + K_i^g \begin{bmatrix} G_{(k-1)1}^{(\alpha)} & G_{(k-1)2}^{(\alpha)} & G_{(k-1)3}^{(\alpha)} \end{bmatrix} \begin{bmatrix} \Delta x_{i-(k-1)j} \\ \Delta x_{i-(k-1)j}^{(1)} \\ \Delta x_{i-(k-1)j}^{(2)} \end{bmatrix}. \quad (2.53)$$

Next, note that the saving of the velocity and acceleration every j steps is needed along with the displacements to advance the algorithm. This can be proven quite powerful for the implementation of the algorithm in multi-degree-of-freedom systems. As Figure (2.1) shows, the jp steps of the fractional derivative estimation are approximated by the Taylor backwards expansion with respect to the displacement, velocity and acceleration of the i^{th} step. The multiplication of the first jp GL coefficients with the connectivity matrix H produces an equivalent mass, damping and stiffness coefficient matrix which can be added to the original equation of motion turning the fractional non linear differential equation into a non linear equation without fractional terms. The solution of this equation can be called the predictor step. Clearly, this equation takes into account only a limited number of past terms, specifically jp terms of time duration $jph=j\Delta t$. The correction step comes from the adjustment of the excitation by a term representing the rest of the past terms associated with the displacement, velocity and acceleration of previous time steps. Once again this is accomplished by a set of equivalent mass, damping and stiffness coefficients that are calculated once in the beginning as a product of the H connectivity matrix and the GL coefficients vector.

2.4.2. Linear fractional multi-term differential equations

Consider the case of a system with one or more purely elastic springs and n viscoelastic dissipative elements connected in parallel as shown in Figure (2.2) and governed by the equation of motion

$$m\ddot{x}+\sum_{l=1}^{n}\left(c_l x^{(\alpha_l)}\right)+Kx=f(t). \tag{2.54}$$

Utilizing Equation (2.50) yields

$$\left(m+\sum_{l=1}^{n}c_l G_{03}^{(\alpha_l)}\right)\Delta\ddot{x}_i+\sum_{l=1}^{n}c_k G_{02}^{(\alpha_l)}\Delta\dot{x}_i+\left(K+\sum_{l=1}^{n}c_l G_{01}^{(\alpha_l)}\right)\Delta x_i=\Delta f_i-\Delta f_{cor} \tag{2.55}$$

and the correction term

$$\Delta f_{cor}=\sum_{l=1}^{n}c_l\begin{bmatrix}G_{11}^{(\alpha_l)} & G_{12}^{(\alpha_l)} & G_{13}^{(\alpha_l)}\end{bmatrix}\begin{bmatrix}\Delta x_{i-j}\\ \Delta x_{i-j}^{(1)}\\ \Delta x_{i-j}^{(2)}\end{bmatrix}+\ldots$$

$$\ldots+\sum_{l=1}^{n}c_l\begin{bmatrix}G_{(l-1)1}^{(\alpha_l)} & G_{(l-1)2}^{(\alpha_l)} & G_{(l-1)3}^{(\alpha_l)}\end{bmatrix}\begin{bmatrix}\Delta x_{i-(k-1)j}\\ \Delta x_{i-(k-1)j}^{(1)}\\ \Delta x_{i-(k-1)j}^{(2)}\end{bmatrix}. \tag{2.56}$$

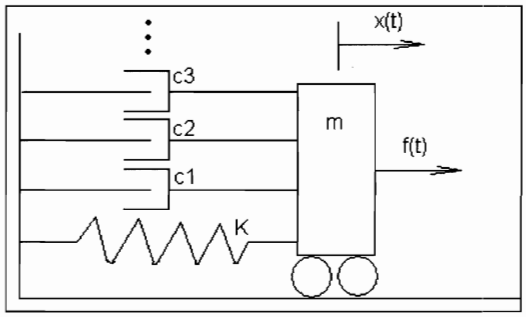

Figure 2.2 Viscoelastic elements and an elastic spring in parallel connection.

2.4.3 Initial conditions

Imposing initial conditions on fractional differential equations presents non trivial challenges. The fractional differentiation and integration are by nature non local operations. Therefore, since the typical initial conditions required for solving ordinary and partial differential equations are the displacement and velocity which are locally obtained values, a significant problem is introduced. Specifically, the often used Riemann-Liouville derivative defined by

$$ {}_{RL}D^{\alpha}_{t_0,t}x(t) = \frac{d^n}{dt^n}\left\{\frac{1}{\Gamma(n-\alpha)}\int_{t_0}^{t}(t-\tau)^{n-\alpha-1}\,x(\tau)\,d\tau\right\}, \qquad (2.57) $$

where the integer n satisfies $n-1 \le \alpha < n$, t_0 denotes the lower limit and α the order of fractional differentiation introduces a numerically difficulty for non zero initial conditions (see Fukunaga and Shimizu 2004). Since no past terms exist before the initiation of the oscillatory motion the lower limit t_0 is assumed to be zero and the divergent difficulty is introduced by this abrupt truncation of the displacement function x(t). It was shown in (Ochmann and Malakov 1993; Zhang and Shimizu 1999) that a smooth extension of the displacement function for $t<0$ resolves this difficulty. Extensive investigation on solving fractional differential equation with non zero initial conditions can be found in (Fukunaga and Shimizu 2004). Also, Caputo (1974) modified the definition of the fractional derivative to introduce initial conditions composed of the values of the displacement function and its successive integer order derivatives. However, due to this modification the solution of fractional differential equations with non zero initial conditions using the Caputo definition can be different than that of using other fractional derivative

expressions (see Trigeassou and Maamri 2011). For this reason, initial conditions used herein are zero and thus the results are identical independently from the fractional derivative expression such as Riemann-Liouville, Grunwald-Letnikov and Caputo.

2.4.4 Numerical examples

As an example, consider a simple linear system of unit mass under a sinusoidal excitation with the equation of motion

$$\ddot{x} + x^{(0.25)} + 2x^{(0.5)} + x^{(0.75)} + 4x = \sin t\,. \tag{2.58}$$

Dividing the time domain in Δt of length 0.02 sec, h of 0.001 sec, setting j=5 and using only k=5 number of correction terms one obtains the solution shown in Figure (2.3) Specifically for this case, Equation (2.55) yields

$$m\Delta\ddot{x}_i + c\Delta\dot{x}_i + K\Delta x_i = \Delta(\sin t) - \Delta f_{cor}\,, \tag{2.59}$$

where

$$\begin{aligned} m &= 0.9882 \\ c &= 0.8663 \\ K &= 10.5964 \end{aligned} \tag{2.60}$$

and Δf_{cor} yields

$$\Delta f_{cor} = 10^{-3}\begin{bmatrix} -1922 & 78 & -2.4 \end{bmatrix}\begin{bmatrix} \Delta x_{i-j} \\ \Delta x_{i-j}^{(1)} \\ \Delta x_{i-j}^{(2)} \end{bmatrix} + \ldots$$

$$\ldots + 10^{-3}\begin{bmatrix}-3.5 & 1.6 & -0.1\end{bmatrix}\begin{bmatrix}\Delta x_{i-20j} \\ \Delta x^{(1)}_{i-20j} \\ \Delta x^{(2)}_{i-20j}\end{bmatrix}. \quad (2.61)$$

Equation (2.58) is solved using the benchmark algorithm G1 (Podlubny 1999; Oldham and Spanier; Miller and Ross 1993) for the first p steps and then equation (2.59) is solved using Equation (2.61) for the rest N-p time steps. The average acceleration Newmark algorithm is used having parameters β=0.25 and γ=0.5. The error between the numerical integration solution and the frequency domain solution is also shown in Figures (2.3) and (2.4). The error function used herein is defined as the difference between the numerical integration scheme and the frequency domain solution as

$$error(t) = x(t) - x_f(t), \quad (2.62)$$

where $x_f(t)$ denotes the frequency domain solution obtained using Fourier transform; see (2.4.6). The convergence of this numerical scheme depends on both the coarse time step Δt and in the time step h. Convergence of the algorithm is shown in Figures (2.5), (2.6), (2.7) and (2.8) where the error between the two solutions decreases monotonically as the number of past terms involved in the fractional derivative estimation is increasing. Specifically, in Figure (2.5) the error for increasing number of past terms j is shown for k=5 of correction terms. In Figure (2.6) the error is shown for the same values of j and for k=10 correction terms. Further, Figures (2.7) and (2.8) show the error for k=15 and k=20 correction terms. Note that each figure shows the error decreasing as the number of past terms j increases and from each figure to the other, the error is also

decreasing as the number of correction terms k is increasing. This may be construed as a numerical convergence proof, since as either one of the parameters j or k is increasing, the error monotonically decreases. Table (2.1) shows the $\max\{|error|\}$ for several combinations of correction k and past j terms.

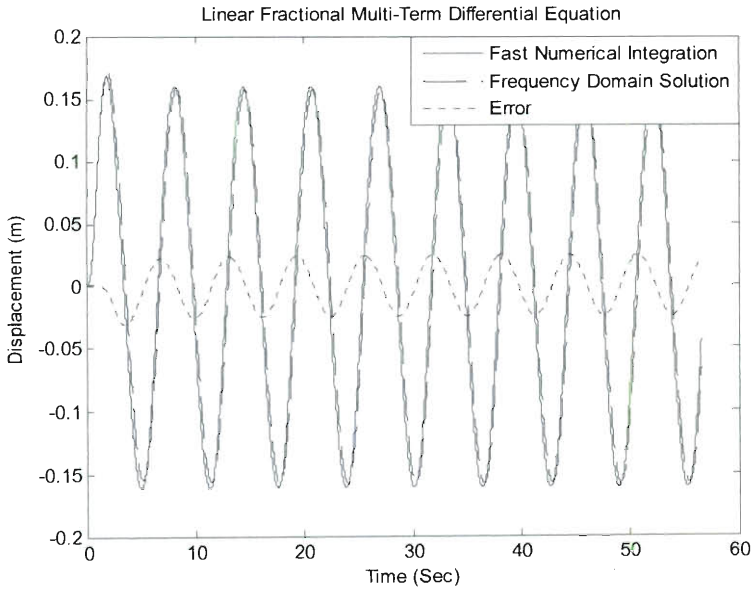

Figure 2.3 Frequency domain solution vis a vis numerical integration, Δt=0.02 sec, h=0.001 sec, p=20, j=5, k=5.

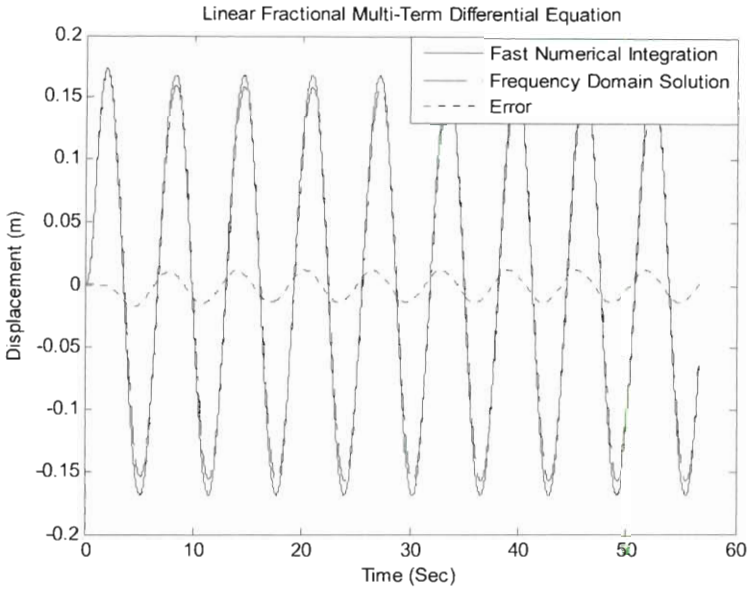

Figure 2.4 Frequency domain solution vis a vis numerical integration, Δt=0.02 sec, h=0.001 sec, p=20, j=10, k=5.

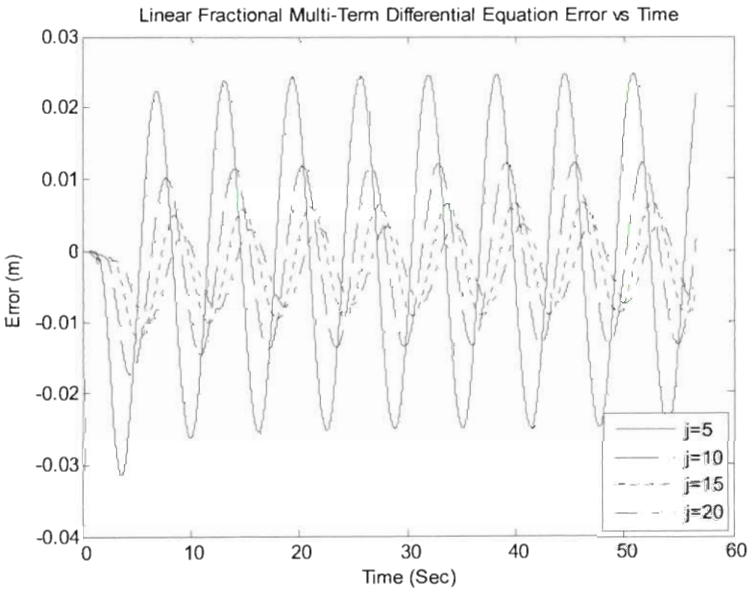

Figure 2.5 Error vis-a-vis time for Δt=0.02 Sec, h=0.001 Sec, p=20, k=5 and j=5, 10, 15, 20.

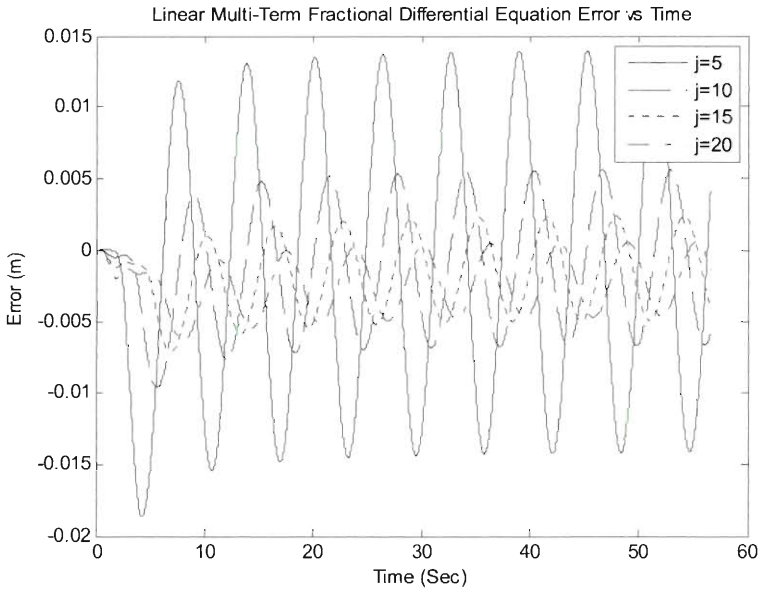

Figure 2.6 Error vis-à-vis time for Δt=0.02 Sec, h=0.001 Sec, p=20, k=10 and j=5, 10, 15, 20.

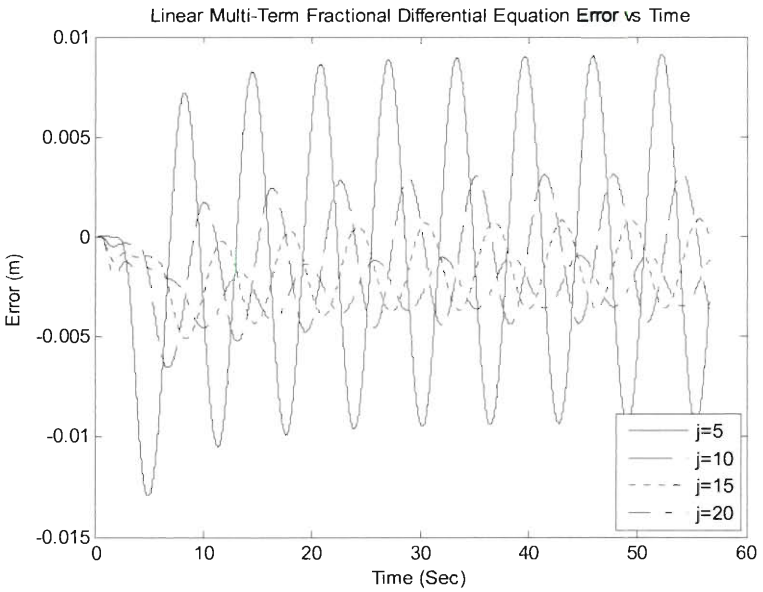

Figure 2.7 Error vis-à-vis time for Δt=0.02 Sec, h=0.001 Sec, p=20, k=15 and j=5, 10, 15, 20.

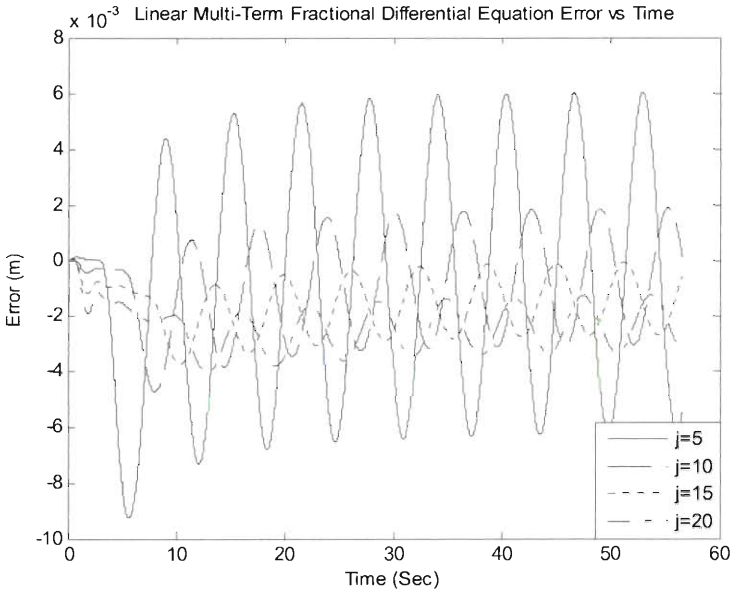

Figure. 2.8 Error vis-à-vis time for Δt=0.02 Sec, h=0.001 Sec, p=20, k=20 and j=5, 10, 15, 20.

k \ j	5	10	15	20	25	30
5	0.0314	0.0175	0.0123	0.01	0.0089	0.008
10	0.0187	0.0097	0.0071	0.0063	0.0058	0.0047
15	0.0129	0.0066	0.0051	0.0046	0.00459	0.00459
20	0.0093	0.0047	0.0038	0.003756	0.003787	0.0036

Table. 2.1 Maximum absolute value of the error function for Δt=0.02 Sec, h=0.001 Sec, p=20, k=5, 10, 15, 20 and j=5, 10, 15, 20, 25, 30.

In addition to the example of Equation (2.58), 3 other examples are considered to elucidate the performance of this scheme. Table (2.2) shows the values of the parameters in Equation (2.54) for each example and Tables (2.3), (2.4) and (2.5) summarize the error results. It can be seen from the Tables that as the correction terms k increase the error decreases monotonically. However, as the number of past terms approximation by a Taylor expansion increase, the error decreases up to a certain level, and then it increases. This trend is attributed to the fact that the second order Taylor expansion can accurately capture the past terms that are

significantly near the expansion point. Therefore, depending on the smoothness of the response each problem has a different optimal j parameter. Proper selection of the j parameter presents the challenge of the scheme. Obviously, from the results it can be seen that for small numbers j the error is clearly decreasing, and thus a small number j should always be preferred.

	m	c_1	c_2	c_3	α_1	α_2	α_3	K	f(t)
Example A	1	1	2	1	0.25	0.5	0.75	4	sin(t)
Example B	1	2	4	2	0.25	0.5	0.75	1	sin(t)
Example C	1	1	2	1	1.25	1.5	1.75	4	sin(t)
Example D	1	1	1	1	0.25	0.5	0.75	0	sin(t)

Table. 2.2 Parameter values for 4 numerical examples of linear fractional multi-term differential equations shown in equation (2.54).

k \ j	5	10	15	20	25	30
5	0.0556	0.0346	0.0255	0.0209	0.0181	0.0157
10	0.0365	0.0205	0.0154	0.0135	0.0127	0.0108
15	0.0265	0.0144	0.0116	0.0112	0.0112	0.011
20	0.0196	0.0106	0.0097	0.00974	0.0096	0.0094

Table. 2.3 Maximum absolute value of the error function for Δt=0.02 Sec, h=0.001 Sec, p=20, k=5, 10, 15, 20 and j=5, 10, 15, 20, 25, 30 for example B.

k \ j	5	10	15	20	25	30
5	0.1578	0.0545	0.0284	0.0218	0.0222	0.0235
10	0.0624	0.0209	0.0155	0.0145	0.0139	0.0153
15	0.0339	0.0131	0.0101	0.0102	0.0134	0.0173
20	0.0198	0.0086	0.0073	0.0111	0.0139	0.0164

Table. 2.4 Maximum absolute value of the error function for Δt=0.02 Sec, h=0.001 Sec, p=20, k=5, 10, 15, 20 and j=5, 10, 15, 20, 25, 30 for example C.

k \ j	5	10	15	20	25	30
5	0.2318	0.1405	0.1003	0.0802	0.0705	0.067
10	0.1501	0.0815	0.0576	0.0519	0.0501	0.0491
15	0.1087	0.0563	0.0444	0.0404	0.0434	0.0514
20	0.0802	0.0434	0.035	0.0367	0.0425	0.0454

Table. 2.5 Maximum absolute value of the error function for Δt=0.02 Sec, h=0.001 Sec, p=20, k=5, 10, 15, 20 and j=5, 10, 15, 20, 25, 30 for example D.

2.4.5 Numerical results for earthquake excitation

Consider next the ElCentro 1940, California earthquake excitation shown in Figure (2.9), and a single degree of freedom oscillator with restoring forces governed by fractional derivatives. Proceed to implement the described algorithm and to obtain the system response.

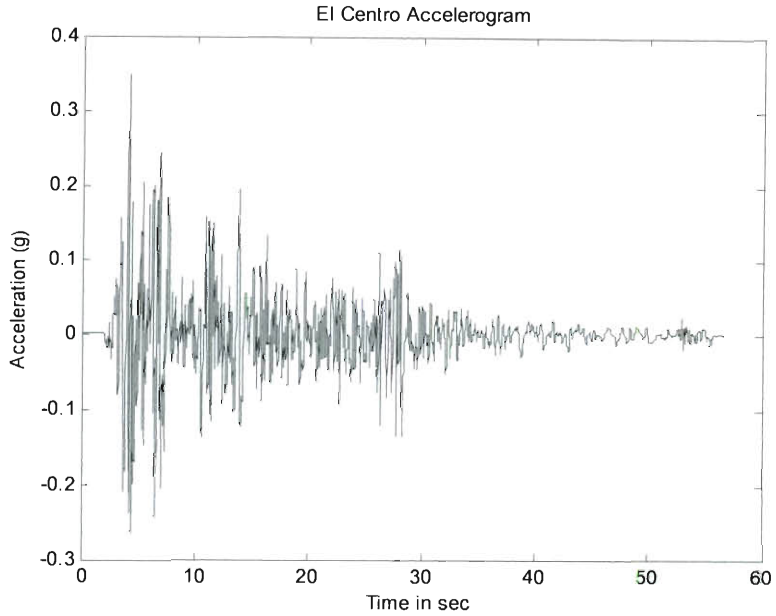

Figure 2.9 The El-Centro Accelerogram; g is the gravitational acceleration.

The coarse time discretization for the integration in time is of length Δt=0.02 seconds and the fine discretization is h=0.001 and h=0.004 seconds, thus p=20 and p=5. The range of the Taylor expansion is equal to $3\Delta t$, $4\Delta t$, $5\Delta t$ and $6\Delta t$ thus j=3,4,5 and 6. Since four correction terms have been used in every simulation k=5. The range of the Taylor expansion is obtained in a heuristic manner by assuming that the max Δt for Newmark is T/10 where T is the natural period of the system (Chopra 1995). Then, one can obtain the number j as $j=\Delta t\ max/\Delta t$. It

can be argued that the choice of the number j representing the range of an acceptable approximation by the Taylor expansion can be rigorously addressed. However, such an attempt would be a quite laborious process and is out of the scope of this work. Empirically, however, it is seen that the first $j\Delta t$ seconds including the jp past terms must have a significantly high threshold. That is, Equation (2.8) for n=jp must has a much larger value than n=kjp which is the threshold for the entire representation range. This is readily explained, by the fact that the correcting terms must account for larger correction than the correction achieved by the first Taylor expansion and the changing of the mass damping and stiffness values. Next consider results for linear systems, and non linear systems of the Duffing type. The same values of fractional derivatives are used for both the linear and non linear cases and quite large values of the non linearity strength ε are considered. Specifically, the system considered is governed by Equation (2.37) with a Duffing kind nonlinearity. This is,

$$m\ddot{x} + cD_{0,t}^{\alpha}x + Kx(1+\varepsilon x^2) = f(t). \tag{2.63}$$

The results of solving Equation (2.55, 2.56) via the proposed algorithm are compared to the benchmark G1 algorithm (Podlubny 1999; Oldham and Spanier; Miller and Ross 1993; Spanos and Evangelatos 2010) results which use the truncated Grunwald-Letnikov representation. Pertinent results for various values of fractional derivatives are shown in Figures (2.11), (2.13), and (2.15). Further, for linear systems this approach is verified by comparison with the frequency domain solution and the results are shown in Figures (2.10), (2.12) and (2.14). That is the Fourier transform of the excitation signal is computed. It is then

multiplied by the transfer function of the oscillator. Finally, this product is Fourier-inverted to determine the response of the linear oscillator. This procedure is further elucidated in the next section.

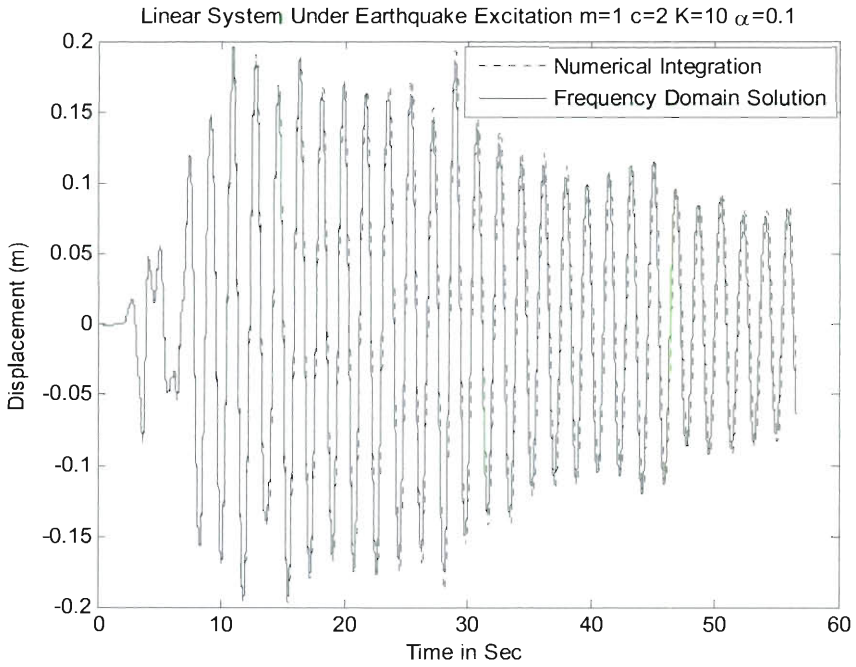

Figure 2.10 Frequency domain solution vis a vis numerical integration with correction step of four past terms p=20, j=5, k=5.

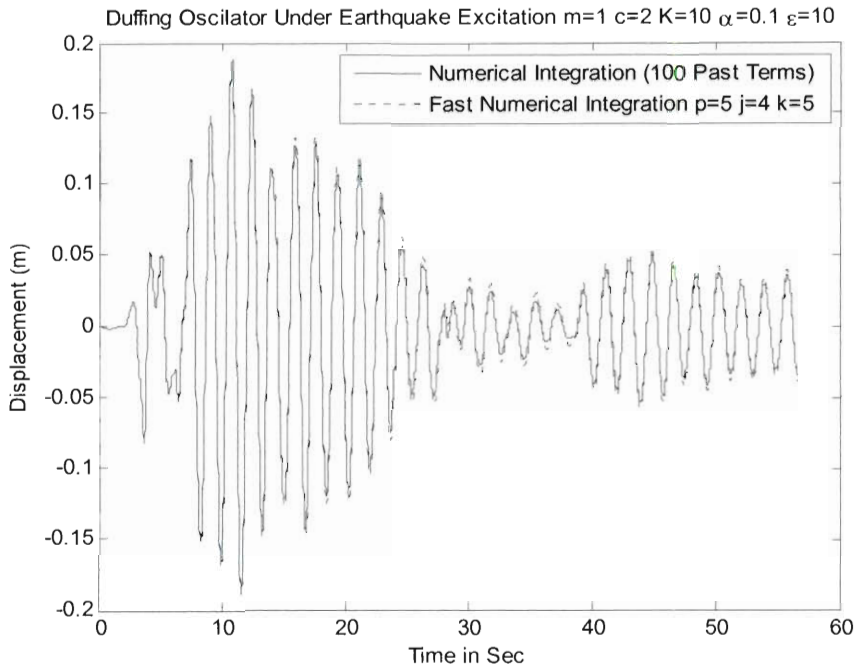

Figure 2.11 Numerical solution with past terms corresponding to GL coefficients of the order 10^{-3} vis a vis the enhanced numerical integration algorithm

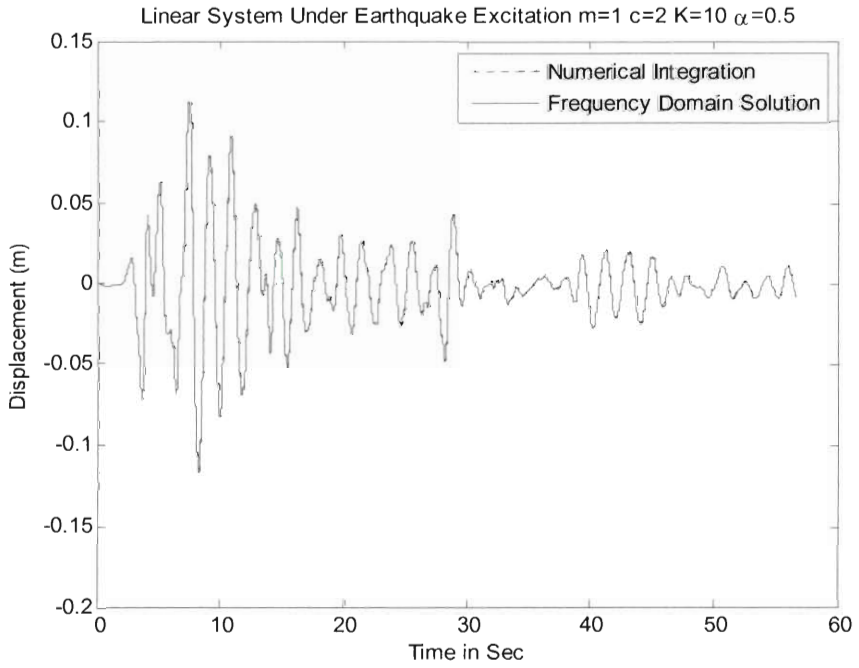

Figure 2.12 Frequency domain solution vis a vis numerical integration with correction step of four past terms p=20, j=9, k=5.

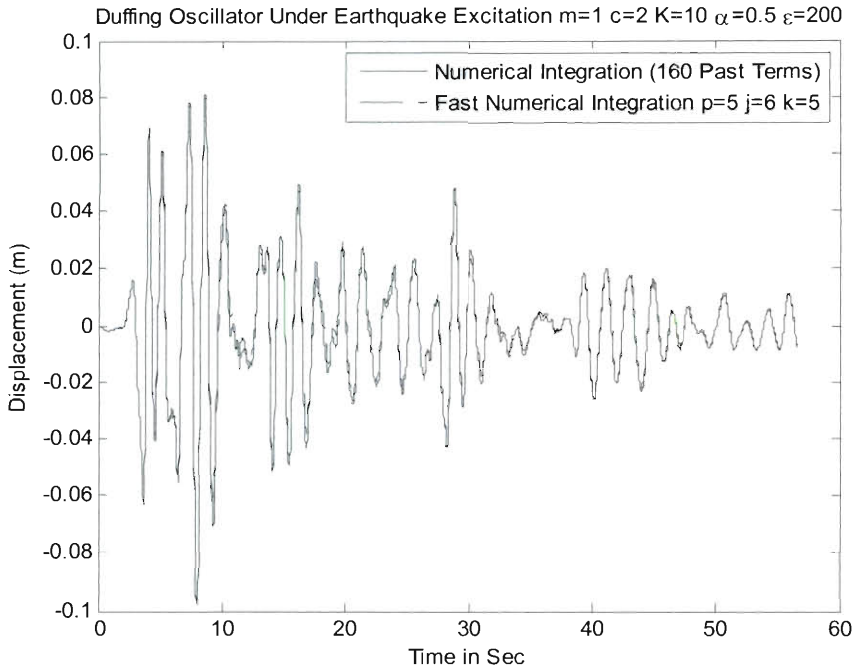

Figure 2.13 Numerical solution with past terms corresponding to GL coefficients of the order 10^{-3} vis a vis the enhanced numerical integration algorithm

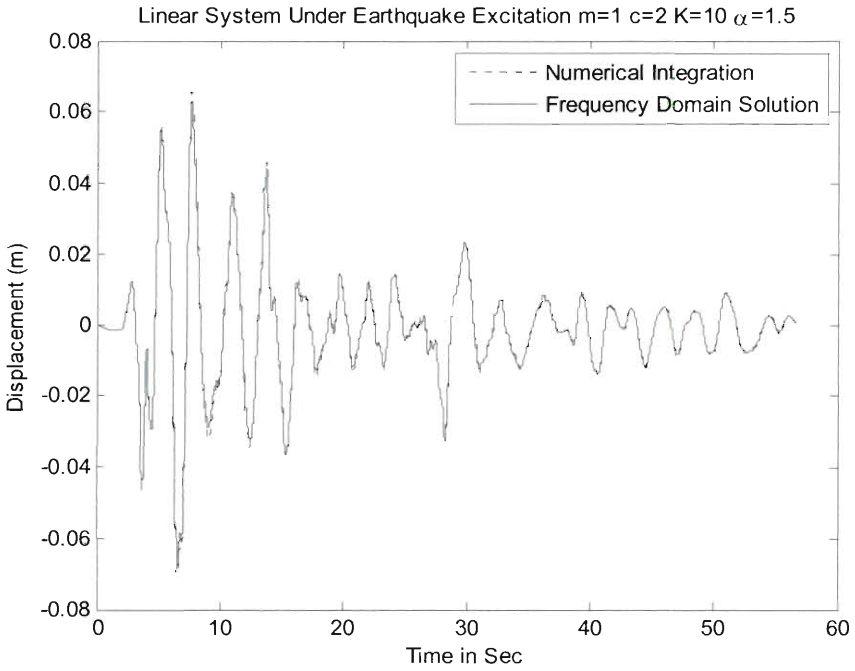

Figure 2.14 Exact solution vis a vis numerical integration with correction step of four past terms p=20, j=9, k=5.

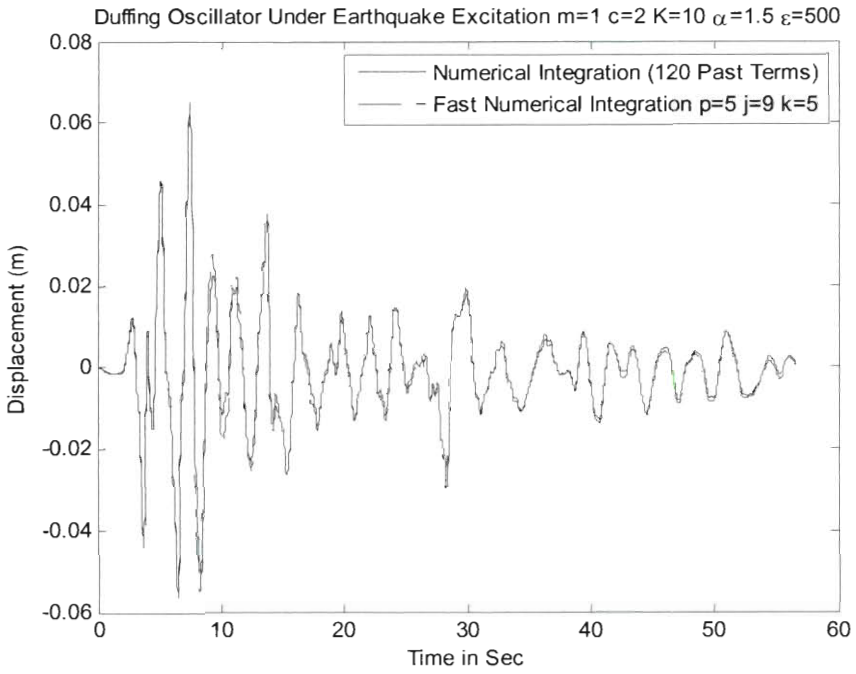

Figure 2.15 Numerical solution with past terms corresponding to GL coefficients of the order 10^{-3} vis a vis the enhanced numerical integration algorithm

2.4.6 Frequency domain solution

Solving linear fractional multi-term differential equations shown in Equation (2.54) with zero initial conditions is accurately pursued in the frequency domain. The Fourier transform on both parts of Equation (2.54) yields

$$\mathbb{F}\left\{ m\ddot{x} + \sum_{k=1}^{n}\left(c_k x^{(\alpha_k)}\right) + Kx \right\} = \mathbb{F}\{f\}. \tag{2.64}$$

Carrying out the calculations yields

$$\left(-m\omega^2 + \sum_{k=1}^{n}\left(c_k (i\omega)^{\alpha_k}\right) + K \right) X(\omega) = F(\omega), \tag{2.65}$$

where the X denotes the Fourier transform of the displacement

$$X(\omega) = \mathbb{F}\{x\}. \tag{2.66}$$

Solving Equation (2.64) and combing with Equation (2.65) yields the solution in the time domain denoted herein as x_f

$$x_f(t) = \mathbb{F}^{-1}\left\{\frac{F(\omega)}{\left(-m\omega^2 + \sum_{k=1}^{n}\left(c_k(i\omega)^{\alpha_k}\right) + K\right)}\right\}. \tag{2.67}$$

Chapter 3

Polyester Mooring Lines Analysis

3.1 Introduction

The perspective of the previous chapters will be used in this to model the behavior of polyester mooring lines. The exposition of the various concepts is expedited by resorting to the material of appendix A. Mooring systems have been used in offshore engineering applications for several years. The performance of any mooring system depends on the size and kind of the moored vessel, the applied environmental forces, the water depth, and the soil conditions of the sea bed. Under challenging sea conditions the proper choice of anchors, clump weights, chains and cables becomes critical for keeping the vessel on site and for the mooring system survival. In designing a mooring system, one must first specify the vessel which needs to be kept in place, and then to apply proper mathematical models and analysis techniques to assess its adequacy and station keeping capability (Herbich 1999). In this regard, the design needs to account for possible cable tensions along with possible failure modes, such as the breaking of cable in an extreme event or the dragging of the anchor. Of course, cost benefit analysis is a most critical part in the decision making.

Early applications of polyester lines were reported a couple of decades ago. Polyester mooring lines have attracted attention due to their superior strength and their light weight which is counterbalanced when the ropes are submerged. Thus, the use of polyester mooring systems results into smaller platforms and

ground chains, smaller chain jacks and fairleads, which also produce cost saving beyond the impact on the hull. There are specific ways for the line to be installed and operate. Every polyester mooring system must have an inspection, maintenance, repair and retirement plan (IMRR). Due to these requirements the line consists of many parts from the jack of the platform to the anchoring point in the sea bed. In most of the cases the line has a number of polyester rope segments, two chain segments one at each end point and connectors in between. The bottom end of the line ends up in a suction pile onto the sea bed and the upper end is jacked in the platform with proper wheels and jacks. The jacks can adjust the length of the in and out board chain length so the platform can be relocated and fixed exactly above the oil wells. Analysis of multi-component lines is a quite difficult procedure during the design. Due to this fact, a two moduli approach is commonly the first step for the design procedure (Petruska et all 2005). Specifically, a static modulus is used to calculate the displacements of the platform for certain wind and wave loading, and a dynamic stiffness for the design of the spar in hostile environmental conditions. In a series of papers by (Childres 1973; Childres 1974; Childres 1975) the mooring system was considered from a more practical standpoint and the advantages of a multi-component line over the single component lines were discussed. Niedzwecki and Casadella (1975) developed a numerical algorithm to solve the catenary equations for a line with cable and chain components. However, such lines are not used in ultra deep water mooring systems where the depths are greater than usual. Further, lines have connectors which act like clumped weights and in this

particular study they are not treated. Nath and Felix (1970) considered a single point mooring system with a uniform cable and determined the mooring line motion and the tensions resulting from wave forces; they also implemented a numerical model limited though to certain depths and wave conditions. Wilson and Gabaccio (1969) also considered a uniform cable and therefore their technique is limited to single steel catenaries from the bottom up to the fairlead. Tuah and Leonard (1990) discussed a finite element model for predicting the dynamic viscoelastic response of a cable. The model is a three parameter linear visco-elastic model proper for dynamic analysis of multi-component systems. A powerful method to determine the geometry of the line and the static equilibrium forces was presented by Peyrot and Goilois (1979); it is basically an algorithm which iteratively determines the final equilibrium point of the line. The initial guess is of great importance to the convergence of the solution. The 'quasi-static' cable analysis deals with the dynamics of the anchoring system in a static manner, whereby a static equilibrium state is assumed at each time step. This assumption is reasonable since the response of the moored vessel is normally outside the frequency range of the mooring system. However, in this kind of analysis the line dynamics is ignored and there are situations where the dynamics of the line is of great importance. Ansari and Khan (1973) showed that the dynamics of the line can be of greater significance than previously thought when modeling each line component as a discrete dynamic system. However, their line model had a submerged weight, whereas in the polyester line the only weights that are important are the clumped weights of the connectors. Thus the dynamics of the

line will be primarily influenced by these weights. The loads that determine the design phase related to wind, currents, and waves.

Due to the stochastic nature of the wind, its properties vary with time and location. In standard meteorological practice, wind velocity and direction is predicted as an average over a given interval in time, varying from one minute to an hour (Remery and Van Oortmersson 1973). Despite the fact that wind fluctuations are occurring about the mean value of the velocity and direction, these forces are considered small in comparison to hydrodynamic forces. Thus, a steady wind velocity and direction is considered by most researchers adequate for design purposes (Remery and Van Oortmersson 1973; Olsen et all 1973; Schellin et all 1982). It is clear that the constant winds in velocity and in direction will move the platform to a new equilibrium position and keep it there with small variations. Therefore, the static stiffness becomes an essential tool in the design process because it leads to the calculation of the average displacement of the platform about the new equilibrium point. Currents, however, can not be treated in this fashion. Their complexity of occurrence is attributed to several other phenomena. Currents are primarily due to ocean circulation and create steady currents, from cyclic changes in lunar and solar gravities causing tidal currents and from wind and water density differences. Because of their slow variation one can model them for analysis purposes as constant loads and carry on the design scheme using the static stiffness coefficient. Currents also create other kinds of loading for the submerged parts of the platform, besides the force from the

impact. Friction of the parts with the water is also an important load along with the pressure drag.

In the preceding context, data collected from the Gulf of Mexico during Hurricane Katrina on (8/25/2005-8/31/2005) are utilized herein in conjunction with the fractional calculus and generalized material models. This is done for the purpose of deriving a reliable constitutive equation governing the modulus of elasticity of polyester operating in service conditions. Specifically, the modulus is separated in two parts, the static modulus and the dynamic modulus. For the static modulus, an inverse identification problem is solved to obtain an accurate estimate. For the dynamic modulus, an unknown dependency on the strain and the strain's fractional derivatives is assumed. This dependency is modeled as polynomial terms of the strain and polynomial terms of the fractional derivatives of the strain. Specifically, a non linear viscoelastic model much like the Zener model is used with terms of arbitrary orders of fractional derivatives. Note that the Zener model can accurately capture most of real materials behavior due to its generalized form (see Podlubny 1999). Furthermore, the Zener model is superior to the Kelvin-Voigt and Maxwell model since it is a combination of both models and affords capturing both creep and relaxation (see Podlubny 1999). Specifically, an elaborate model such as the one proposed is perhaps able to model any kind of real material, since the fractional derivative terms account for linear hysteresis and fading memory effects (Nutting 1921; Scot-Blair 1949; Gemant 1936; Gemant 1938; Grunwald 1867; Makris 1991; Makris and Constantinou 1992), and the polynomials of such terms account to any type of rate dependent non linearity.

In this regard, the fitting of a non linear viscoeleastic model incorporating fractional derivative terms is then performed and the identification of the underlying parameters yields a non trivial least squares minimization problem.

Specifically, the displacements of the operating platform in the Gulf of Mexico, during the hurricane Katrina are used as input to a mathematical model to numerically estimate the effective stiffness of the polyester mooring lines used for its station keeping. The configuration of the platform is known. The stiffness of the line components is known except for the polyester segments. The non linear catenary equations are used iteratively to calculate the equilibrium geometry of the line. In this regard, by utilizing the known fairlead position, an inverse problem is solved to calculate the stiffness and the initial length of the polyester. For calm sea conditions the obtained stiffness is denoted as the static stiffness and is then verified for other periods of time on calm sea conditions. For confused sea conditions the dynamic stiffness is obtained as the additional stiffness needed for the polyester to satisfy the force equilibrium. Nevertheless, the identification of the dynamic stiffness poses non trivial challenges. Specifically, the separation of the loads in static and dynamic is more of a heuristic process, rather than, separation based on clearly defined bounds. For this reason, several time histories of the line tension and the underlying strain obtained near the platform's peak hurricane response are utilized in conjunction to non linear regression methods to fit the parameters of the proposed non linear viscoelastic model. Results of the proposed model are compared vis a vis the recorded data, and the effectiveness of this model in capturing the quite complex behavior of polyester is shown.

3.2 Modeling of the Problem

An offshore platform has GPS (Global Positioning System) and accelerometers to provide its position at any time point. From the data acquired and by using the reliability region of each instrument in the frequency domain, a quite accurate displacement calculation can be obtained (Appendix A). Then, the 6 degrees of freedom from the center line of the platform can be translated in each fairlead point using a Gaussian translation matrix (Appendix A). Therefore, a displacement versus time history is available at each fairlead point. Tension measurements are also available at each fairlead point and the components of the line and their properties are known for each line. However, the lengths of the polyester segments involve uncertainty. Usually, the lines are pre-stressed before installation to release as much construction creep is possible. Despite the pre-stressing of the line, construction creep remains since removing it entirely would demand a large pre-stressing force. Therefore, it is reasonable to assume a linear behavior of the polyester segments in loading situations caused by calm sea conditions. Specifically, for static loading of smaller level than the pretension level this assumption is quite satisfactory. However, the initial length after which this behavior can be assumed linear can only be estimated by assuming a static stiffness coefficient. Therefore, the initial zero stress length of each polyester segment along with its corresponding stiffness is treated as unknowns in this proposed model, and both their values are estimated using an iterative approach employing the catenary equations.

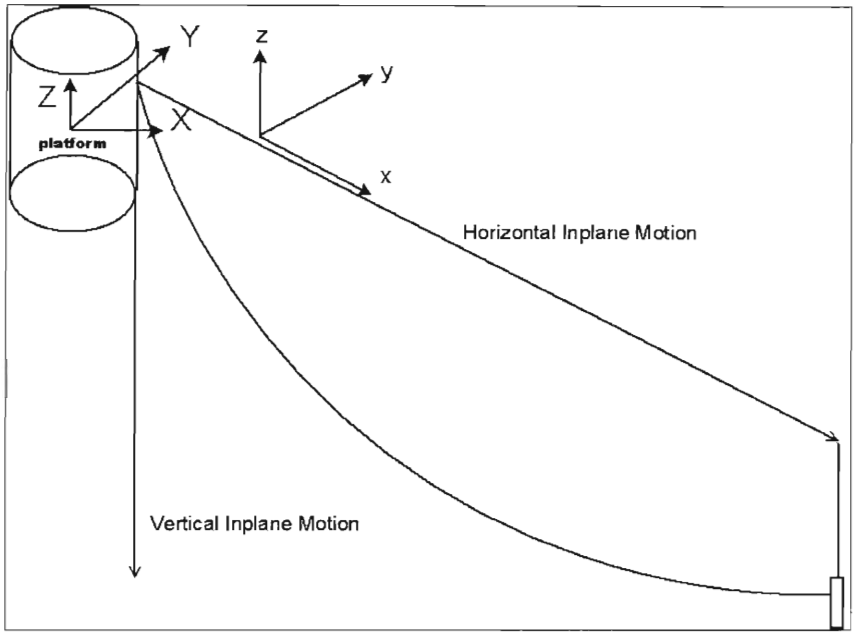

Figure 3.1. The line from the fairlead point of the platform to the anchoring point and the global and local coordinate systems.

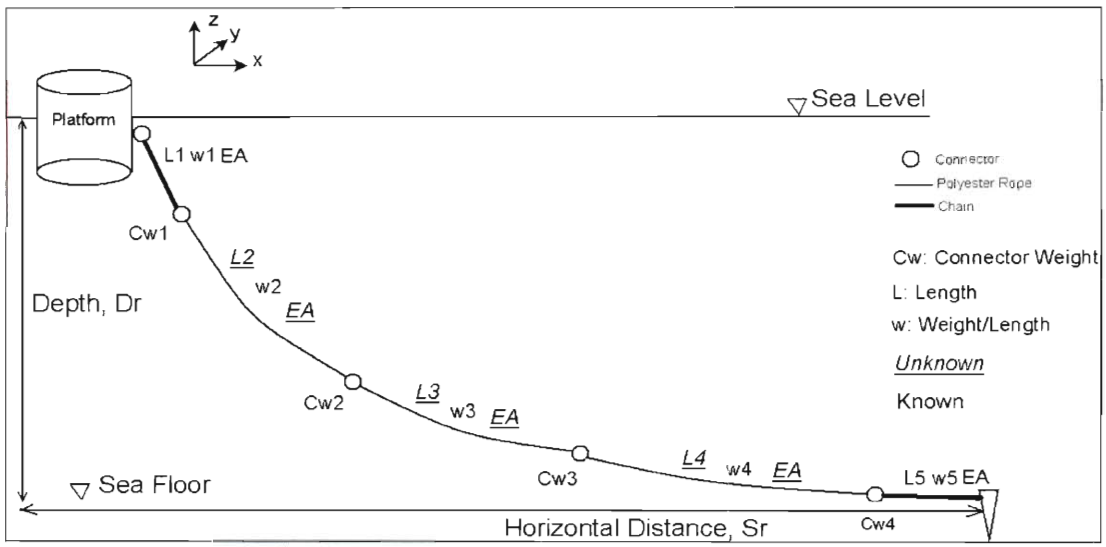

Figure 3.2. A typical polyester mooring line at in-plane depiction. Known and unknown parameters of the line are also shown.

As it can be seen in Figures (3.1) and (3.2), each line comprises many components, most of them connectors, chains, and large polyester segments. In a global axis system the exact location of the fairlead and the anchoring point are

known (Appendix A); also the force at the fairlead is known. Having this information available along with the catenary equations, one can estimate the exact position and tension at the bottom end of each component. This is done by starting from a known position and tension of the initial point and knowing the properties of the component. Next iteratively proceeding from the first component (chain on the platform) to the last one (chain at the sea bed) the final point can be estimated and the shape of the submerged line can be determined. The shape of the line is estimated within certain error boundaries due to the fact that each part of the line must be calculated as a distinct catenary rope, and the connectors are quite heavy short length parts that introduce errors as one proceeds from one component to the next. As the platform swings, the shape of the line changes according to the position and the force at the fairlead. More specifically, the shape of the line changes when the in-plane and vertical distance change, in-plane distance is the horizontal distance between the anchoring point and the initial point of the line. Assuming that the zero stress length (L_0) is known by randomly choosing an initial angle θ, the coordinates of the final tip of the line can be calculated. Further, since the real anchoring points are known there is an error vector R that ultimately must be minimized with respect to some parameters which may be the angle θ and the EA modulus of polyester ropes. In the same manner, if the modulus of the polyester components is assumed known then, the angle and the L_0 can be the minimizing parameters. Equation (3.1) yields the error vector

$$R = \begin{bmatrix} D_e - D_r \\ S_e - S_r \end{bmatrix}, \tag{3.1}$$

where, De and Se are the estimated values of the depth and the horizontal distance, in the same way Dr and Sr represent the real depth and horizontal distance. Note, that the real values of these distances are known from the position of the platform and the position of the anchoring points.

Next, assuming that a certain algorithm minimizes the error R, convergence can be achieved for the minimizing parameters and therefore for each time point these parameters can be identified. However, L_0 and EA are both unknown parameters along with the angle, and since a constant EA and L_0 can be assumed for calm sea conditions, these two parameters must remain constant for every calm sea excitation. Using the fact that in calm sea conditions the tension is fairly constant and the platform swings slightly, the average position of the platform can be used for two different tension levels the minimum calm sea tension, and the maximum calm sea tension. Thus, an equivalent system of two unknowns with two equations can be set up where the unknowns are the EA and the L_0.

Obviously, this system is a non linear system of equations and its solution can be obtained by numerical iterations. Note, that dynamic analysis is not considered herein due to the small in plane accelerations and small line weights. Also, the polyester is buoyant when submerged, and thus the only significant weight is introduced by the chain and steel connectors. However, their weight and the acceleration magnitude is estimated to account for less than 4% of the static

forces applied on the line; and thus the quasi-static analysis is capturing quite accurately the response.

3.3 Non Linear Catenary Equations

Consider in Figure (3.3), a submerged infinitesimal rope section under tension and water current loads, as well as under its own submerged weight.

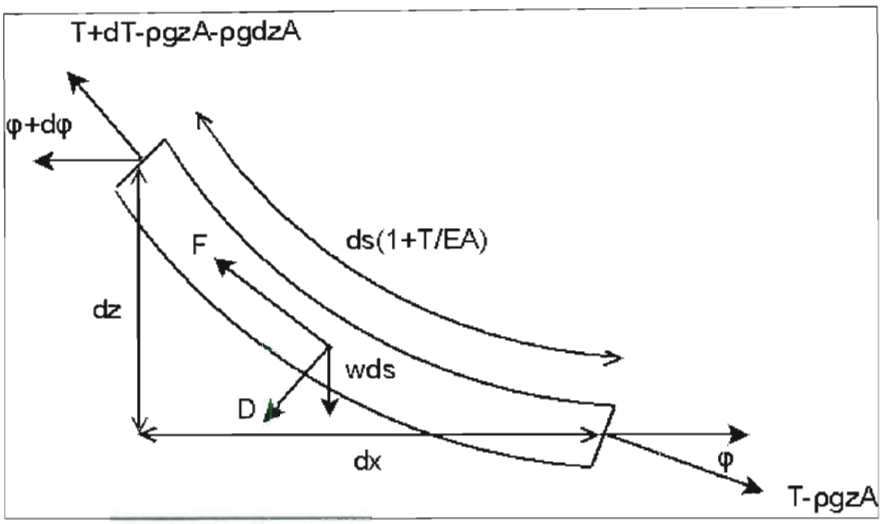

Figure 3.3. The infinitesimal submerged rope section starting from the sea floor.

Considering the equilibrium equation for the infinitesimal submerged rope segment in the X and Z directions, yields

$$dT - \rho gAdz = [w\sin\varphi - F(1 + T/EA)]ds \tag{3.2}$$

and

$$Td\varphi - \rho gAzd\varphi = [w\cos\varphi + D(1 + T/EA)]ds\,. \tag{3.3}$$

The symbols w, A, F and D denote the submerged weight, the cross section area, the shear force on the line and the vertical force on the line. Next, subtracting the water pressure force from the tension yields

$$T' = T - pgzA, \tag{3.4}$$

and combining Equation (3.2) and Equation (3.3) yields

$$\frac{dT'}{T'} = \frac{\sin\varphi}{\cos\varphi} d\varphi. \tag{3.5}$$

Integrating the differential Equation (3.5), yields

$$T' = T'_0 \frac{\cos\varphi_0}{\cos\varphi}. \tag{3.6}$$

Decomposing the differential length in the two dimensions x and z yields

$$dx = \cos\varphi dp, \tag{3.7}$$

and

$$dz = \sin\varphi dp. \tag{3.8}$$

Next, correcting the initial length by the stretched length yields

$$dp = ds(1 + T / EA). \tag{3.9}$$

Using the sin and cosine of the angle φ at the infinitesimal triangle of Figure (3.3), and assuming that the angle is negligibly affected from the water pressure subtraction, leads to

$$\frac{dx}{ds} = \cos\varphi(1 + T / EA) \approx \cos\varphi(1 + T'/ EA) = \cos\varphi + \frac{T_0'}{EA}, \tag{3.10}$$

and

$$\frac{dz}{ds} = \sin\varphi(1 + T/EA) \approx \sin\varphi(1 + T'/EA) = \sin\varphi + \frac{w}{EA}s. \tag{3.11}$$

Integrating Equation (3.10) yields

$$x - x_0 = \int(\cos\varphi + T_0'/EA)ds = \int\left(\cos\varphi + \frac{T'\cos\varphi}{EA\cos\varphi_0}\right)ds, \tag{3.12}$$

and combining Equations (3.3), (3.6) and (3.12) yields,

$$x - x_0 = \int\frac{T_0'\cos\varphi_0}{w\cos\varphi}\frac{d\varphi}{ds}(1 + \frac{T'}{EA\cos\varphi_0})ds. \tag{3.13}$$

Further, introducing the variable φ and changing variables from ds to $d\varphi$ yields

$$x - x_0 = \int\frac{T_0'\cos\varphi_0}{w\cos\varphi}(1 + \frac{T'}{EA\cos\varphi_0})d\varphi. \tag{3.14}$$

Further, carrying out the integration in Equation (3.14) yields

$$x = \frac{T_0'\cos\varphi_0}{w}\log\left(\frac{\frac{1}{\cos\varphi} + \tan\varphi}{\frac{1}{\cos\varphi_0} + \tan\varphi_0}\right) + \frac{T_0'^2\cos\varphi_0}{EAw}(\tan\varphi - \tan\varphi_0) + x_0. \tag{3.15}$$

One can follow the preceding procedure for the Z direction and derive for the two dimensions x and z representing the in-plane horizontal displacement and the vertical displacement as shown in Figure (3.2). The equation in the Z direction becomes

$$z = \frac{T_0'\cos\varphi_0}{w}\left(\frac{1}{\cos\varphi} - \frac{1}{\cos\varphi_0}\right) + \frac{T_0'^2\cos^2\varphi_0}{wEA}\left(\frac{1}{2\cos^2\varphi} - \frac{1}{2\cos^2\varphi_0} - \tan\varphi_0(\tan\varphi - \tan\varphi_0)\right) + z_0$$

(3.16)

The above stretched catenary equations define the coordinates of the final point of a submerged rope for known initial and final angle of the segment. The initial and final angle can be correlated by combining Equations (3.3) and (3.6) and integrating both sides yields

$$s - s_0 = \frac{T'_0 \cos\varphi_0}{w} \int_{\varphi_0}^{\varphi} \frac{1}{\cos^2 \varphi} d\varphi \ , \tag{3.17}$$

where the left side is the un-stretched length of the segment and can be substituted by L_0. Thus,

$$\tan\varphi = \frac{L_0 w}{T'_0 \cos\varphi_0} + \tan\varphi_0 \, . \tag{3.18}$$

3.4 Gauss-Newton Minimization Algorithm

Knowing the coordinates of the fairlead, the force at the line, the segments of the line and their properties one can start with an initial guess for the angle between the chain and the platform and simulate the line geometry. Knowing the coordinates of the bottom end of the line, the error vector R of the horizontal distance and the vertical distance that the end of the line went off can be calculated. This vector next can be minimized using the Gauss Newton non linear minimization algorithm. Figure (3.4) helps to elucidate the numerical scheme.

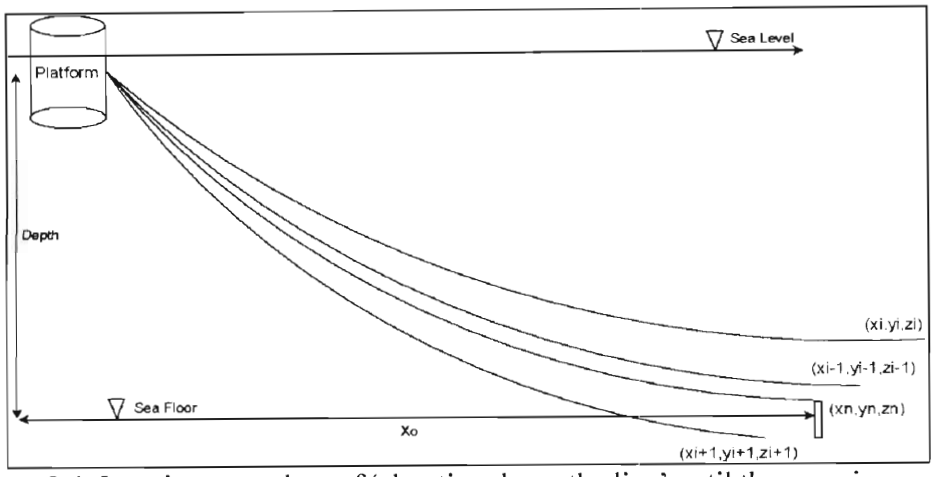

Figure 3.4. Iterative procedure of 'shooting down the line' until the error in Equation (3.1) is minimized.

Further, Equation (3.1) can be cast in the form of Equation (3.19) for numerical evaluation. The output of the algorithm is the initial angle, and the EA coefficient of each polyester segment or the angle and the L_0 of each polyester segment. Thus is,

$$R = \begin{bmatrix} \sum_i L_i(1 + T/EA)\sin(\vartheta_i) - D_r \\ \sum_i L_i(1 + T/EA)\cos(\vartheta_i) - S_r \end{bmatrix}. \tag{3.19}$$

Numerical methods for minimization problems are well developed and quite common in engineering applications. In this regard, significant challenge is associated with the initial guess, and the fact that the algorithm sometimes can only find a local minimum solution which may not be the global minimum (Nocedal and Wright). Further, the problem of 'entrapment' is quite common. It basically relates to the symptom of a local minimum being found but the algorithm is trapped inside it and stagnates for many iterations. In this case there are certain boundaries that need to be imposed. The stiffness modulus must be

within a certain range of values, and the construction creep can not be greater than a large value of 10%. Specifically $\theta \in (0, \pi/2)$, EA$\in$ (min(EA),max(EA)) and L_0 must satisfy the following relationship $1.1L_{or} > L_0 > L_{or}$ where L_{or} is the original zero stress length installed prior to the construction creep removal and L_0 is the assumed initial length with linear behavior after the construction creep has been removed.

Using the algorithm described with the above conditions a testing to calibrate the model is conducted with real and synthetic data inputs and the errors are compared with the professional program PROFLEX that uses finite elements for the line. The Gauss-Newton minimization algorithm is shown below. Knowing the initial value x_0

$$x_0 = \begin{bmatrix} \theta_0 \\ EA_0 \end{bmatrix}, \tag{3.20}$$

the next step is determined by the 'backtracking' algorithm (Nocedal and Wright) which ensures that the equation

$$f(x_k + a_k p_k) < f(x_k) \tag{3.21}$$

holds for step k. Where a_k and p_k are the length and the search direction towards the minimization point.

Two conditions must hold and they are called the Armijo conditions (Nocedal and Wright). That is,

$$f(x_k + a_k p_k) \leq f(x_k) + c_1 a \nabla f_k^T p_k \tag{3.22}$$

and

$$\nabla f(x_k + a_k p_k)^T p_k \geq c_2 \nabla f_k^T p_k, \tag{3.23}$$

where, Equation (3.22) ensures that the initial error becomes smaller in every step, and Equation (3.23) ensures that the step towards the local minimum is large enough so that the algorithm does not 'stagnate'. The symbol f denotes the quadratic object function that must be minimized; it corresponds to the norm of the error vector R. Coefficients c_1 and c_2 must be adjusted for stability and fast convergence of the algorithm and depend on the sensitivity of the problem. The coefficient α is usually set equal to 1, but there are ways to be adjusted for faster convergence (Cauchy initial point; see Nocedal and Wright). Next, f yields

$$f(x) = \frac{1}{2}\sum_{j=1}^{m} r_j^2(x). \tag{3.24}$$

Therefore, the gradient of this function yields

$$\nabla f(x) = \sum_{j=1}^{m} r_j(x)\nabla r_j(x) = J(x)^T R(x), \tag{3.25}$$

where the Jacobian is

$$J = \left[\partial R/\partial\theta \quad \partial R/\partial T\right], \tag{3.26}$$

and r_j in this case is each component of the R vector column-wise. The search direction vector p is the step towards the local minimum and is determined by using the equation

$$p_k = (J^T J)^{-1}(-J^T R). \tag{3.27}$$

Note that the $J^T J$ matrix in this specific case may be an ill-conditioned matrix, and for the examples below an infinitesimal diagonal matrix is added to shift the

eigenvalues away from the origin (see Nocedal and Wright). Knowing the 'step' p and the length, the next point x can be obtained from the equation

$$x_{k+1} = x_k + \alpha_k p_k . \tag{3.28}$$

Multiple solutions are usually obtained when minimization algorithms are used. However, in this case these solutions are easily discarded due to their non physical interpretation. Specifically, solutions that yield negative Young's modulus E, or angles $\theta<0$ essentially correspond to non possible line configurations.

3.5 Modeling Connector as Catenaries

Considering a line segment of length ds in Figure (3.5), force equilibrium demands that the change of the angle from φ to $\varphi + d\varphi$ provides an equal and opposite force to counterbalance the submerged weight. Note that if the dx curved segment is relatively heavy and short (connectors are quite heavy and short), this angle becomes smaller and therefore the dT force increases to a quite large value in order for the equilibrium to hold.

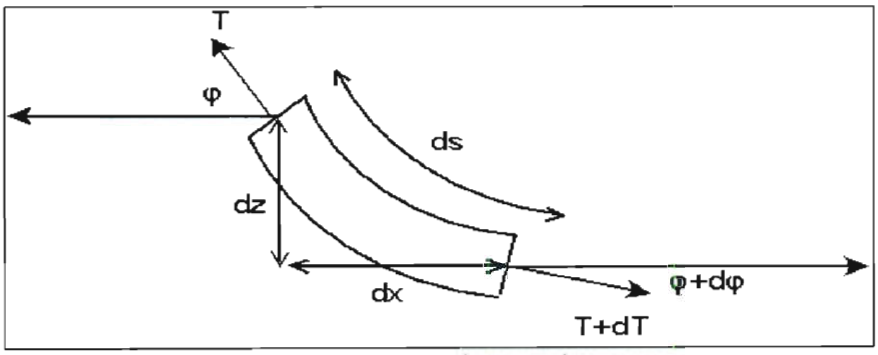

Figure 3.5. Infinitesimal submerged rope segment.

Therefore, a first attempt to lower the error relates redistributing the weight of the connectors to a larger fictitious connector. The tables below show the comparison of results from the custom made algorithm vis a vis commercial finite element package for in-service operational lines comprising three connectors, two polyester ropes and two chain segments. The accuracy of the custom algorithm in the tension and in the initial angle of the chain is of particular interest. Tables (3.1) through (3.3) show how the accuracy of the results improves by dealing with the 'effective' length of the connectors, where, the 'effective' length is the fictitious longer length for a lower distributed weight.

Input to Finite Elements Program PROFLEX								
Segment Properties Defined from Top to Sea Floor								
		Chain	Connector	Polyester	Connector	Polyester	Connector	Chain
Segment Length		260.6	0.2	1525.2	0.3	1478.9	0.2	230
Wet Weight (KN/m)		5.087	181.408	0.1042	209.28	0.1042	181.408	4.234
EA (KN)		1604732	1933687	378098.8	2024288	378098.8	1933687	1440385
# of Finite Elements		2	1	9	1	9	1	2
			X	Y	Z			
Fairlead Coordinates			45.55	-38.72	-18.18			
Anchor Coordinates			2446.99	-1424.64	-2191			
			PROFLEX		Custom Algorithm		Error %	
Fairlead Tension			5175		6021		16.35	
Line top Angle			51.44		50.07		2.65	

Table 3.1. Error results from commercial F.E. package and the custom program for small connecting segments.

Input to Finite Elements Program PROFLEX							
Segment Properties Defined from Top to Sea Floor							
	Chain	Connector	Polyester	Connector	Polyester	Connector	Chain
Segment Length	260.6	1	1525.2	1.5	1478.9	1	230
Wet Weight (KN/m)	5.087	36.28	0.1042	41.86	0.1042	36.28	4.234
EA (KN)	1604732	1933687	378098.8	2024288	378098.8	1933687	1440385
# of Finite Elements	2	1	9	1	9	1	2
		X	Y	Z			
Fairlead Coordinates		45.55	-38.72	-18.18			
Anchor Coordinates		2446.99	-1424.64	-2191			
		PROFLEX		Custom Algorithm		Error %	
Fairlead Tension		5175		5704		10.22	
Line top Angle		51.44		50.71		1.41	

Table 3.2. Error results from commercial F.E. package and the custom program for fictitious connecting segments of reasonable length.

Input to Finite Elements Program PROFLEX							
Segment Properties Defined from Top to Sea Floor							
	Chain	Connector	Polyester	Connector	Polyester	Connector	Chain
Segment Length	260.6	2	1525.2	3	1478.9	2	230
Wet Weight (KN/m)	5.087	18.14	0.1042	20.93	0.1042	18.14	4.234
EA (KN)	1604732	1933687	378098.8	2024288	378098.8	1933687	1440385
# of Finite Elements	2	1	9	1	9	1	2
		X	Y	Z			
Fairlead Coordinates		45.55	-38.72	-18.18			
Anchor Coordinates		2446.99	-1424.64	-2191			
		PROFLEX		Custom Algorithm		Error %	
Fairlead Tension		5175		5333		3.05	
Line top Angle		51.44		51.56		0.24	

Table 3.3. Error results for commercial F.E. package and the custom program for fictitious connecting segments of quite large length.

Tables (3.3) and (3.4) are for the same line with different tension at the initial tip of the line.

Input to Finite Elements Program PROFLEX							
Segment Properties Defined from Top to Sea Floor							
	Chain	Connector	Polyester	Connector	Polyester	Connector	Chain
Segment Length	260.6	2	1525.2	3	1478.9	2	230
Wet Weight (KN/m)	5.087	18.14	0.1042	20.93	0.1042	18.14	4.234
EA (KN)	1604732	1933687	378098.8	2024288	378098.8	1933687	1440385
# of Finite Elements	2	1	9	1	9	1	2
		X	Y	Z			
Fairlead Coordinates		45.55	-38.72	-18.18			
Anchor Coordinates		2446.99	-1424.64	-2191			
		PROFLEX		Custom Algorithm		Error %	
Fairlead Tension		3000		3030		1	
Line top Angle		62.22		62.54		0.51	

Table 3.4. Error results for commercial F.E package and the custom program for fictitious connecting segments of quite large length.

Taking this point into consideration, the algorithm is calibrated to use an 'effective' length for each short and heavy connector three times longer than its original length. This naturally perturbs the L_0 length, but to a minor degree, since the overall initial installed length is approximately 5800 ft for the specific line (Ultra Deep Water Conditions). The program is compared against the professional package PROFLEX for a steel catenary rise (one pipe all the way from the sea bed to the platform) for a simple line and for the two lines of the specific offshore structure. The number of iterations needed for convergence can be adjusted by the order of the error, usually 6-10 iterations are enough to reach accuracy up to 10^{-5}; Table (3.5) describes the output for the one pipe catenary all the way from the sea bed to the platform. As it can be seen in Table (3.5), the geometry of the steel pipe all the way down to the sea bed is accurately captured; it requirers 8 iterations and the accuracy is of order 10^{-3}. However, in Table (3.1), which relates to the real multi component line, the custom made algorithm yields a large

error in comparison to the commercial finite elements code PROFLEX, and the fictitious connector lengths have been used to reduce that error.

Input to Finite Elements Program PROFLEX				
Steel Catenary Rise (one segment from top to sea level)				
Segment Length (ft)		3413		
Wet Weight (lbs/ft)		74.5		
EA (Kips)		768708		
# of Finite Elements		150		
			X	Y	Z
Fairlead Coordinates			0	0	0
Anchor Coordinates			2044	0	-2480
		PROFLEX	Custom Algorithm		Error %
Fairlead Tension lbs		267418	267300		0.04
Line top Angle		72.1	72		0.01

Table 3.5. Error results for commercial F.E. package and custom algorithm for one segment line from the sea floor to the platform

3.5.1 Static moduli deduced from hurricane Katrina data

The preceding modeling was applied to data pertaining to the Katrina hurricane in the Gulf of Mexico on the 25^{th}-28^{th} of August 2005. Field data are in 20 min recordings for the movement of the platform and forces at the fairlead. For each file as input, derived is a 20 min recording output of the angle between the platform and the chain and the EA modulus or the length L_0. Data from hurricane Katrina were used to extract a static stiffness coefficient and dynamic stiffness time histories. The data set of hurricane Katrina involves, 6 days and consists of 72 files per day. After screening the data only the first 4 days were deemed reliable information due to the fact that after the hurricane intensified, the connection to the platform was lost. These 4 days begin from calm sea conditions (platform oscillates slowly) and progressively build up to the peak of the

hurricane. Figure (3.6) shows the maximum tension in Kips for the first group versus the number of the files starting the morning of August 25th 2005.

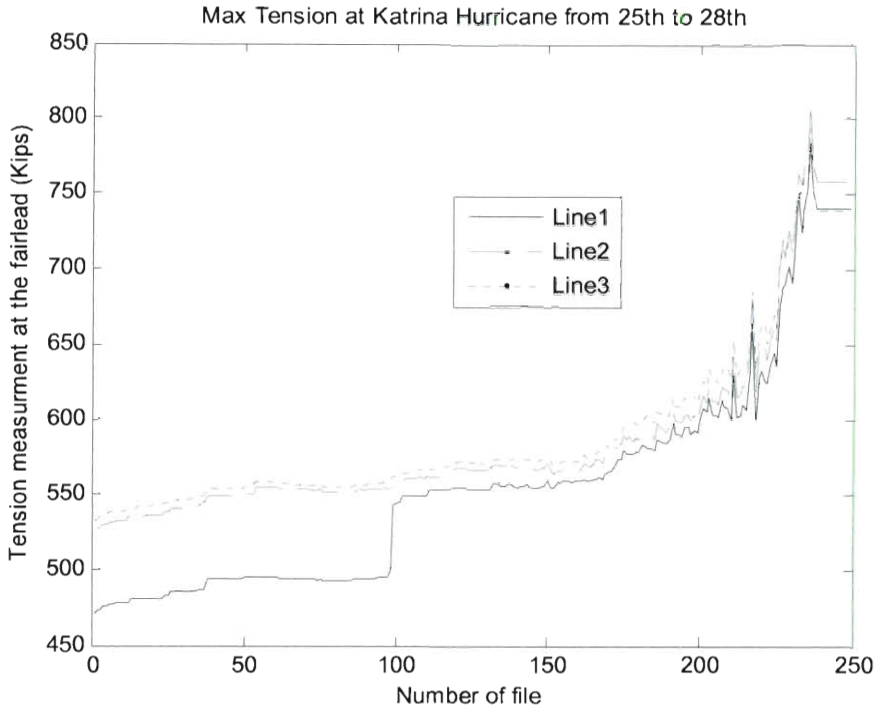

Figure 3.6. Maximum fairlead tension in Kips versus the number of 20min files from the 25th morning to 28th .

It is obvious that there is a line #1 readjustment before the peak of the hurricane, chain was pulled on board the platform so the tension of the line could match the rest of the group. For minimum tension occurring at midnight (00:00) of the 25th, the average displacement of the first line fairlead has been calculated. The same procedure is used for the maximum tension occurring prior to the readjustment of the line #1. For these two averaged displacements and tensions the EA coefficient was swiped from 9 BS to 17 BS (Due to the large value of the EA coefficient, industrial reports often use the normalized EA with respect to the Breaking

Strength of the polyester) and the corresponding L_0 is plotted. Figures (3.7), (3.8) and (3.9) show the surge, sway and heave fluctuations from which their means were used as inputs.

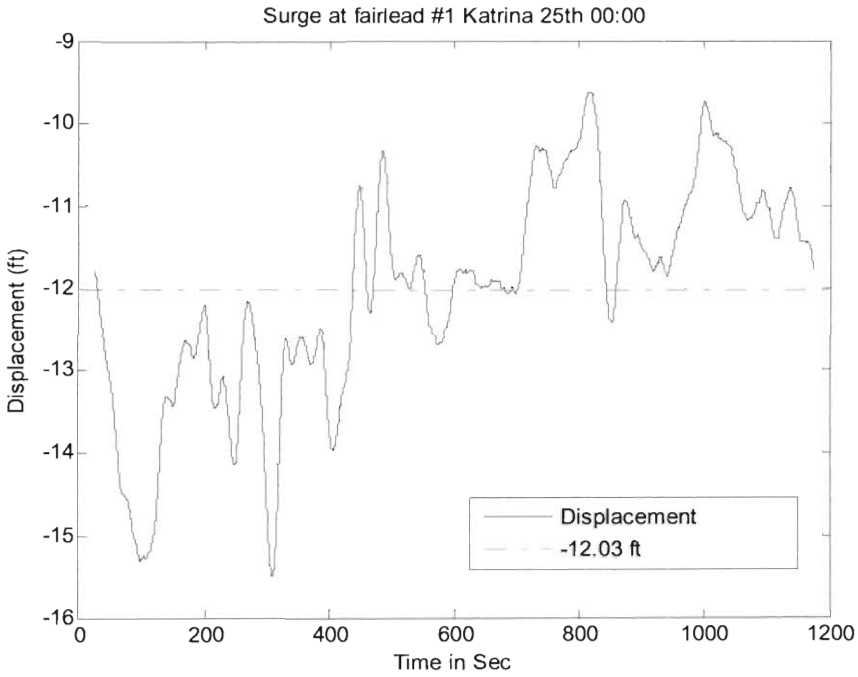

Figure 3.7. Surge fluctuation and mean value over a 20min period of time.

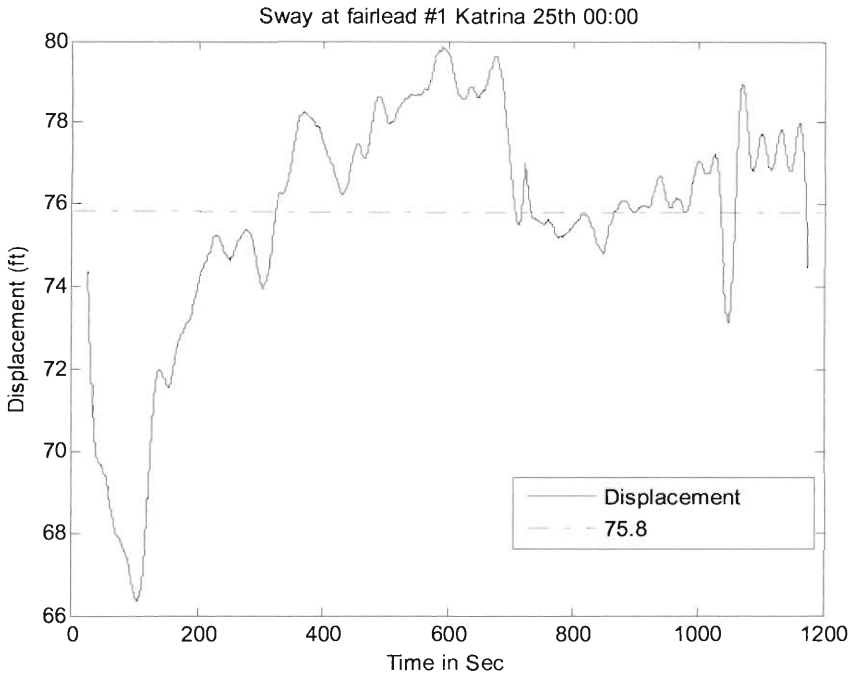

Figure 3.8. Sway fluctuation and mean value over a 20min period of time.

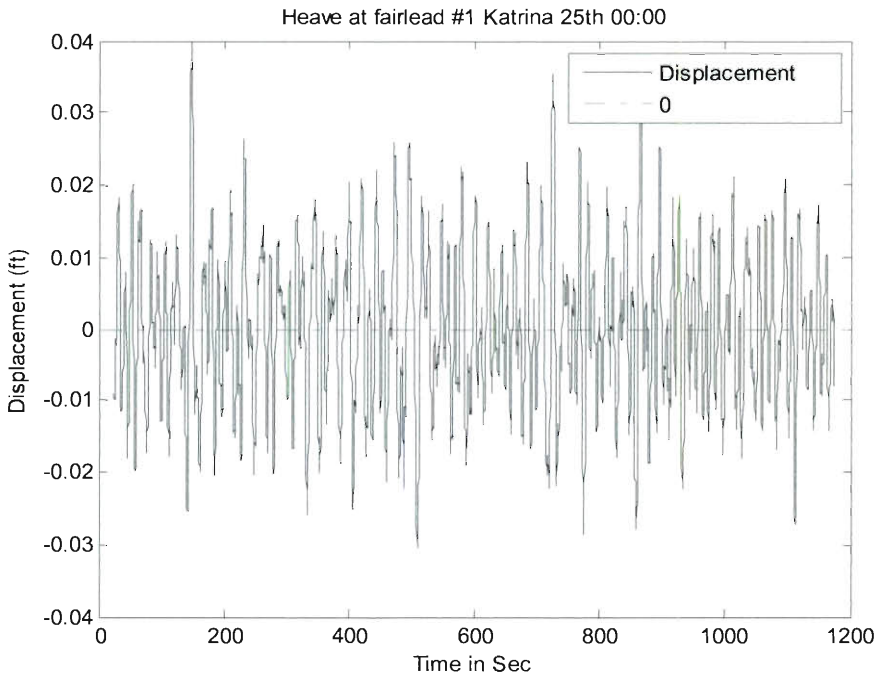

Figure 3.9. Heave fluctuation and mean value over a 20min period of time.

The mean values of surge, sway, heave and the mean values of the tensions for the 25th (00:00) are shown in Figures (3.7, 3.8 and 3.9). Also, the mean values of surge, sway, heave and the mean values of the tensions are available for the 26th (18:20). Figure (3.10) summarizes the obtained results for the L_0 length. Note that after the line rearrangement, there is a contamination in the tension data and the curves are not crossing, this suggests that the chain lock tension measuring devices may introduce inaccuracies in adverse operations.

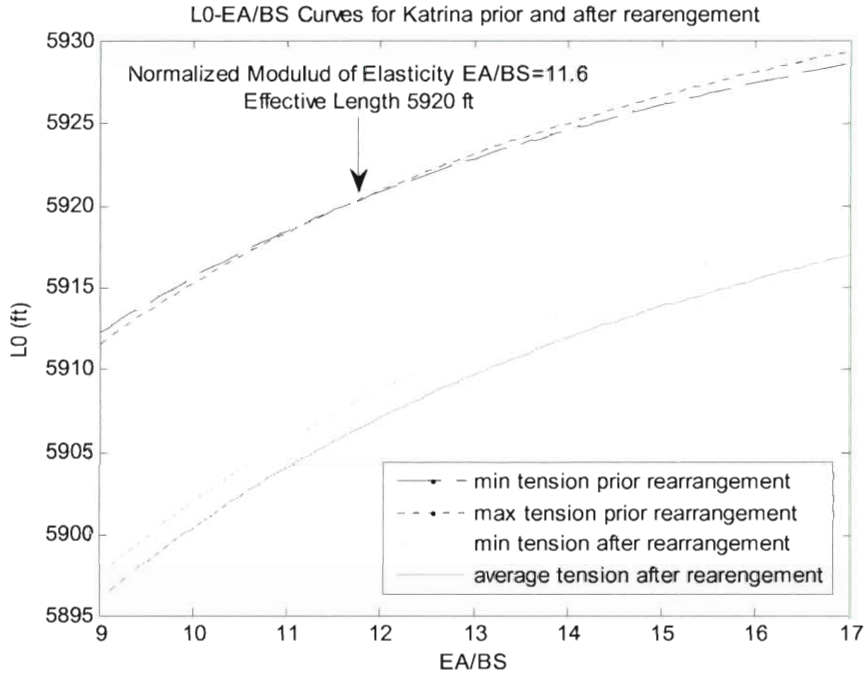

Figure 3.10. Effective 'elastic' length versus 'static' stiffness of polyester rope

Once obtaining the EA coefficient as 11.6BS and the L_0 (equivalent zero stress length) 5920 (ft) for the static conditions (calm sea), one can proceed to the developed sea conditions by assuming L_0 is known, while is EA unknown (attempt to find a dynamic stiffness coefficient). However, before the new inputs

are considered, a validation of the above EA coefficient is done for the entire 20min file of the 25th (calm sea). In this regard, it can be seen in Figure (3.11) that the EA coefficient fluctuates from 9BS to 13BS with the average value of 11.67BS; obviously the fluctuation is caused by noise of the input.

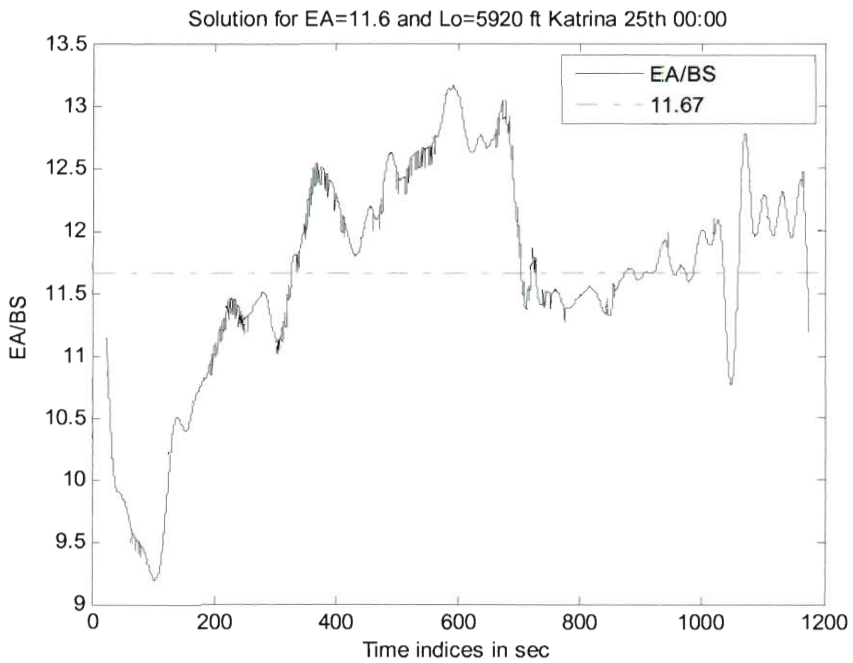

Figure 3.11. 'Static' stiffness fluctuation and mean value over a 20min period of time

3.6 Capturing Polyester's Constitutive Law

3.6.1 Non linear viscoelastic model

The introduction of polyester mooring lines as a permanent anchoring system of offshore platforms and floating production storage and offloading vessels (FPSO) has reduced significantly the costs of the construction for the anchored system. However, the design phase is usually hindered by the high nonlinearity of the material. Specifically, the stiffness of polyester depends on the mean load, the amplitude and the frequency of the excitation. Further, for static loading, the material exhibits permanent in-elastic deformation due to the construction creep. Several researchers have made a concerted effort to model the stiffness of polyester using pertinent laboratory data. Specifically, in Fernandes et all (1999) a linear combination was used for the modulus of elasticity of polyester that depends on the mean load, amplitude and period of the excitation. Then, the underlying coefficients were obtained from least-squares minimization techniques. Also, hysteretic characteristics and fading memory effects were reported. In Casey and Banfield (2005) it was concluded that the effects of construction creep of the polyester are of significant importance, and the stiffness dependency on loading at high frequencies is less important than that at lower frequencies. Also, the polyester rope is becoming stiffer with increasing number of load cycles. During storm cycling loads the viscoelastic-plastic effects are important since they introduce length recovery of the polyester rope. In Huntley (2006) the issue of length and static modulus determination was considered using laboratory experiments. It was concluded that the pre-tension load effects

significantly the construction stretch of the rope and that the static stiffness before pretension should be used for determination of the elastic deformation of the rope. Further, the stiffness of the stretched rope determines the offset of the vessel. In Crudu (1997) experimental results showed clearly that the stiffness of polyester increases with the amplitude and frequency of the excitation. In (Fernandes and Rossi 2002; Fernandes and Rossi 2005) the effects of the full scale polyester ropes were approximated in quite satisfactory manner by introducing a smaller scale model. In Tahar and Kim (2008) a coupled dynamic analysis was conducted for an offshore platform with polyester mooring lines. In Kim Ding (2004) a polyester stiffness model (see Fernandes et all 1999; Fernandes and Rossi 2005) was enhanced by adding a rate dependent term. This, in essence introduces a Voigt model; the significance of the static modulus in determining the offset of the anchored vessel was reported.

In the preceding context, it is clear that polyester is a non linear material with hysteretic, rate dependent, and fading memory features. In this context, the significance of fractional calculus in addressing these issues has been noted. In (Nutting 1921; Scot-Blair 1949; Gemant 1936; Gemant 1938; Grunwald 1867) the fractional calculus was introduced and the first results in modeling visco-elastic behavior and general strain-stress relationships were reported. In Podlubny (1999) several examples were presented in modeling real materials such as wires and ropes using the concept of fractional derivatives. In (Caputo 1974; Bagley and Torvik 1986; Adolfson et all 2005) the response of vibrating viscoelastic materials including fading memory effects were introduced and the effectiveness

of capturing the viscoelastic behavior using fractional derivatives were reported. In (Galucio et all 2005; Schmidt and Gaul 2002) a finite element formulation was introduced for treating viscoelastic constitutive equations with fractional derivatives of time. In (Bossemayer 2001; Lu 2006; Enelund and Olson 1999) the effectiveness of modeling frequency dependent materials with fading memory effects was shown. In (Hwang and Wang 1998; Koh and Kelly 1990; Makris 1994; Makris and Constantinou 1991; Makris and Constantinou 1992) the application of fractional Maxwell and Kelvin models in modeling viscoelastic fluids, high damping rubber bearings and other materials was used to predict the response of base isolated structures under earthquake excitation.

In the preceding context, the data collected from the Gulf of Mexico during Hurricane Katrina are utilized herein in conjunction to the fractional calculus and generalized material models to derive a reliable constitutive equation governing the modulus of elasticity of polyester operating in service conditions. Specifically, from the morning of the 27^{th} to the 28^{th} midnight there are 140 available 20min files. From these files the tension and their underlying displacements are considered as input to the model with known L_0 (5920 ft) of the mooring line. Clearly, from the model in the preceding chapter, the time histories of the tension at the 2^{nd} segment of the line shown in Figure (3.2) can be obtained. Figure (3.12), (3.13) and (3.14) shows the tension at the tip of the line, the underlying strain and the dynamic modulus with respect to time on highly disturbed seas prior to the actual hurricane peak values.

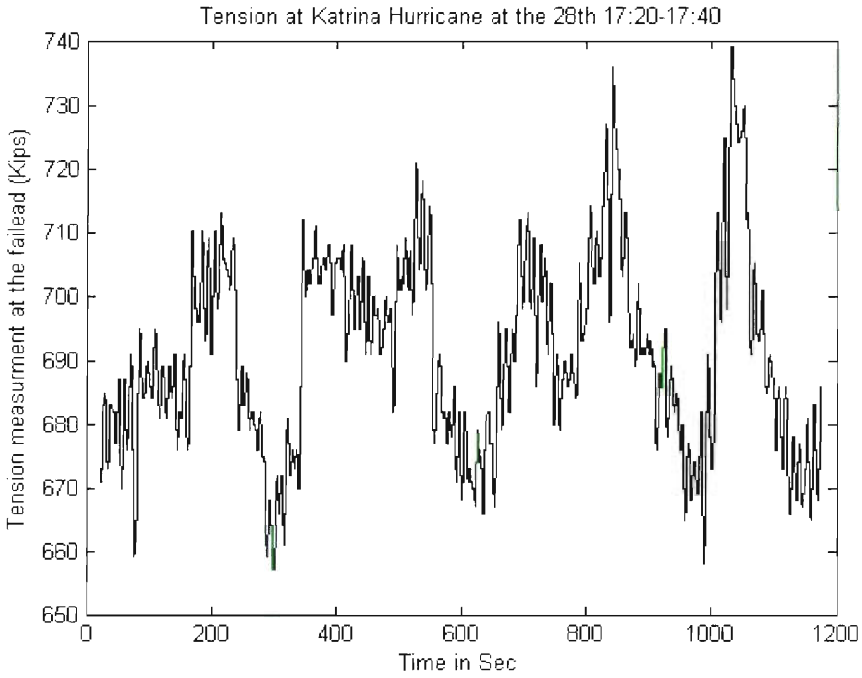

Figure 3.12. Tension at the fairlead for disturbed sea conditions.

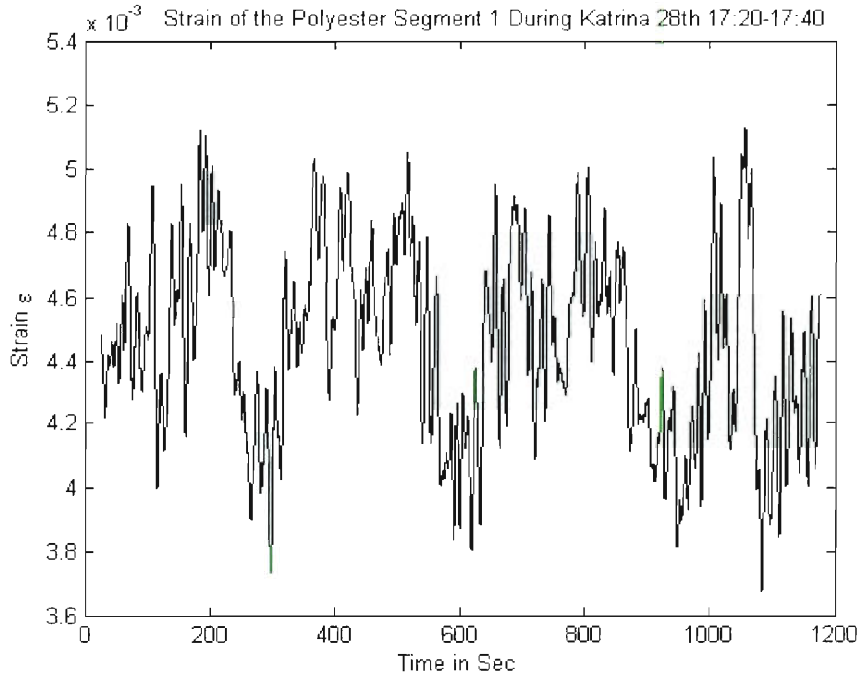

Figure 3.13. Strain of the 2nd polyester rope shown in Figure (3.2) obtained by the Gauss-Newton minimization algorithm for the tension shown in Figure (3.12).

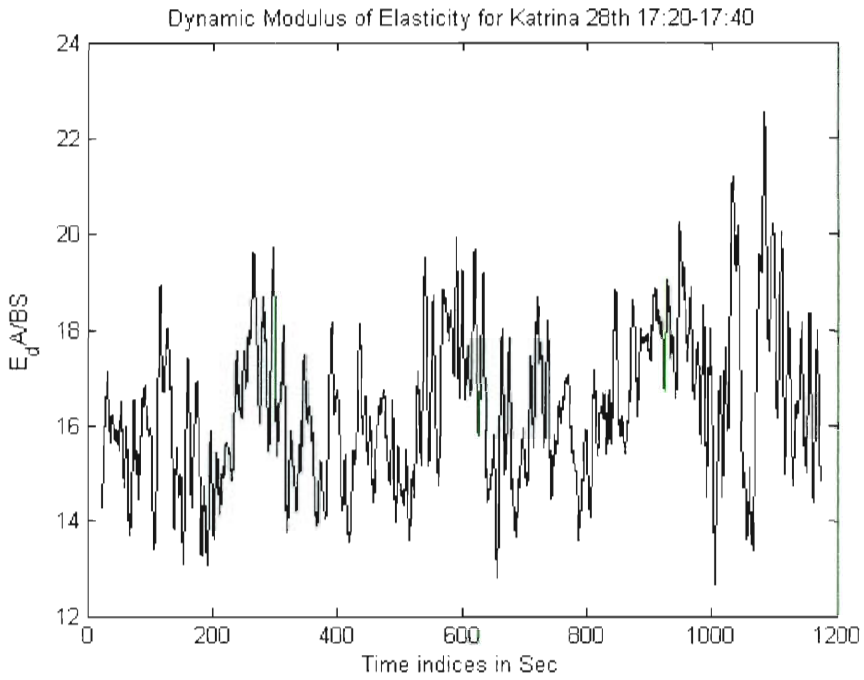

Figure 3.14. 'Dynamic' stiffness fluctuation over a 20 minute period of time for disturbed sea conditions obtained from the tension and strain shown in Figures (3.12) and (3.13).

Next, having the tension and the strain time histories of the 2nd polyester segment of the line shown in Figure (3.2) leads to the identification of the constitutive equation of polyester for dynamic loading. In this context, prior to proceeding to the proposed model definition, certain linear viscoelastic models are introduced. Specifically, the Maxwell, Voigt and Zener models are shown in Figure (3.15). Obviously, these viscoelastic models are obtained by combining purely viscous dampers with purely elastic Hookean springs. Further, more elaborate models can be generated by combining several other dashpots and springs. The governing constitutive equations of the herein considered viscoelastic models are:

$$\sigma + \frac{c}{k}\frac{d\sigma}{dt} = c\frac{dx}{dt}, \tag{3.29 a}$$

for the Maxwell model;

$$\sigma = c\frac{dx}{dt} + kx, \tag{3.29 b}$$

for the Kelvin-Voigt model, and finally; and

$$\sigma + \frac{c}{k_2}\frac{d\sigma}{dt} = c\frac{k_1 + k_2}{k_2}\frac{dx}{dt} + k_1 x, \tag{3.29 c}$$

for the standard linear solid or Zener model.

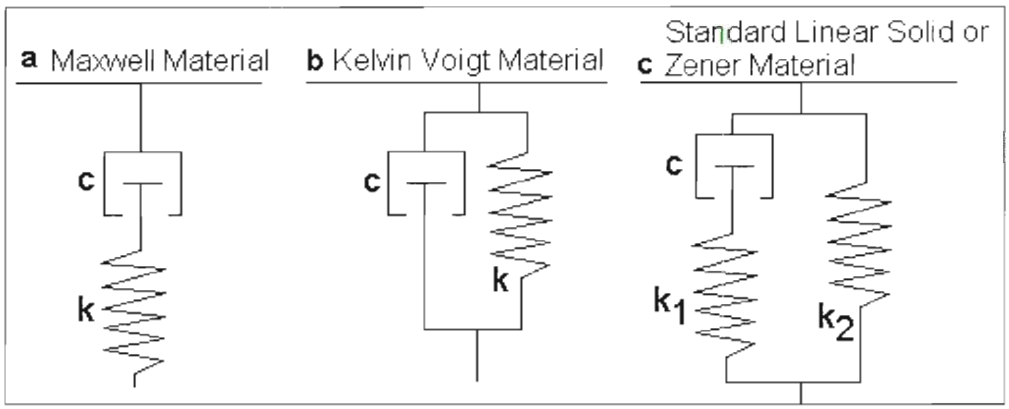

Figure 3.15. The Maxwell, Kelvin-Voigt and Zener viscoelastic models.

Obviously, the Maxwell model affords modeling permanent deformations, and thus it is appropriate for accurately capturing relaxation of solid materials and fluids. The Kelvin-Voigt model, however, is quite ineffective in modeling relaxation but excellent in modeling creep. For the elimination of the difficulties that the Maxwell and Kelvin-Voigt models are exhibiting in capturing both creep and relaxation, the standard linear solid model (Zener) was introduced. Specifically the Zener model affords to capture both creep and relaxation phenomena quite accurately (see Podlubny 1999). Next, substituting the purely viscous damper with elements governed by fractional derivatives (Podlubny

1999) yields the generalized Maxwell, Kelvin-Voigt and Zener models. The governing constitutive equations of the generalized viscoelastic models is

$$\sigma + \frac{c}{k}\frac{d^{\alpha}\sigma}{dt^{\alpha}} = c\frac{d^{\beta}x}{dt^{\beta}}, \tag{3.30 a}$$

for the generalized Maxwell model,

$$\sigma = c\frac{d^{\alpha}x}{dt^{\alpha}} + kx, \tag{3.30 b}$$

for the generalized Kelvin-Voigt model; and

$$\sigma + \frac{c}{k_2}\frac{d^{\alpha}\sigma}{dt^{\alpha}} = c\frac{k_1 + k_2}{k_2}\frac{d^{\beta}x}{dt^{\beta}} + k_1 x, \tag{3.30 c}$$

for the generalized Zener model. Note that α and β are real numbers and the operator d^{α}/dt^{α} denotes fractional differentiation.

In this context, the proposed constitutive equation to model polyester ropes involves a non linear extension of the Zener model. Specifically, the springs are non linear and the non linear dissipative elements depend on the fractional derivative of strain. The non linear springs adopted herein and the non linear dissipative elements governed by fractional derivatives are of the polynomial type. Thus, the constitutive equation of the proposed model is cast in the form

$$\sigma + \eta_0 \frac{d^{\alpha}\sigma}{dt^{\alpha}} = g(\varepsilon) + h\left(\frac{d^{\beta}\varepsilon}{dt^{\beta}}\right), \tag{3.31}$$

where the symbols g and h denote the polynomials

$$g(\varepsilon) = E_0\sqrt{\varepsilon} + \sum_{\substack{j=1 \\ \neq 2}}^{3} E_j \varepsilon^j, \tag{3.32}$$

and

$$h(d)=\sum_{\substack{j=1\\ \neq 2}}^{3}\eta_j\left(\frac{d^{\beta}\varepsilon}{dt^{\beta}}\right)^{j}. \tag{3.33}$$

Note that such a model corresponds to frequency dependent parameters (Nutting 1921; Scot-Blair 1949; Gemant 1936; Gemant 1938; Grunwald 1867). Specifically, it accounts for stiffness and damping being frequency dependent in the frequency domain, and having fading memory effects in the time domain. Therefore, the fitting of a generalized non linear viscoelastic model is adopted herein. Obviously the proposed model affords accurately capturing non linearity of the Duffing type, linear and non linear hysteresis, and linear and non linear dissipative restoring forces.

3.6.2 Polynomial regression

Having the tension time histories of the polyester segment under calm and developed sea conditions and the strain time histories for a quite large period of time before and during the hurricane peak allows for a robust determination of the above described model. Specifically, the general model pursued for identification is given by

$$\sigma+\eta_0\frac{d^{\alpha}\sigma}{dt^{\alpha}}=E_0\sqrt{\varepsilon}+E_1\varepsilon+E_3\varepsilon^3+\eta_1\frac{d^{\beta}\varepsilon}{dt^{\beta}}+\eta_3\left(\frac{d^{\beta}\varepsilon}{dt^{\beta}}\right)^3, \tag{3.33}$$

where the coefficients α,β, E and η are unknown. Note that the non linear minimization problem poses non trivial challenges since the above described model contains eight unknown parameters. The minimization problem is solved

for the determination of the α,β, E and η coefficients minimizing the error in the least squares sense. Specifically, for a given pair of force F and strain ε time histories, the problem can be cast in matrix form

$$\begin{bmatrix} F_0 \\ \dots \\ F_m \end{bmatrix} + \begin{bmatrix} \dfrac{d^\alpha F_0}{dt^\alpha} \\ \dots \\ \dfrac{d^\alpha F_m}{dt^\alpha} \end{bmatrix} \eta_0 = A \begin{bmatrix} \sqrt{\varepsilon_0} & \dots & \varepsilon_0^3 \\ \dots & \dots & \dots \\ \sqrt{\varepsilon_m} & \dots & \varepsilon_m^3 \end{bmatrix} \begin{bmatrix} E_0 \\ \dots \\ E_3 \end{bmatrix} + A \begin{bmatrix} \dfrac{d^\beta \varepsilon_0}{dt^\beta} & \left(\dfrac{d^\beta \varepsilon_0}{dt^\beta}\right)^3 \\ \dots & \dots \\ \dfrac{d^\beta \varepsilon_m}{dt^\beta} & \left(\dfrac{d^\beta \varepsilon_m}{dt^\beta}\right)^3 \end{bmatrix} \begin{bmatrix} \eta_1 \\ \eta_3 \end{bmatrix}, \quad (3.34)$$

where m is number of discretization points and the symbol F_0, F_1 denotes the calculated tension force at the specific polyester segment at time instant 0, Δt etc. Next, combining Equation (3.34) with the Grunwald-Letnikov expansion shown in Equation (2.7) yields

$$\begin{bmatrix} F_0 \\ \dots \\ F_m \end{bmatrix} + \begin{bmatrix} \sum_{k=0}^{n} GL_k^\alpha F_{0-k} \\ \dots \\ \sum_{k=0}^{n} GL_k^\alpha F_{0-k} \end{bmatrix} \Delta t^{-\beta} \eta_0 = A \begin{bmatrix} \sqrt{\varepsilon_0} & \dots & \varepsilon_0^3 \\ \dots & \dots & \dots \\ \sqrt{\varepsilon_m} & \dots & \varepsilon_m^3 \end{bmatrix} \begin{bmatrix} E_0 \\ \dots \\ E_3 \end{bmatrix} + A \begin{bmatrix} \sum_{k=0}^{n} GL_k^\beta \varepsilon_{0-k} & \left(\sum_{k=0}^{n} GL_k^\beta \varepsilon_{0-k}\right)^3 \\ \dots & \dots \\ \sum_{k=0}^{n} GL_k^\beta \varepsilon_{m-k} & \left(\sum_{k=0}^{n} GL_k^\beta \varepsilon_{m-k}\right)^3 \end{bmatrix} \begin{bmatrix} \Delta t^{-\beta} \eta_1 \\ \left(\Delta t^{-\beta}\right)^3 \eta_3 \end{bmatrix}, \quad (3.35)$$

where n is the number of the past terms taken into account for the fractional derivative estimation, so that

$$GL_n < 10^{-3}. \quad (3.36)$$

Note that the sampling rate of the data is 0.25 seconds and since it is not enough for an accurate estimation of the fractional derivatives. Thus, data interpolation is necessary. In this context, cubic splines are used to reduce the time step Δt from 0.25 to 0.01. Next, since there are not enough past terms for an accurate

estimation of the fractional derivative for the first few initial terms, a number of n initial values must be truncated. Therefore, the reduced problem yields

$$\begin{bmatrix} F_n \\ \dots \\ F_m \end{bmatrix} + \begin{bmatrix} \sum_{k=0}^{n} GL_k^{\alpha} F_{n-k} \\ \dots \\ \sum_{k=0}^{n} GL_k^{\alpha} F_{m-k} \end{bmatrix} \Delta t^{-\beta} \eta_0 = A \begin{bmatrix} \sqrt{\varepsilon_0} & \dots & \varepsilon_0^3 \\ \dots & \dots & \dots \\ \sqrt{\varepsilon_m} & \dots & \varepsilon_m^3 \end{bmatrix} \begin{bmatrix} E_0 \\ \dots \\ E_3 \end{bmatrix} + A \begin{bmatrix} \sum_{k=0}^{n} GL_k^{\beta} \varepsilon_{n-k} & \left(\sum_{k=0}^{n} GL_k^{\beta} \varepsilon_{n-k} \right)^3 \\ \dots & \dots \\ \sum_{k=0}^{n} GL_k^{\beta} \varepsilon_{m-k} & \left(\sum_{k=0}^{n} GL_k^{\beta} \varepsilon_{m-k} \right)^3 \end{bmatrix} \begin{bmatrix} \Delta t^{-\beta} \eta_1 \\ \left(\Delta t^{-\beta} \right)^3 \eta_3 \end{bmatrix}. \tag{3.37}$$

The system of Equations (3.37) is a set of linear equations with respect to the coefficients E and η, and non linear with respect to the parameters α and β. The system is solved for the eight parameters that minimize the Euclidean norm of the error vector. For the cases considered herein, the truncation number n is based on the truncation threshold and it varies with respect to the order of the fractional derivative. The length of the force F and strain ε signals is m=4606 before interpolation, and m=115201 after cubic spline interpolation of the data. Further, to circumvent numerical difficulties due to the small number of strains, the signal is normalized by a scaling coefficient of 10^3, and thus the strain is given in percentage of 10^{-3}. Obviously, the combination that minimizes the error is the best set of parameters. For a 20minute period of time of developed sea conditions, the tension F at the polyester segment is obtained from the preceding chapters and the parameters are specified utilizing the Levenberg-Marquart algorithm (see Nocedal and Wright 2002). Next, these parameters are used to reconstruct the tension of the same polyester segment from other segments of time closer to the hurricane peak using the strain recorded data. Then, the data are compared vis a vis the eight parameter non linear viscoelastic model. The error function is given

as the Euclidean norm of the error vector normalized by the length of the signal and yields

$$error_{(\alpha,\beta,E,\eta)} = \frac{1}{m-n}\left\| \begin{bmatrix} F_n \\ \dots \\ F_m \end{bmatrix} + \begin{bmatrix} \sum_{k=0}^{n} GL_k^{\alpha} F_{n-k} \\ \dots \\ \sum_{k=0}^{n} GL_k^{\alpha} F_{m-k} \end{bmatrix} \Delta t^{-\alpha}\eta_0 - A \begin{bmatrix} \sqrt{\varepsilon_0} & \varepsilon_0 & \varepsilon_0^3 & \sum_{k=0}^{n} GL_k^{\beta}\varepsilon_{n-k} & \left(\sum_{k=0}^{n} GL_k^{\beta}\varepsilon_{n-k}\right)^3 \\ \dots & \dots & \dots & \dots & \dots \\ \sqrt{\varepsilon_m} & \varepsilon_m & \varepsilon_m^3 & \sum_{k=0}^{n} GL_k^{\beta}\varepsilon_{m-k} & \left(\sum_{k=0}^{n} GL_k^{\beta}\varepsilon_{m-k}\right)^3 \end{bmatrix} \begin{bmatrix} E_0 \\ \dots \\ \Delta t^{-\beta}\eta_1 \\ \left(\Delta t^{-\beta}\right)^3 \eta_3 \end{bmatrix} \right\|. \tag{3.38}$$

Utilizing the set of Equations (3.38), the unknown coefficients are obtained, and Equation (3.33) is recast in the form

$$F + 0.49\frac{d^{0.66}F}{dt^{0.66}} = 150\sqrt{\varepsilon} + 26.21\varepsilon + 0.19\varepsilon^3 + 0.15\frac{d^{0.81}\varepsilon}{dt^{0.81}} + 0.13\left(\frac{d^{0.81}\varepsilon}{dt^{0.81}}\right)^3 . \tag{3.39}$$

Obviously the separation of the dynamic modulus from the total modulus poses algebraic difficulties. However, the design requires an effective modulus of elasticity that initiates from the static value and changes with time due to its dynamic component. Thus, the effective modulus is considered herein. Equation (3.33) presents a good approximation for the stiffness of polyester line material. Specifically, the stiffness is affected by the frequency of the loading, it is highly non linear, and for static loading it is time dependent due to relaxation. As is clearly shown in the results, the proposed non linear viscoelastic model captures the behavior of polyester operating in service conditions. Conceivably, the linear generalized Zener model captures the behavior of linear hysteresis in addition to any other creep and relaxation of the material. Thus, an enhanced model that contains non linearity is appropriate for capturing accurately the behavior of polyester. Note that, allowing the model to attain arbitrary values of fractional

derivatives provides superior fitting capabilities of the model. Figures (3.16-3.26) help show the accuracy of the proposed approach in capturing the tension of polyester ropes in service conditions. Further, Figures (3.16-3.26) show the tension as the peak of the hurricane approached the offshore structure until the night of the 28th of August 2005 where the maximum displacements reached the peak values and connection to the platform was lost.

Having established a model for the non linear viscoelastic behavior of the polyester material, the verification of the model is pursued against laboratory experiments. Specifically, experimental data exist for the same kind of polyester ropes involving tension tests. The tension test is simple; the polyester rope is anchored at one side and is pulled on the other side. That is, that the end tip of the rope is pulled at a constant velocity, and the underlying displacement and tension are recorded. Figure (3.27) shows the experimental set up. Figures (3.28) and (3.29) show the applied displacement and recorded tension versus time. Figure (3.30) shows the force-displacement loops for the experimental data, and the proposed non linear viscoelastic model governed by fractional and integer order derivatives; the normalized error is obtained from Equation (3.38). It can be seen from Figure (3.30) that the fractional order derivatives improve the modeling of polyester vis-à-vis the integer order derivatives model.

Further, note that the tension experiments shown in Figure (3.30) were conducted for small tension amplitude. For, from the Figure (3.30) it is seen that the mean tension applied was 800 kips with three cycles of loading of 300 kips amplitude. Note that the installed and tested polyester rope has breaking strength

(BS) of 4261Kips. Therefore, the ratio of the excitation with respect to the breaking strength (BS) of the rope is less 8%, and the ratio of the mean value with respect to the BS is less than 20%. In this context, extensive experimental data on polyester ropes are shown in (Petruska et all 2005) where the dependency of the stiffness on the mean value of the tension is captured by a linear regression model; Figure (3.31) summarizes the findings of similar tension experiments.

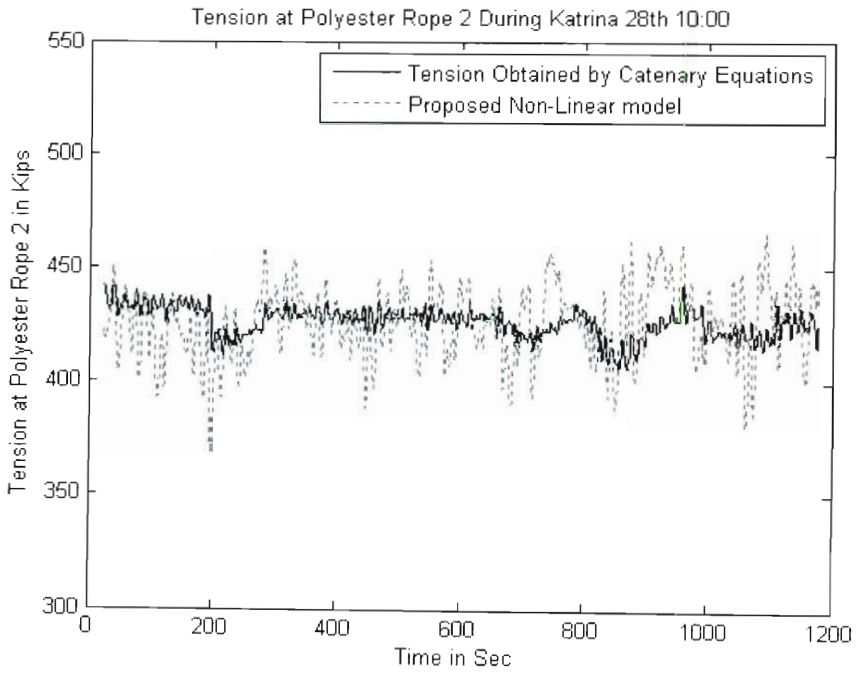

Figure 3.16. Tension at the 2nd polyester rope shown in Figure (3.2) vis a vis the proposed non linear model; n=204, m=115201 and normalized error 4.62%.

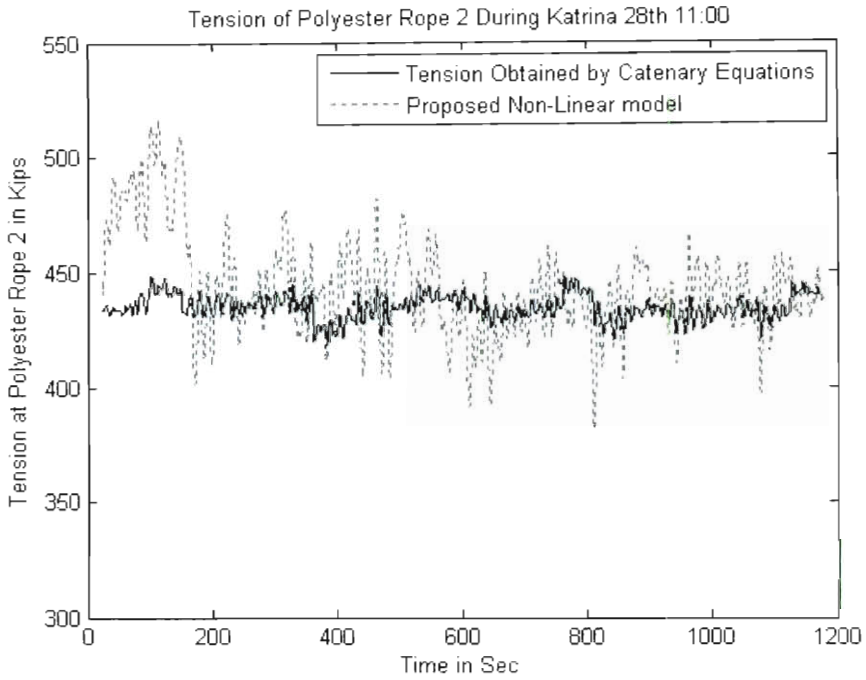

Figure 3.17. Tension at the 2nd polyester rope shown in Figure (3.2) vis a vis the proposed non linear model; n=204, m=115201 and normalized error 6.53%.

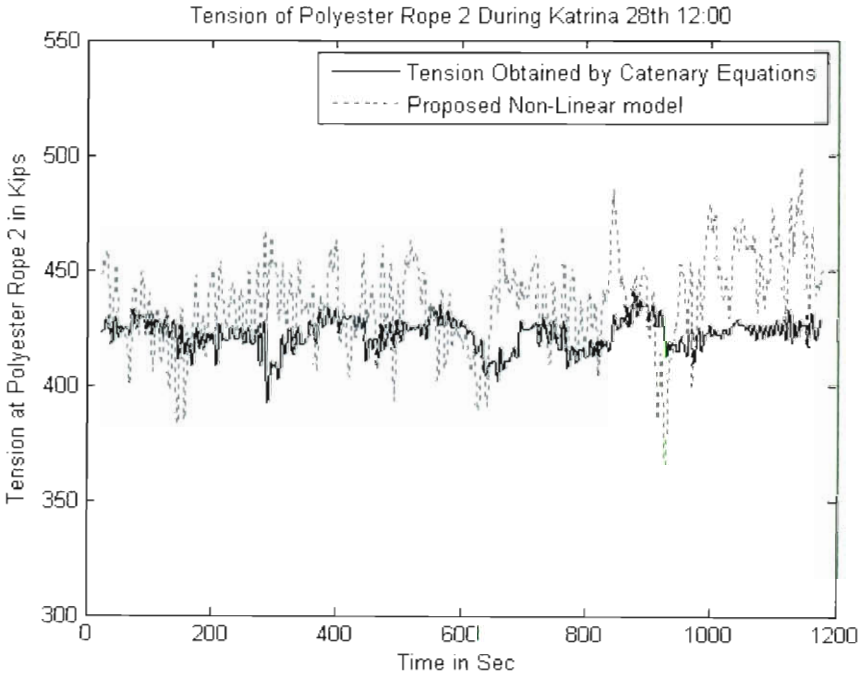

Figure 3.18. Tension at the 2nd polyester rope shown in Figure (3.2) vis a vis the proposed non linear model; n=204, m=115201 and normalized error 6.92%.

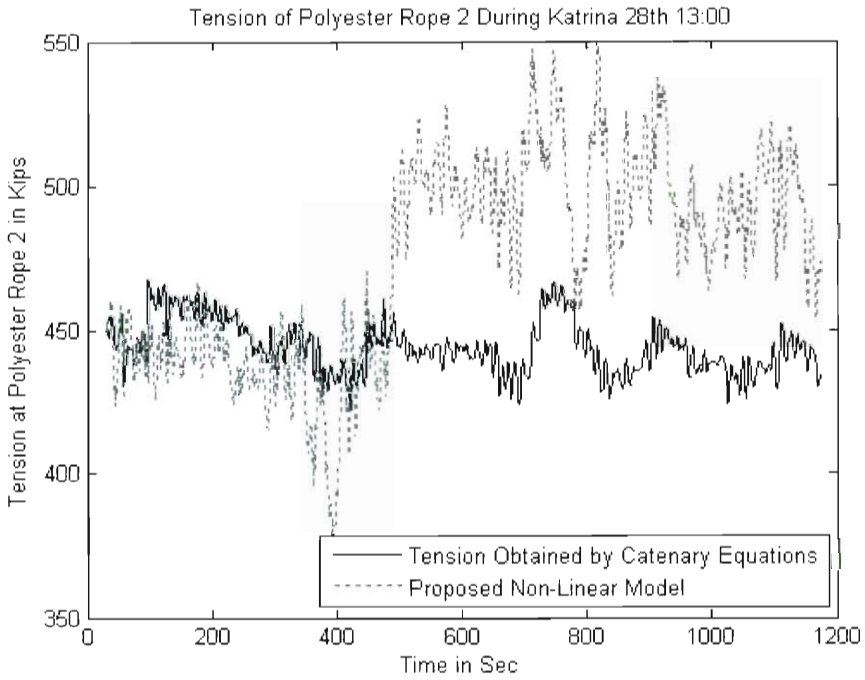

Figure 3.19. Tension at the 2nd polyester rope shown in Figure (3.2) vis a vis the proposed non linear model; n=204, m=115201 and normalized error 13.95%.

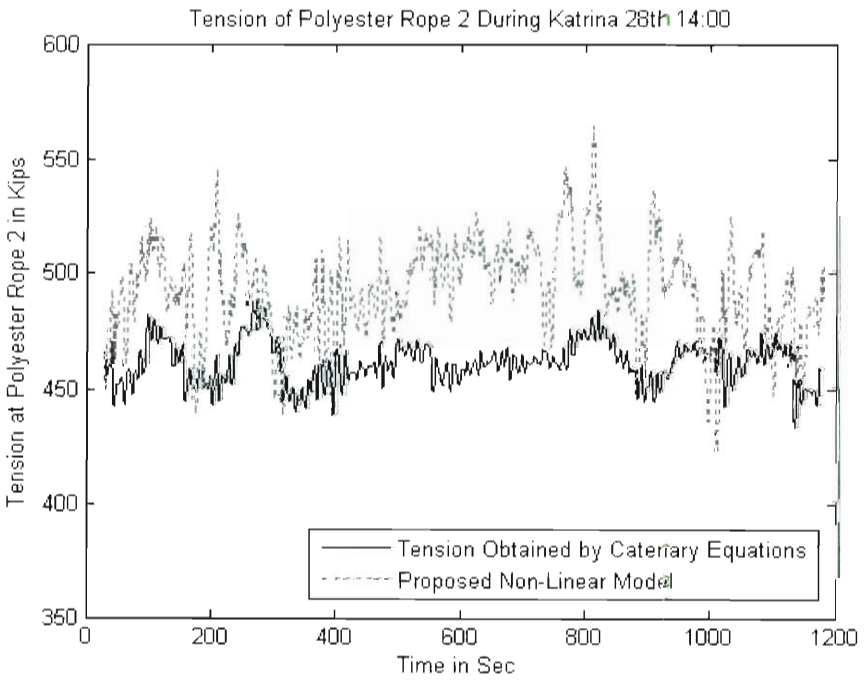

Figure 3.20. Tension at the 2nd polyester rope shown in Figure (3.2) vis a vis the proposed non linear model; n=204, m=115201 and normalized error 10.98%.

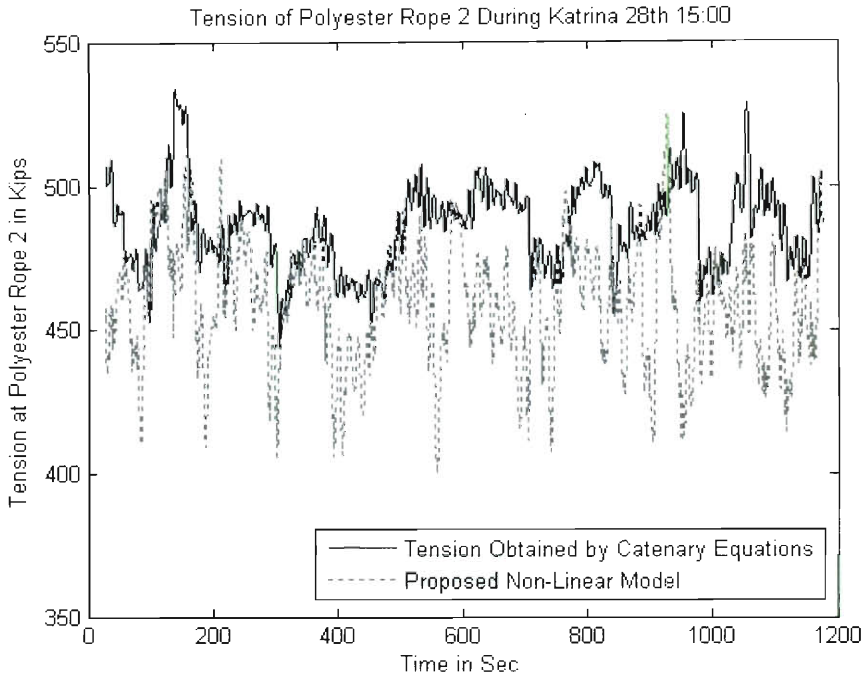

Figure 3.21. Tension at the 2nd polyester rope shown in Figure (3.2) vis a vis the proposed non linear model; n=204, m=115201 and normalized error 10.43%.

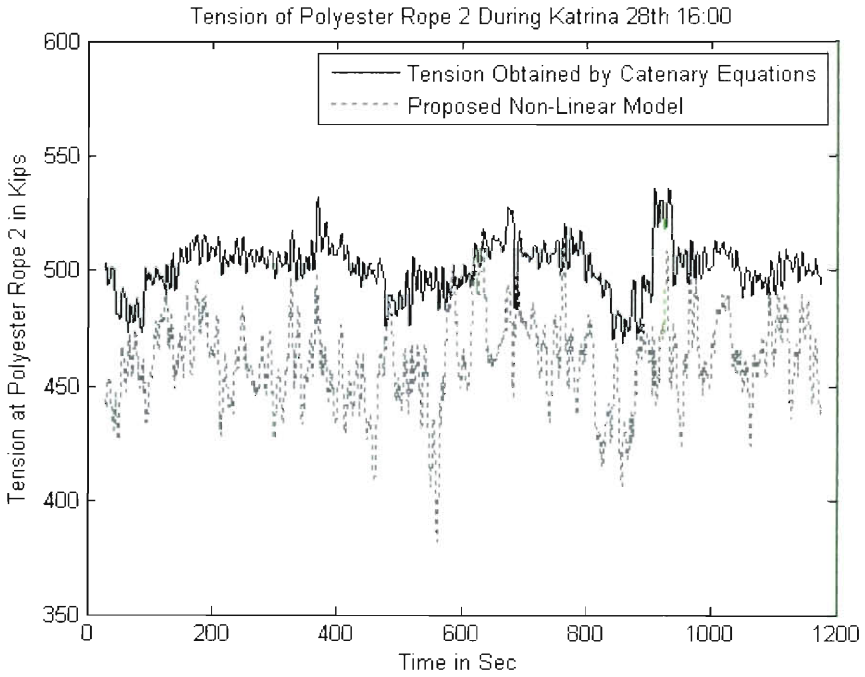

Figure 3.22. Tension at the 2nd polyester rope shown in Figure (3.2) vis a vis the proposed non linear model; n=204, m=115201 and normalized error 13.19%.

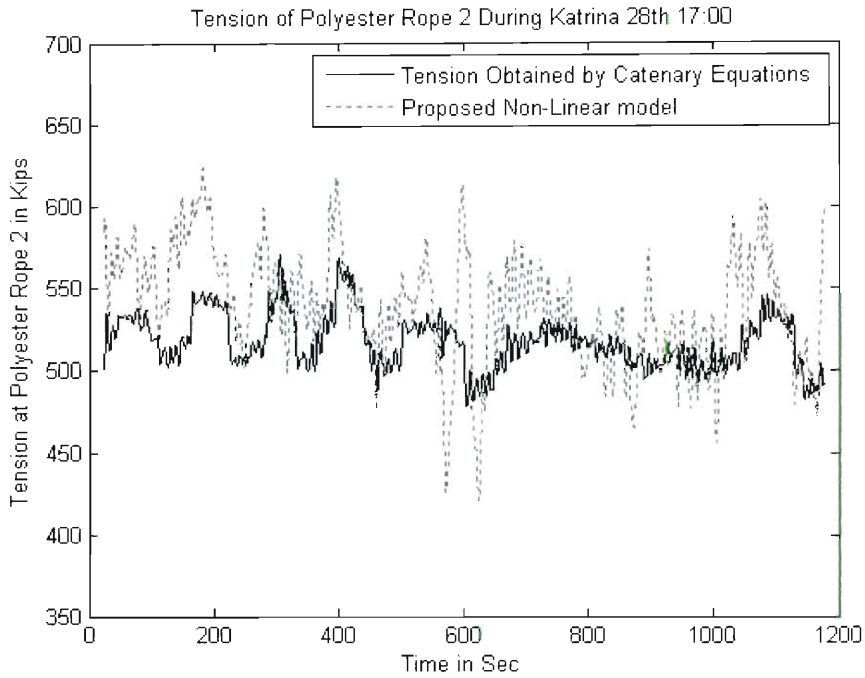

Figure 3.23. Tension at the 2nd polyester rope shown in Figure (3.2) vis a vis the proposed non linear model; n=204, m=115201 and normalized error 10.62%.

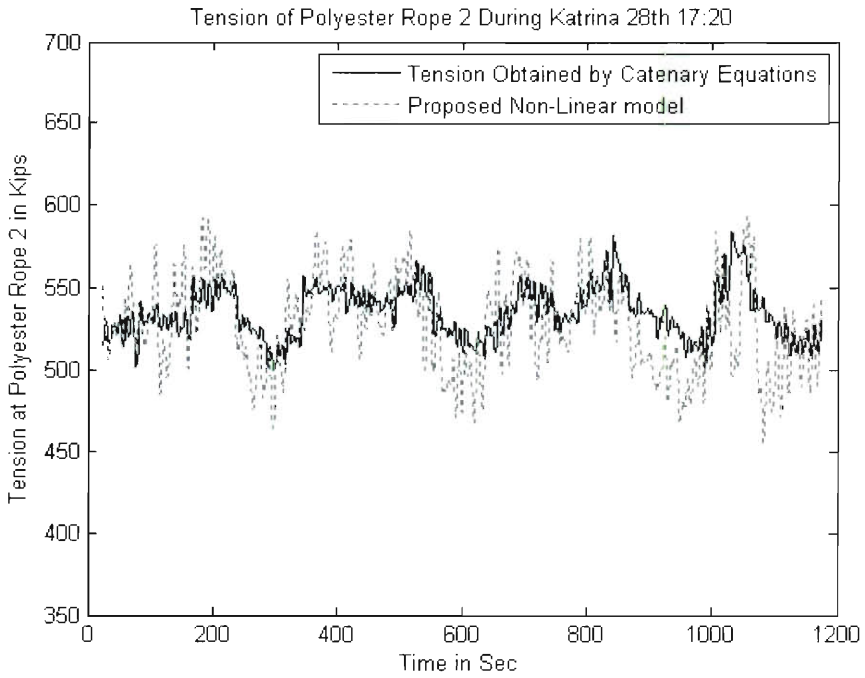

Figure 3.24. Tension at the 2nd polyester rope shown in Figure (3.2) vis a vis the proposed non linear model; n=204, m=115201 and normalized error 7.12%.

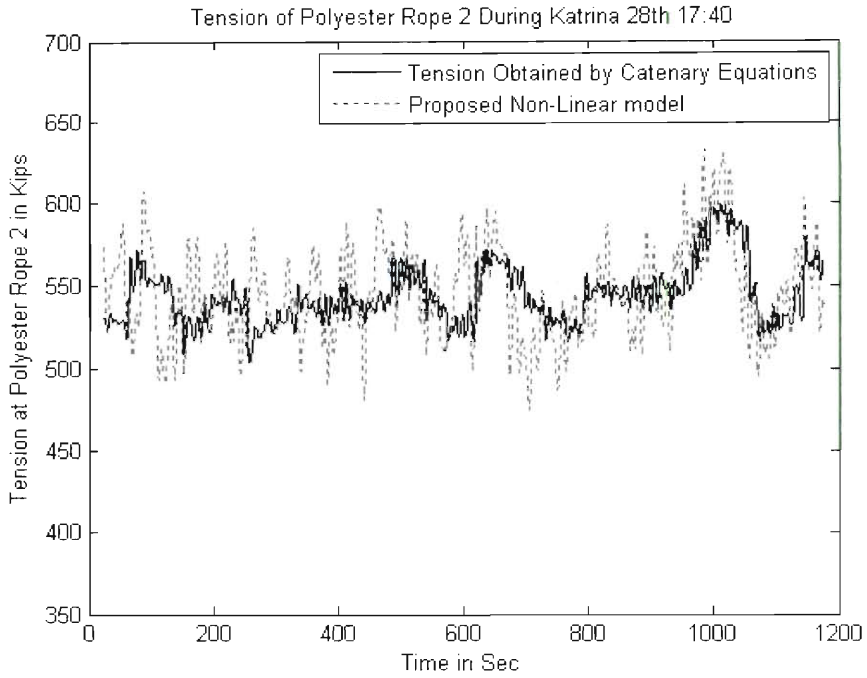

Figure 3.25. Tension at the 2nd polyester rope shown in Figure (3.2) vis a vis the proposed non linear model; n=204, m=115201 and normalized error 7.24%.

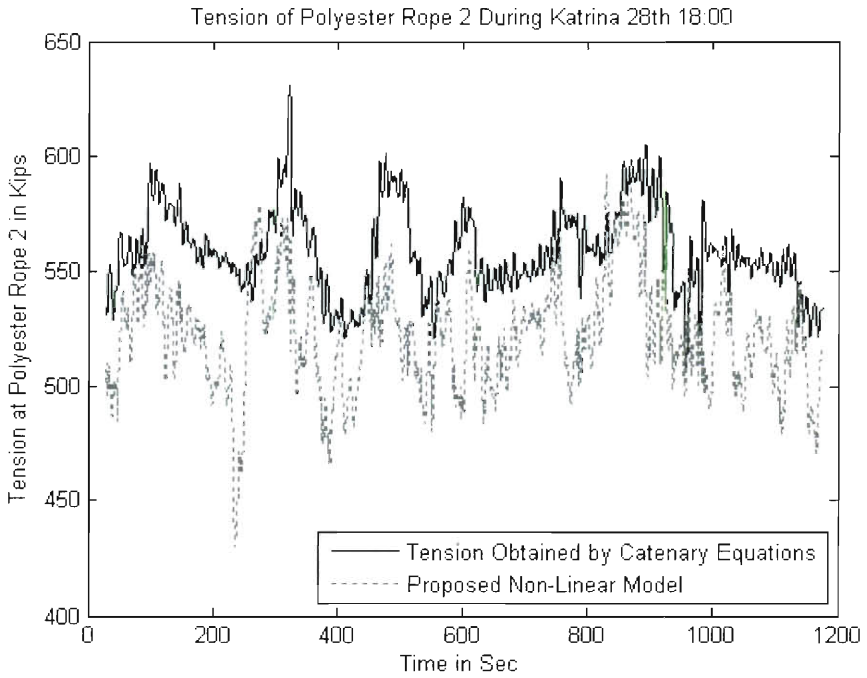

Figure 3.26. Tension at the 2nd polyester rope shown in Figure (3.2) vis a vis the proposed non linear model; n=204, m=115201 and normalized error 12.53%.

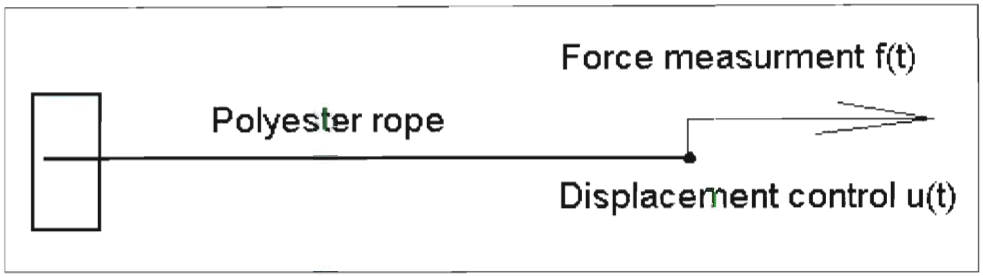

Figure 3.27. Simple experimental set up for identification of the polyester rope stress-strain relationship.

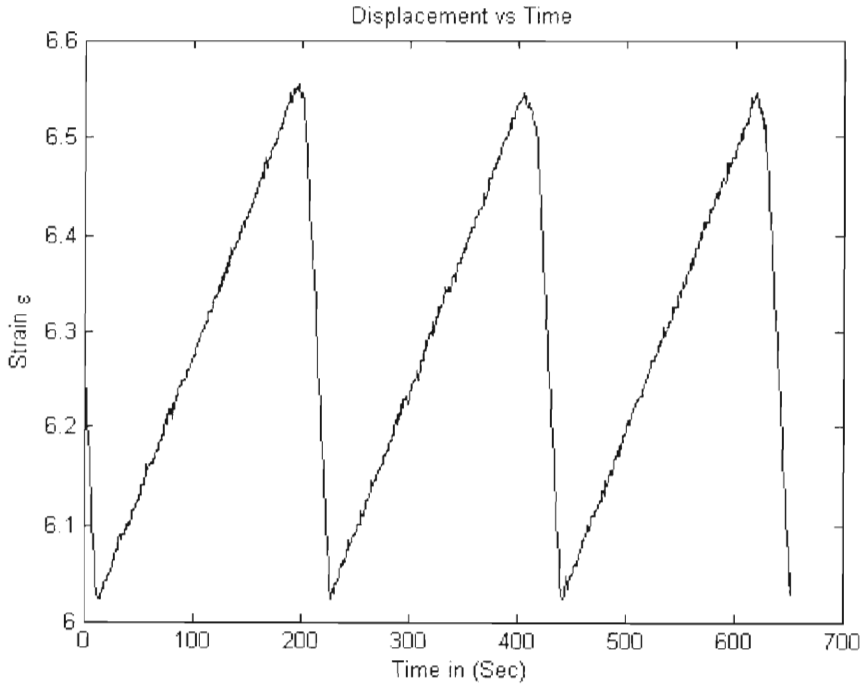

Figure 3.28. Applied displacement at the end tip of the polyester rope.

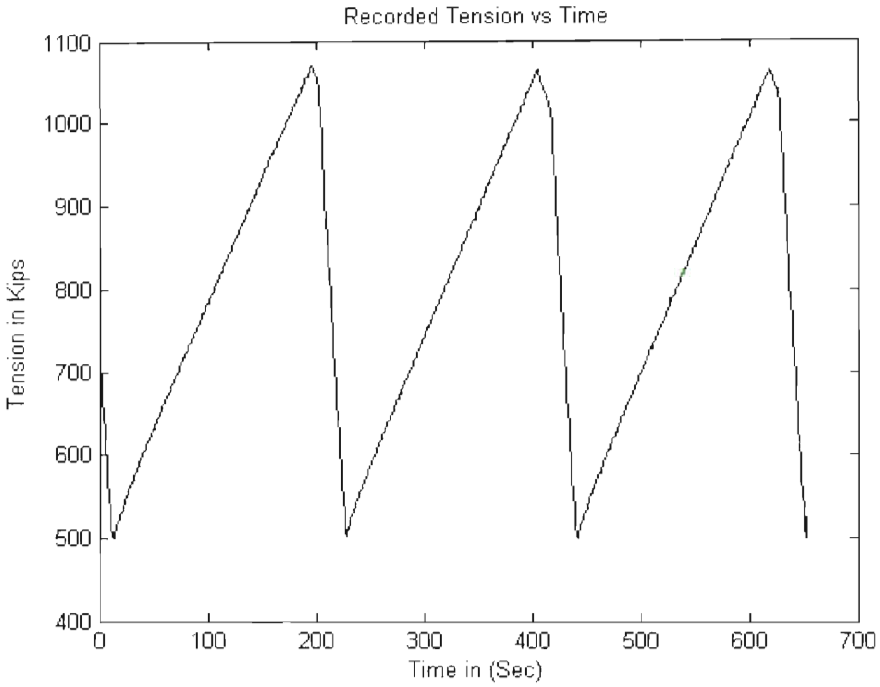

Figure 3.29. Recorded tension for applied displacement of Figure (3.25) at the end tip of the polyester rope.

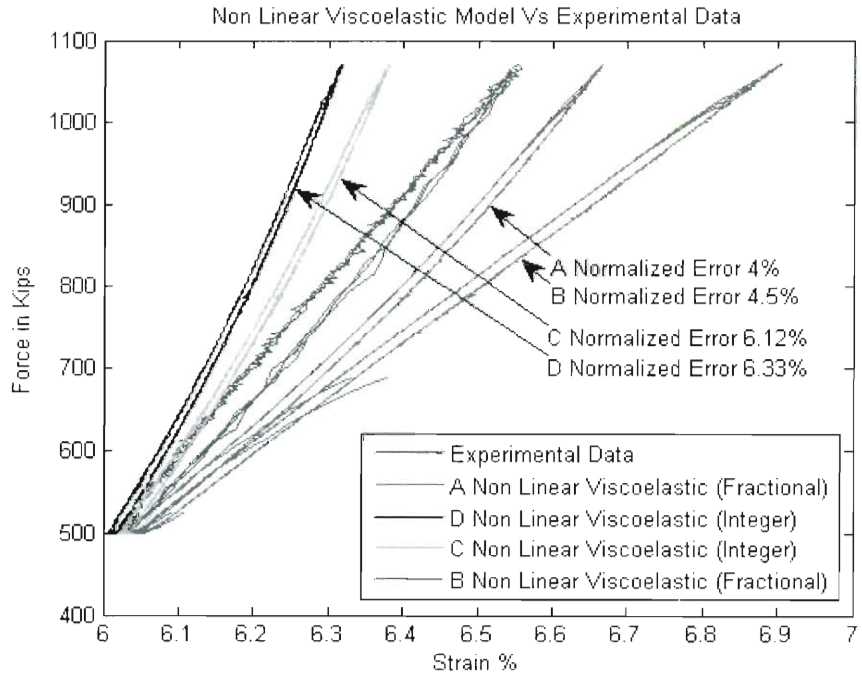

Figure 3.30. Experimental force-strain loops versus the proposed non linear viscoelastic model governed by fractional and integer order derivatives.

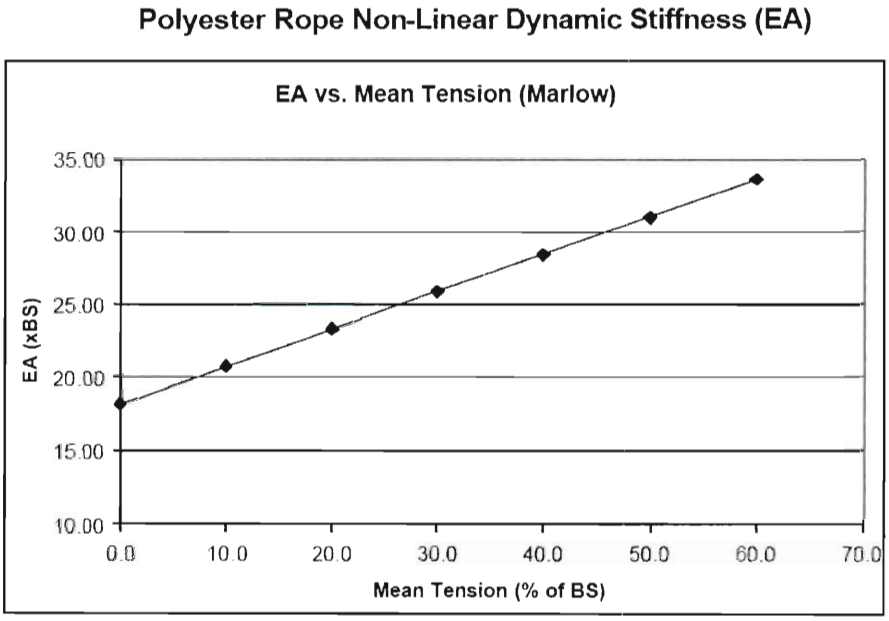

Figure 3.31. The stiffness of a certain polyester rope with respect to the mean tension; Petruska et all (2005).

Chapter 4

Peridynamics Theory of Mechanics

4.1 Introduction

The problem of modeling dynamic or static systems that contain discontinuities is fundamental in mechanics. Fractured surfaces and propagating cracks are discontinuities which disrupt the domain of the differential equations and create mathematical singularities. There are several approaches to deal with these kinds of discontinuities. Two classical approaches are the finite element method (FEM) with re-meshing of the continuous domain, and the extended finite element method (XFEM) which circumvents the constant re-meshing of the domain and uses the same mesh by simply adjusting the stiffness of the cracked element (see Zi and Belytschko 2003; Stolarsca et all 2001; Chessa and Belytschko 2004; Rodenas et all 2010). Further, mesh-free techniques have been applied to the same problem with quite reasonable results (Belytschko et all 1994; Belytschko et all 1995). However, all of these approaches have been based on local mechanics theory. In local mechanics theory, a single point in the medium is in direct contact with only its immediate neighboring points, and thus spatial derivatives exist in such a continuum. In a non-local mechanics, however, a single point in the medium is in direct contact with points further away in addition to its immediate neighboring points. Non-local theories have been initially developed in (Kroner 1967; Edelen 1969, 1970, 1975, Eringen et all 1977; Bazant and Novak 2000; Bazant and Giraudon 2002) and since then several researchers have contributed to this concept (Di Paola and Faila 2008; Di Paola et all 2009; Faila et

all 2010). Silling (2000) extended the concept of non-local mechanics. Until then the non-locality concept was used as a generalization of the local mechanics and assumed that spatial derivatives at a finite neighborhood around the point of interest can be used. Silling (2000) proposed a fully non-local peridynamics modeling in which no spatial derivatives are needed, and therefore the inherent problem of a discontinuity in the domain can be circumvented. The model involves a formulation of a partial integrodifferential equation which holds for discontinuous domains with no additional treatment, like enrichment etc. Since this pioneering work, several publications have focused on the application of this approach to a wide spectrum of problems. In Silling et all (2003) the deformation of an infinite bar was investigated using the peridynamics theory. In Silling et all (2007) a generalization of the original peridynamics framework was proposed to extend the kinds of materials that can be modeled by peridynamics theory. In Bobaru et all (2009) adaptive refinement was proposed, and the uniform convergence of the peridynamics theory to classical mechanics was shown for dynamic and static 1D solutions when the non locality effect is approaching zero. In Warren et all (2009) the previous peridynamics theory was extended to handle Poisson ratios other than ¼, and allow bonds to exhibit non central forces. In Macek and Silling (2007) the peridynamics theory was extended beyond the EMU meshless formulations to the finite element method by incorporating truss elements. In Bobaru (2007) the peridynamics method was used to analyze the effect of the Van der Waals forces on the mechanical behavior, strength and toughness of three dimensional nano-fiber networks. In this benchmark study (see

Bodaru 2007), the fracture was introduced at the micro-structural level using the concept of bonds and it was concluded that two main mechanisms control the deformation: the fiber re-orientation and the fiber accretion. In Silling and Askari (2005) a numerical mesh free method for solving the partial integrodifferential equation arising from the peridynamics theory was proposed and examples of modeling crack growth in brittle materials were presented. In Zhou and Du (2010) a mathematically based approach for linear peridynamics FEM was introduced.

In this chapter a peridynamics modeling of systems with stochastic material properties exposed to stochastic excitations is considered. In this context, a novel spatial discretization of the peridynamics equation is used which allows for a stochastic extension of the model. The governing partial integrodifferential equation is treated by the Kansa collocation method (Kansa 1990; Ling and Kansa 2004; Fedoseyev et all 2002) using the inverse multi-quadric (IMQ) radial basis functions (RBF). In this formulation the direction and length of the crack propagation is not governed by the nodal density and positioning of the nodes as it is in the usual mesh free peridynamics approach. The approach is quite similar to the XFEM (Zi and Belytschko 2003; Wei et all 2010; Baietto et all 2010; Dreau et all 2010; Khoei and Taheri-Mousavi 2010) where the crack, is influencing only one finite element, and only the stiffness of the current element in which crack is going through needs to be determined. Further, the boundary conditions are imposed in a simpler manner than in the peridynamics theory, and it is quite similar to the FEM. Finally, after having established a reliable collocation method to treat the deterministic problem, the stochastic problem is considered and it is

solved utilizing the concept proposed in SFEM (see Ghanem and Spanos 1990). The reliability of the system is assessed by determining the probability density function (PDF) of the energy release rate around the crack tip.

4.2 Peridynamics Formulation

4.2.1 The peridynamics partial integrodifferential equation

Consider a mechanical component having one dimension significantly smaller than the other two, and operating under an excitation in the plane defined by its two significant dimensions. Obviously, the significant displacements of the vibrating medium are on the same 2-D plane. Next, consider the non local peridynamics theory for modeling the behavior of the medium. The non-local theory of peridynamics involves a partial integrodifferential equation for dynamic problems (see Emmrich and Weckner 2007). Specifically, this equation is a second order differential equation with respect to time, and an integral equation with respect to space. In this context, the governing equation of motion of any particle inside the vibrating 2-D medium is given by the equation

$$\rho\begin{bmatrix}\ddot{u}(\underline{x},t)\\ \ddot{v}(\underline{x},t)\end{bmatrix}+\int_{H(\underline{x})} f\left(\begin{bmatrix}u(\underline{x},t)-u(\hat{\underline{x}},t)\\ v(\underline{x},t)-v(\hat{\underline{x}},t)\end{bmatrix},\underline{x}-\hat{\underline{x}}\right)dV_{\hat{\underline{x}}}=\begin{bmatrix}b_x(\underline{x},t)\\ b_y(\underline{x},t)\end{bmatrix}, \qquad (4.1)$$

where $\ddot{u}, \ddot{v}$ denote the second order derivatives of u, v with respect to time; and the vectors $\underline{x}$ and $\hat{\underline{x}}$ are defined by the equations

$$\underline{x} = \begin{pmatrix} x \\ y \end{pmatrix}, \tag{4.2}$$

and

$$\hat{\underline{x}} = \begin{pmatrix} \hat{x} \\ \hat{y} \end{pmatrix}. \tag{4.3}$$

Note, that ρ is the material density, $b_x(\underline{x},t), b_y(\underline{x},t)$ are the force densities in each direction, $u(\underline{x}), v(\underline{x})$ denote the displacements of the point $\underline{x}$ on the x and y axis respectively, f denotes the force function measured in force per unit volume squared exerted on the point $\underline{x}$ by the point $\hat{\underline{x}}$, and $H(\underline{x})$ is the domain of integration. Note that the force function f may depend on the partial derivatives of the displacement with respect to the directions x, y, and thus Equation (4.1) is a partial integrodifferential equation. In the peridynamics theory the domain of $\hat{\underline{x}}$ is restricted by the position of $\underline{x}$ by defining the relative position $\underline{\xi}$

$$\underline{\xi} = \underline{x} - \hat{\underline{x}}, \tag{4.4}$$

such that

$$\left|\underline{\xi}\right| < \delta. \tag{4.5}$$

The distance δ is called the horizon and represents the distance of the non local approximation. The domain $H(\underline{x})$ for every given point $\underline{x}$ is defined by the equation

$$H(\underline{x}) = \{\forall \hat{\underline{x}}, \left|\underline{x} - \hat{\underline{x}}\right| < \delta\}, \tag{4.6}$$

and yields a circular disc centered at $\underline{x}$ of radius δ; Figure (4.1) helps to elucidate this concept.

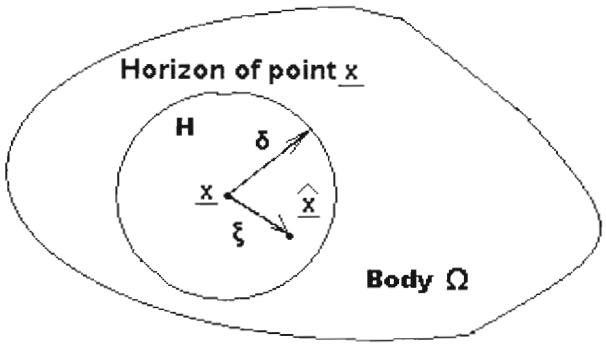

Figure 4.1. Each point $\underline{x}$ in the body Ω interacts directly with the points $\hat{\underline{x}}$ in the circular disc $H(\underline{x})$ through bonds.

Further, the pair-wise force-function f, represents the force between two particles separated by a distance of length ξ (see Silling 2000). Thus, it must exhibit the properties

$$f(-\underline{\eta},-\underline{\xi}) = -f(\underline{\eta},\underline{\xi}), \tag{4.7}$$

and

$$(\underline{\xi}+\underline{\eta}) \otimes f(\underline{\eta},\underline{\xi}) = 0, \tag{4.8}$$

where $\otimes$ is the symbol of the tensor product, and the vector $\underline{\eta}$ is defined by the equation

$$\underline{\eta} = \begin{bmatrix} u(\underline{x}) - u(\hat{\underline{x}}) \\ v(\underline{x}) - v(\hat{\underline{x}}) \end{bmatrix}. \tag{4.9}$$

The above restrictions ensure the conservation of angular momentum, and the co-linearity of the force with respect to the relative position of the particles.

Extensive details on the force function can be found in Silling (2000). Next, for the linearized pair-wise force-function introduced in Silling (2000), the force yields

$$f(\underline{\eta},\underline{\xi}) = C(\underline{\xi})\underline{\eta}, \tag{4.10}$$

where the micro-modulus C satisfies the condition

$$C(-\underline{\xi}) = C(\underline{\xi}). \tag{4.11}$$

A fundamental measure of the peridynamics theory is the bond stretch given by the formula

$$s = \frac{\left|\underline{\xi}+\underline{\eta}\right| - \left|\underline{\xi}\right|}{\left|\underline{\xi}\right|}. \tag{4.12}$$

Specifically, stretch is used to determine whether the bond has failed or not, and thus it is the measure governing the force between the particles such as the strain in classical mechanics theory. Bonds which have exceeded the predetermined value of s_0 are damaged. In quantifying the damage on a specific point $\underline{x}$ from the points in the horizon of $\underline{x}$ the function

$$\varphi(\underline{x},t) = 1 - \frac{\int_{H(\underline{x})} \mu(\underline{x},t,\underline{\xi})\, dV_{\underline{\hat{x}}}}{\int_{H(\underline{x})} dV_{\underline{\hat{x}}}}, \tag{4.13}$$

is used, where the damage can be assumed to be of total failure of the bond by

$$\mu(\underline{\xi},t)=\begin{Bmatrix}1\\0\end{Bmatrix}\begin{matrix}s(t,\underline{\xi})<s_0\\ Otherwise\end{matrix}. \tag{4.14}$$

In linear peridynamics, the pair-wise force amplitude is given by the equation in (Silling 2000; Silling and Askari 2005)

$$\left|f(\underline{\eta},\underline{\xi})\right|=c\frac{\left|\underline{\eta}\right|}{\left|\underline{\xi}\right|}, \tag{4.15}$$

where the force vector f is aligned with the vector $\underline{\xi}+\underline{\eta}$, and for a 2-D plate problem the constant c is given by the equation

$$c=\frac{72k}{5\pi\delta^3} \tag{4.16}$$

where k is the bulk modulus of the material in Emmrich and Weckner (2007). Several other formulations can be found in Silling (2000) regarding the pair-wise force-function.

4.2.2 Polar coordinate transformation

Equation (4.1) can also be cast into polar coordinates yielding

$$\rho\begin{bmatrix}\ddot{u}(\underline{x},t)\\ \ddot{v}(\underline{x},t)\end{bmatrix}+\int_{H(\theta,r)} f\left(\begin{bmatrix}u(\underline{x},t)-u(\underline{x}+\underline{r},t)\\ v(\underline{x},t)-v(\underline{x}+\underline{r},t)\end{bmatrix},-\underline{r}\right)\left|J\right|d\theta dr=\begin{bmatrix}b_x(\underline{x},t)\\ b_y(\underline{x},t)\end{bmatrix}, \tag{4.17}$$

where

$$\left|J\right|=-r, \tag{4.18}$$

$$\underline{r} = -\underline{\xi}\,, \tag{4.19}$$

and

$$\underline{r} = r\begin{pmatrix}\cos\theta\\ \sin\theta\end{pmatrix}. \tag{4.20}$$

Note that the Equation (4.9) in the polar coordinates yields

$$\underline{\eta} = \begin{bmatrix} u(\underline{x}) - u(\underline{x}+\underline{r}) \\ v(\underline{x}) - v(\underline{x}+\underline{r}) \end{bmatrix}, \tag{4.21}$$

and equivalently Equation (4.15) yields

$$\left| f(\underline{\eta},\underline{r}) \right| = \frac{c}{r}\left|\underline{\eta}\right|. \tag{4.22}$$

For illustration purposes, the displacements u and v of a bond are shown in Figure (4.2).

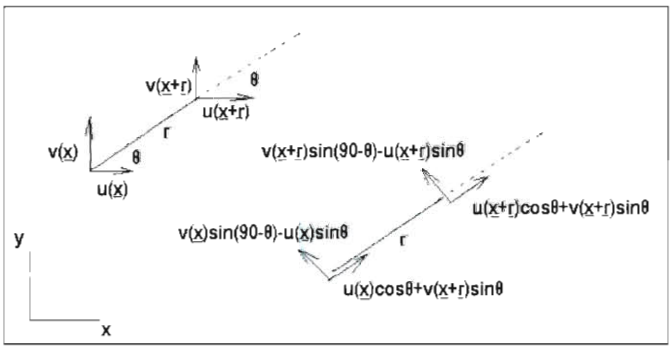

Figure 4.2. A bond of length r and angle θ with respect to the global coordinate system.

Adopting the linearized pair-wise force-function, and using the fact that the horizon δ is a small distance, the total stretch of the bond can be approximated accurately by just the collinear component to the vector $\underline{r}$. The contribution to the extension of the bond from the perpendicular displacements with respect to the

vector $\underline{r}$ shown in Figure (4.2), can be neglected for small distances r. This is due to the assumption that small rigid body rotations of the bond can be neglected (B.3). With this assumption, and since this force is on the direction of the vector $\underline{r}$ the forces per unit volume on the x and y direction yield

$$force_x = \frac{c}{r}\Big((u(\underline{x}) - u(\underline{x}+\underline{r}))dV_{\underline{x}+\underline{r}}\cos\theta + (v(\underline{x}) - v(\underline{x}+\underline{r}))dV_{\underline{x}+\underline{r}}\sin\theta\Big)\cos\theta$$
$$force_y = \frac{c}{r}\Big((v(\underline{x}) - v(\underline{x}+\underline{r}))dV_{\underline{x}+\underline{r}}\cos\theta + (v(\underline{x}) - v(\underline{x}+\underline{r}))dV_{\underline{x}+\underline{r}}\sin\theta\Big)\sin\theta \quad . \tag{4.23}$$

These equations represent the force at the x and y direction due to one bond formed from 2 particles in distance r and in angle from the reference point θ. Since Equation (4.17) is given in polar coordinates, Equation (4.1) can be cast as

$$\rho\begin{bmatrix}\ddot{u}(\underline{x},t)\\ \ddot{v}(\underline{x},t)\end{bmatrix} + \int_0^{\delta}\int_0^{2\pi}\frac{c}{r}\begin{bmatrix}\cos^2\theta & \cos\theta\sin\theta\\ \cos\theta\sin\theta & \sin^2\theta\end{bmatrix}\begin{pmatrix}u(\underline{x},t) - u(\underline{x}+\underline{r},t)\\ v(\underline{x},t) - v(\underline{x}+\underline{r},t)\end{pmatrix}|J|\,d\theta dr = \begin{bmatrix}b_x(\underline{x},t)\\ b_y(\underline{x},t)\end{bmatrix}. \tag{4.24}$$

4.3 Spatial Discretization

4.3.1 Radial basis function expansion

Having derived Equation (4.24), proceed to use the Kansa collocation method for its spatial discretization; see Kansa (1990). In implementing the Kansa collocation method, a series of nodes is distributed in the domain forming a grid of points. The inverse multi-quadrics (IMQ) radial basis functions (RBF's) are used as defined in (Kansa 1990) and correspond to the inverse of the Euclidean distance of the point $\underline{x}$ from the collocation node k

$$g_k(\vec{x}) = \frac{1}{\sqrt{(x-x_k)^2 + (y-y_k)^2 + \psi_k^2}}, \tag{4.25}$$

where the distance ψ_k is a local shape parameter regulating the shape of the basis. Large values of this parameter contribute to smoother shapes and are quite accurate approximations of flat and slowly varying solutions. However, small parameters represent sharper shapes and are particularly good for peaks and steep slopes. The inverse multi-quadric function attains its maximum at the node and decreases monotonically as the distance from the node increases. Next, using the same inverse multi-quadrics (IMQ) for both the u and v displacements yields

$$\begin{aligned} u(\underline{x}) &= \sum_{k=1}^{N} a_{1k} g_k(\underline{x}) + \sum_{j=1}^{M} a_{2j} q_j(\underline{x}) \\ v(\underline{x}) &= \sum_{k=1}^{N} d_{1k} g_k(\underline{x}) + \sum_{j=1}^{M} d_{2j} q_j(\underline{x}) \end{aligned} . \tag{4.26}$$

Further, the polynomials q that correspond to the a and d coefficients can be arbitrarily chosen. Note that details on the Kansa collocation method and the inverse multi-quadrics (IMQ) radial basis functions (RBF) are included in Appendix (B.2). Next, Equation (4.26) on the collocation points with time dependent coefficients can be cast in the form

$$\begin{bmatrix} u(\underline{x}_1,t) \\ v(\underline{x}_1,t) \\ \dots \\ 0 \\ \dots \end{bmatrix} = \begin{bmatrix} g_1(\underline{x}_1) & 0 & \dots & q_1(\underline{x}_1) & 0 & \dots \\ 0 & g_1(\underline{x}_1) & \dots & 0 & q_1(\underline{x}_1) & \dots \\ \dots & \dots & \dots & \dots & \dots & \dots \\ q_1(\underline{x}_1) & q_1(\underline{x}_2) & q_1(\underline{x}_3) & \dots & 0 & 0 \\ \dots & \dots & \dots & \dots & \dots & \dots \end{bmatrix} \begin{bmatrix} a_{11}(t) \\ d_{11}(t) \\ \dots \\ a_{21}(t) \\ d_{21}(t) \\ \dots \end{bmatrix}. \tag{4.27}$$

Equation (4.27) is the scheme upon which the 2-D solution of the integrodifferential equation is constructed. The difference in the displacements of a bond denoted by the vector $\underline{\eta}$ and shown in Equation (4.21), is obtained using Equation (4.26). Specifically, the vector $\underline{\eta}$ with time dependence yields

$$\underline{\eta}(\underline{x},\underline{r},t)=\begin{bmatrix} G_1(\underline{x},\underline{r}) & 0 & G_2(\underline{x},\underline{r}) & \dots & Q_1(\underline{x},\underline{r}) & 0 & \dots \\ 0 & G_1(\underline{x},\underline{r}) & 0 & \dots & 0 & Q_1(\underline{x},\underline{r}) & \dots \end{bmatrix} \begin{bmatrix} a_{11}(t) \\ d_{11}(t) \\ \dots \\ a_{21}(t) \\ d_{21}(t) \\ \dots \end{bmatrix}, \tag{4.28}$$

where

$$\begin{aligned} G_k(\underline{x},\underline{r}) &= g_k(\underline{x}) - g_k(\underline{x}+\underline{r}) \\ Q_j(\underline{x},\underline{r}) &= q_j(\underline{x}) - q_j(\underline{x}+\underline{r}) \end{aligned}. \tag{4.29}$$

4.3.2 Stiffness determination

Having represented the displacements by linear combinations of the basis functions, an approach similar to the one of the finite element method (FEM) is followed. It is assumed that the displacement of any given point inside the domain is captured by interpolating the four adjacent nodes surrounding the point; Figure (4.3) shows this interpolation scheme.

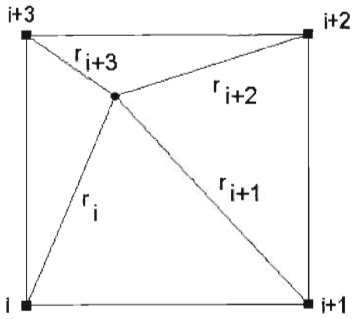

Figure 4.3. A point of interest surrounded by its four closest nodes.

It is clear that for any point that belongs in the square, the four adjacent nodes contribute to its displacement. This leads to a quite convenient and efficient way to integrate over the horizon of each node. Figure (4.4) shows the horizon of each node in a specific element

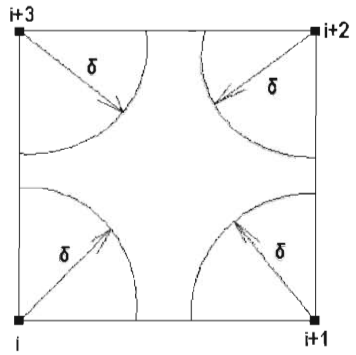

Figure 4.4. The horizon of each node in a square element formed by four grid points

Obviously, the integration of Equation (4.1) can be performed using a finite element approximation inside an element. Specifically, integration over the horizon is required only for one element and its 4 nodes. Then, the integration over the horizon of each node is performed by merely adding the nodal values of the elements, identically as it is done in the finite element method. Therefore,

combining Equations (4.21), (4.24) and (4.28), the peridynamics stiffness density of the node i is given as

$$K=\int_0^{\delta}\int_0^{2\pi}\frac{c}{r}\begin{bmatrix}\cos^2\theta & \cos\theta\sin\theta\\ \cos\theta\sin\theta & \sin^2\theta\end{bmatrix}\begin{bmatrix}G_i(\underline{x}_i) & 0 & \dots & Q_1(\underline{x}_i) & 0 & \dots\\ 0 & G_i(\underline{x}_i) & \dots & 0 & Q_1(\underline{x}_i) & \dots\end{bmatrix}|J|d\theta dr \quad . \tag{4.30}$$

In this regard, combining Equation (4.30) with Equation (4.18) yields the second order micro-modulus tensor

$$C(\underline{\xi})=c\begin{bmatrix}\cos^2\theta & \cos\theta\sin\theta\\ \cos\theta\sin\theta & \sin^2\theta\end{bmatrix}; \tag{4.31}$$

and combining Equations (4.4), (4.19) and (4.20), Equation (4.31) can be cast in a form identical to Silling's in Silling (2000) as

$$C(\underline{\xi})=\frac{c}{\left|\underline{\xi}\right|^2}\underline{\xi}\otimes\underline{\xi}\,. \tag{4.32}$$

Next, the stiffness density matrix corresponding to the g basis functions for a four node element consists of 4x4 blocks of 2x2 matrices and yields

$$K_G=-\int_0^{\delta}\begin{bmatrix}\int_0^{\pi/2}C(\theta,r)\left[G_i(\underline{x}_i,r,\theta) & G_{i+1}(\underline{x}_i,r,\theta) & G_{i+2}(\underline{x}_i,r,\theta) & G_{i+3}(\underline{x}_i,r,\theta)\right]d\theta\\ \int_{\pi/2}^{\pi}C(\theta,r)\left[G_i(\underline{x}_{i+1},r,\theta) & G_{i+1}(\underline{x}_{i+1},r,\theta) & G_{i+2}(\underline{x}_{i+1},r,\theta) & G_{i+3}(\underline{x}_{i+1},r,\theta)\right]d\theta\\ \int_{\pi}^{3\pi/2}C(\theta,r)\left[G_i(\underline{x}_{i+2},r,\theta) & G_{i+1}(\underline{x}_{i+2},r,\theta) & G_{i+2}(\underline{x}_{i+2},r,\theta) & G_{i+3}(\underline{x}_{i+2},r,\theta)\right]d\theta\\ \int_{3\pi/2}^{2\pi}C(\theta,r)\left[G_i(\underline{x}_{i+3},r,\theta) & G_{i+1}(\underline{x}_{i+3},r,\theta) & G_{i+2}(\underline{x}_{i+3},r,\theta) & G_{i+3}(\underline{x}_{i+3},r,\theta)\right]d\theta\end{bmatrix}dr \quad . \tag{4.33}$$

Further, the stiffness density matrix corresponding to the q basis functions for the node i consists of a 2xM matrix, where M is the number of the q functions and yields

$$K_Q = -\int_0^{\delta}\left[\int_0^{2\pi} C(\theta,r)\left[Q_1(\underline{x}_i,r,\theta)d\theta \quad \ldots \quad Q_M(\underline{x}_i,r,\theta)\right]d\theta\right]dr. \qquad (4.34)$$

4.4 Implementation Aspect

4.4.1 Linear differential equations

Utilizing the concept shown in Figures (4.3), (4.4) and combining Equations (4.1), (4.33) and (4.34) yields a set of linear differential equations. Specifically, the set of linear second order differential equations can be cast in the matrix form

$$\begin{bmatrix} \sum_i \rho_i G_i & \sum_j \rho_j Q_j \\ \sum_j Q_j^{\,T} & 0 \end{bmatrix} \begin{bmatrix} \ddot{a}_{11} \\ \ddot{d}_{11} \\ \ldots \\ \ddot{a}_{21} \\ \ddot{d}_{21} \\ \ldots \end{bmatrix} + \begin{bmatrix} \sum_i K_{Gi} & \sum_j K_{Qi} \\ \sum_j Q_j^{\,T} & 0 \end{bmatrix} \begin{bmatrix} a_{11} \\ d_{11} \\ \ldots \\ a_{21} \\ d_{21} \\ \ldots \end{bmatrix} = \begin{bmatrix} b \\ 0 \end{bmatrix}, \qquad (4.35)$$

where $\sum_i \rho_i G_i$ is a square matrix 2Nx2N representing the nodal material density related to the g basis functions, $\sum_j \rho_j Q_j$ is a rectangular matrix 2Nx2M representing the nodal material density related to the additional basis functions q, $\sum_j Q_j^{\,T}$ is a rectangular matrix 2Mx2N and is called the regularization condition,

and finally 0 is the zero matrix 2Mx2M. More details on the regularization conditions can be found in Kansa (1990) and in (B.2). Equivalently $\sum_i K_{Gi}$ is the stiffness density related to the g basis functions which is a square matrix 2Nx2N, $\sum_j K_{Qi}$ is the stiffness density matrix 2Nx2M related to the q basis functions, and $\begin{bmatrix} b \\ 0 \end{bmatrix}$ is the 2Nx1 loading vector on top of a 2Mx1 zero vector representing the regularization conditions. Further, Equation (4.35) is a 2(N+M)x2(N+M) system of second order linear differential equations and can be readily integrated in time using a time integration scheme. Note that since the quantities at Equations (4.30), (4.33) and (4.34) represent stiffness density, this collocation approach is different from the finite element method.

4.4.2 Crack-inclusion treatment

Next, proceed to address the crack growth or crack initiation problem utilizing the preceding peridynamics theory. In this regard, assume that a crack exists in a specific position of the medium. With the above formulation this crack will affect only the peridynamics stiffness of the surrounding nodes. Naturally, the cracks interrupt the horizon of the nodes surrounding them; Figure (4.5) shows how the horizon of the node i+1 is affected.

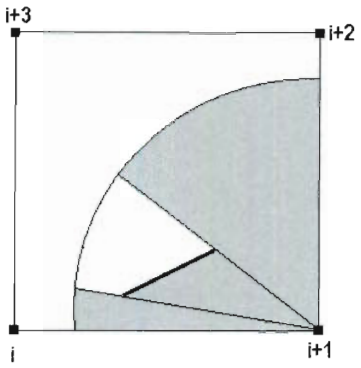

Figure 4.5. The disrupted horizon of node i+1, as it is modeled in peridynamics.

It is perhaps easy to appreciate from Figure (4.5) how effective the peridynamics formulation becomes when dealing with discontinuities in the domain. The crack, in essence describes the bond failure at these points, and therefore the node i+1 along with the other nodes cannot 'see' past the crack, and induces less stiffness density. This feature is implemented by using the same equations as before, only with different integration limits in Equations (4.33) and (4.34). The integration over the discontinuous horizon posses certain difficulties and it is carried out numerically; see Appendix (B.1). Gaussian quadrature is used for the element K_G referring to the 'healthy' part of the domain and is shown in Appendix (A.1). Despite the fact that a more laborious numerical integration is needed for the cracked element, the peridynamics modeling through this approach is quite efficient since a uniform grid of points would have only one kind of elements and thus no other integration is needed. For the integration over the horizon of the functions Q, closed form solutions are available for 'healthy' bonds around the nodes, but for discontinuities numerical integration is again needed and is shown in (B.1).

Furthermore, pointing out that the collocation approach yields stiffness density in contrast to the finite element formulation which yields stiffness, note that the weak form of the problem is given in Emmrich and Weckner (2007), and yields

$$\int_R \rho(\underline{x})\partial_t^2 \begin{pmatrix} u(\underline{x}) \\ v(\underline{x}) \end{pmatrix} w(\underline{x}) dV_{\underline{x}} + \frac{1}{2}\int_R \int_{H(\underline{x})} \begin{pmatrix} u(\hat{\underline{x}}) \\ v(\hat{\underline{x}}) \end{pmatrix} C(\underline{x}, \hat{\underline{x}}) w(\underline{x}) dV_{\underline{x}} dV_{\hat{\underline{x}}} = \int_R \begin{pmatrix} b_x(\underline{x},t) \\ b_y(\underline{x},t) \end{pmatrix} w(\underline{x}) dV_{\underline{x}}, \tag{4.36}$$

where w denotes the weight function. Substituting the displacement function in Equation (4.36) yields the Galerkin approximation which leads to the finite element formulation (FEM). As it is clear for the stiffness expression, a double integration is involved, one on the domain R and one in the horizon domain H. This points out that in the formulation of Equation (4.33) and (4.34), the stiffness density at a collocation point is calculated. Therefore, equation (1) is solved not in terms of displacements and nodal forces as it is from Equation (4.36), but rather in terms of loading density at the collocation points and displacements. Utilizing this formulation, the peridynamics boundary conditions are applied in a much simpler way since the input loading is actually a load density. Further, two consecutive integrations over the discontinuous domains R and H are quite laborious. This is in fact the reason why in the finite element formulation the large number of bonds are replaced by an equivalently large number of truss elements in Macek and Silling (2007). The herein proposed formulation is quite similar to the truss approach, and each node is virtually connected to all the trusses inside its horizon and its stiffness is obtained by direct integration without the actual introduction of the trusses. Further, since the crack is handled geometrically inside the element,

there is no need of checking all the bonds inside the domain. The displacements inside the domain are derived by interpolation of the nodal displacements. Then, the energy release rate is calculated around the crack, independently from the mesh size. Note that, for a more accurate approximation around the crack tip, enrichment of the q functions according to Fleming et all (1997) is available in addition to the grid refinement.

4.4.3 Peridynamics boundary conditions

Having derived the governing equation as a set of linear second order differential equations in matrix form, proceed to incorporate the boundary conditions. Details on incorporating boundary conditions in peridynamics theory are covered in Silling (2000). However, due to this formulation the implementation of boundary conditions becomes readily available. Specifically, an additional layer of material is added to the external part of the elements located on the boundaries of the domain, and is denoted as R*in Silling (2000). The corresponding displacements of the additional layer are decomposed on the same g and q basis functions, and therefore the displacements of the material R* denoted as u* in Silling (2000) are given from Equation (4.26). Figure (4.6) shows the additional layer of material R* that needs to be added on the boundaries.

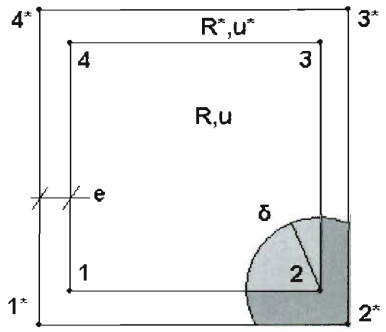

Figure 4.6. The additional layer of material R* needed for implementing the boundary conditions.

Note that the stiffness density related to the lightly shaded area is already available from the preceding equations. However, the stiffness density related to a small layer of thickness e and shown in Figure (4.6) with the darker shade must be added to the stiffness density of the nodes. In this regard, since the displacements u* are decomposed into the same basis as the displacements u, the boundary conditions such as simple supports etc can be applied on the external nodes 1*, 2* etc by utilizing the expansion basis and the displacements of these nodes. Next, to impose certain boundary conditions to the collocation nodes of the Kansa method, specific rows in the matrices shown in Equation (4.35) are modified to account for the imposed constrains. Details can be found in Kansa (1990). Note that the governing equation is solved in terms of the displacement u(x), v(x), and force density b(x). Since the force loading conditions by definition are forcing densities, the boundary conditions are imposed readily using the basis functions. For comparison with any closed form solution models involving stress applied on the above described example, the loading density b(x) must be multiplied by the layer thickness e to yield force per unit area.

4.5 Bond Based Formulation for Arbitrary Poisson Ratio Materials

4.5.1 Enhanced micro-modulus tensor

In Silling (2000) is has been established that the bond-based method yields a model with Poisson ratio of ¼ if the tensor in Equation (4.32) is used. Further, in the above formulation the bond forcing function is constant with respect to the orientation of the bonds. Thus, in this section the manipulation of the tensor of Equation (4.32) is considered in a manner that allows for the modeling of arbitrary Poisson ratio values. This is done by the addition of another micro-modulus function which is dependent on the orientation of the bonds. Consider the enriched linearized micro-modulus function based on Equation (4.32) of the following form

$$C(\underline{\xi}) = \left(c + c_1 \left(\cos\theta \sin\theta\right)^2\right) \frac{\underline{\xi} \otimes \underline{\xi}}{\left|\underline{\xi}\right|^2}, \tag{4.37}$$

and assuming independence with respect to the norm of the vector ξ leads to the 2nd order tensor

$$C(\theta, r) = c\left(1 + m\left(\cos\theta \sin\theta\right)^2\right) \begin{bmatrix} \cos^2\theta & \cos\theta\sin\theta \\ \cos\theta\sin\theta & \sin^2\theta \end{bmatrix} \tag{4.38}$$

where the value m is the ratio of the two coefficients

$$m = c_1 / c \tag{4.39}$$

Note that the forcing density is given in force per unit volume squared, and thus the micro-modulus function in Equation (4.37) is given in N/cm^7. Having this two parameter tensor leads naturally to the calibration of these parameters. In the one parameter bond-based method (see Silling and Askari 2005) the only constant of

Equation (4.32) is calibrated by equating the energy of an isotropically extended plate determined via the classical theory and by the peridynamics theory of mechanics. Depending on the dimensions of the problem, the coefficient yields different values (see Emmrich and Weckner 2007). In this case, the model has two parameters that need to be calibrated with respect to the values of the Young's modulus, and the Poisson ratio of classical mechanics. The proposed scheme for identifying the parameters is as follows. First, combining equations (4.33), (4.34), (4.38) and (4.39) yields

$$K_G = c\left(K_G + mK_G^1\right), \tag{4.40 a}$$

and

$$K_Q = c\left(K_Q + mK_Q^1\right), \tag{4.40 b}$$

where the stiffness densities composed from the first and the second part of the micro-modulus function are given as K_G^1, K_G, K_Q^1 and K_Q (see B.1). Second, solving a simple static problem using classical mechanics and equating the nodal displacements with the displacements given by the basis expansion of equation (4.25) and (4.26) yields the set of the expansion coefficients denoted as $\widehat{a_1}$ etc, and for the static case utilizing the following equation

$$\begin{bmatrix} cI & 0 \\ 0 & I \end{bmatrix} \begin{bmatrix} \sum_i K_{Gi} + m\sum_i K_{Gi}^1 & \sum_j K_{Qi} + m\sum_j K_{Qi}^1 \\ \sum_j Q_j{}^T & 0 \end{bmatrix} \begin{bmatrix} \widehat{a_{11}} \\ \widehat{d_{11}} \\ \cdots \\ \widehat{a_{21}} \\ \widehat{d_{21}} \\ \cdots \end{bmatrix} = \begin{bmatrix} \hat{b} \\ 0 \end{bmatrix}, \qquad (4.41)$$

yields

$$\begin{bmatrix} cI & 0 \\ 0 & I \end{bmatrix} \begin{bmatrix} \sum_i K_{Gi} + m\sum_i K_{Gi}^1 & \sum_j K_{Qi} + m\sum_j K_{Qi}^1 \\ \sum_j Q_j{}^T & 0 \end{bmatrix} \begin{bmatrix} \widehat{a_{11}} \\ \widehat{d_{11}} \\ \cdots \\ \widehat{a_{21}} \\ \widehat{d_{21}} \\ \cdots \end{bmatrix} - \begin{bmatrix} \hat{b} \\ 0 \end{bmatrix} = \begin{bmatrix} R_1 \\ \cdots \end{bmatrix}. \qquad (4.42)$$

Note that $\sum_i K_{Gi}$ is the stiffness density shown in Equation (4.33), and is a 2Nx2N square matrix related to the g basis functions; $\sum_j K_{Qi}$ is the stiffness density shown in Equation (4.34), and is a 2Nx2M rectangular matrix related to the q basis functions; and $\begin{bmatrix} \hat{b} \\ 0 \end{bmatrix}$ is the 2Nx1 loading vector that is applied on the static problem modeled via classical mechanics on top of a 2Mx1 zero vector representing the regularization conditions. Equivalently, $m\sum_i K_{Gi}^1$ and

$m\sum_j K_{Qi}^1$ are the stiffness density matrices related to the g and q basis functions constructed by the additional micro-modulus tensor shown in Equation (4.38). Obviously, Equation (4.42) has two parameters c, m which need to be determined is such a manner that the error between the predetermined nodal forcing values $\hat{b}$ and the obtained ones is minimum. Thus, the error vector R is minimized in the Euclidean measure and finally the values c and m are obtained. Note that since the predetermined forcing $\hat{b}$, and the underlying coefficients $\widehat{a_{11}}$, $\widehat{d_{11}}$ etc correspond to a certain pair of values for the Young's modulus E and Poisson ratio ν, the obtained micro-modulus tensor of Equation (4.37) is compatible with this pair of values in the bond based peridynamics theory of mechanics.

4.5.2 Calibrating the model using a 2-dimensional square plate

A simple example is used next to obtain the coefficients of the above proposed model and demonstrate the effectiveness of the method. A plate under tensile stress is considered and is modeled by the FEM and the peridynamics formulation; the plate is of dimensions 1cm x 1cm and its Young's modulus is $E=1N/cm^2$. The tension is of unitary amplitude $\sigma=1N/cm^2$, and the displacement obtained by the FEM model must match the ones obtained via the peridynamics theory. Figure (4.7) shows the equivalent modeling of the simple problem via the FEM and the peridynamics theory utilizing the Kansa collocation method.

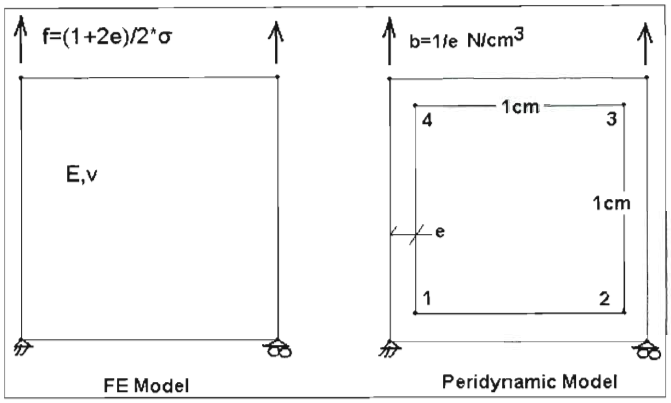

Figure 4.7. A simple 2D plate of unit thickness under tension of $\sigma=1 N/cm^2$, modeled via FEM and peridynamics using the Kansa collocation method.

The displacements given by the FE model are equated to the displacements given by the Kansa collocation method utilizing equation (4.27), and the expansion coefficients are obtained. Then, Equation (4.43) is solved multiple times for different ratio values m, for the actual nodal force densities and for an arbitrary c value

$$\begin{bmatrix} \sum_i K_{Gi} + m\sum_i K^1_{Gi} & \sum_j K_{Qi} + m\sum_j K^1_{Qi} \\ \sum_j Q_j{}^T & 0 \end{bmatrix} \begin{bmatrix} \widehat{a_{11}} \\ \widehat{d_{11}} \\ \cdots \\ \widehat{a_{21}} \\ \widehat{d_{21}} \\ \cdots \end{bmatrix} = \frac{1}{c}\begin{bmatrix} \hat{b} \\ 0 \end{bmatrix}. \qquad (4.43)$$

Once the non linear relation of the ratio parameter m and the displacements has been established, the ratio value m can be obtained for a given Poisson ratio v. Then, since the ratio is fixed, the value c is calculated so that the displacements match the displacements given by the FEM model.

4.5.3 Numerical example

For the example shown above in Figure (4.7) the displacements of the four nodes of the FEM method where obtained for a plate of $E=1N/cm^2$ and various Poisson ratios from 0.25 to 0.5. It is obvious from the way the forcing function is constructed that the c coefficient depends linearly on the Young's modulus E and that the Poisson ratio depends non-linearly on the ratio m. The parameters of the peridynamics model are readily obtained after an example is solved for a specific value of c, and various values of the ratio m. The figure below shows the non linear relationship of the Poisson ratio versus the ratio value m. Note that the value of the Poisson ratio for m=0 is in agreement with the value of the Cauchy crystal Poisson ratio $\nu=1/4$.

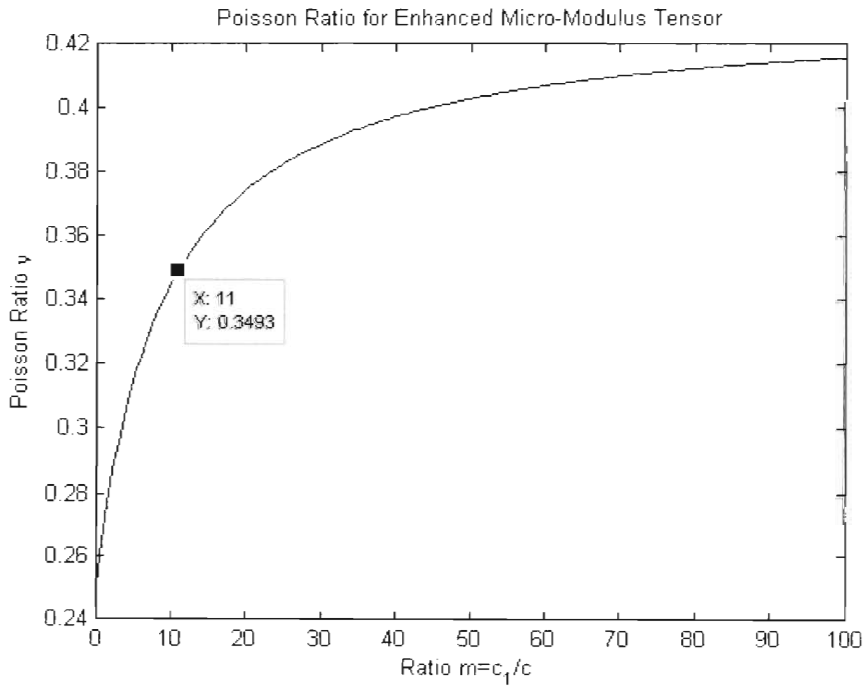

Figure 4.8. Poisson ratio versus the ratio value m for a 2D plate of unit thickness under tension of $\sigma=1N/cm^2$, modeled via peridynamics by the Kansa collocation method.

Figure (4.9) shows the vertical displacement of the peridynamics model of the plate with respect to the coefficient c

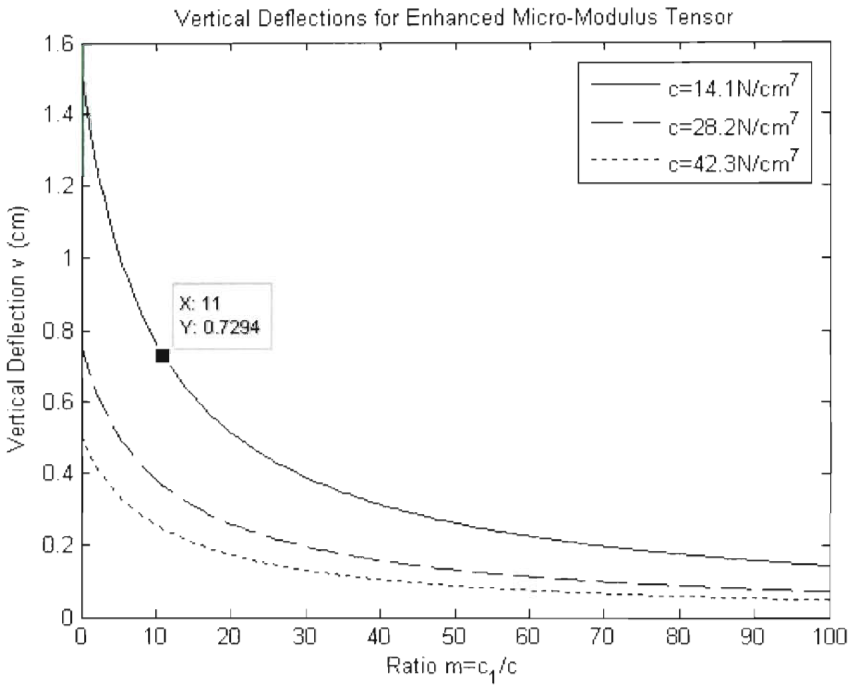

Figure 4.9. Vertical deflection versus the ratio value m for a 2D plate of unit thickness under tension of σ=1N/cm^2, modeled via peridynamics by the Kansa collocation method.

Figure (4.10) shows the surface of the micro-modulus tensor of equation (4.37) on Cartesian coordinates for specific values of the two parameters

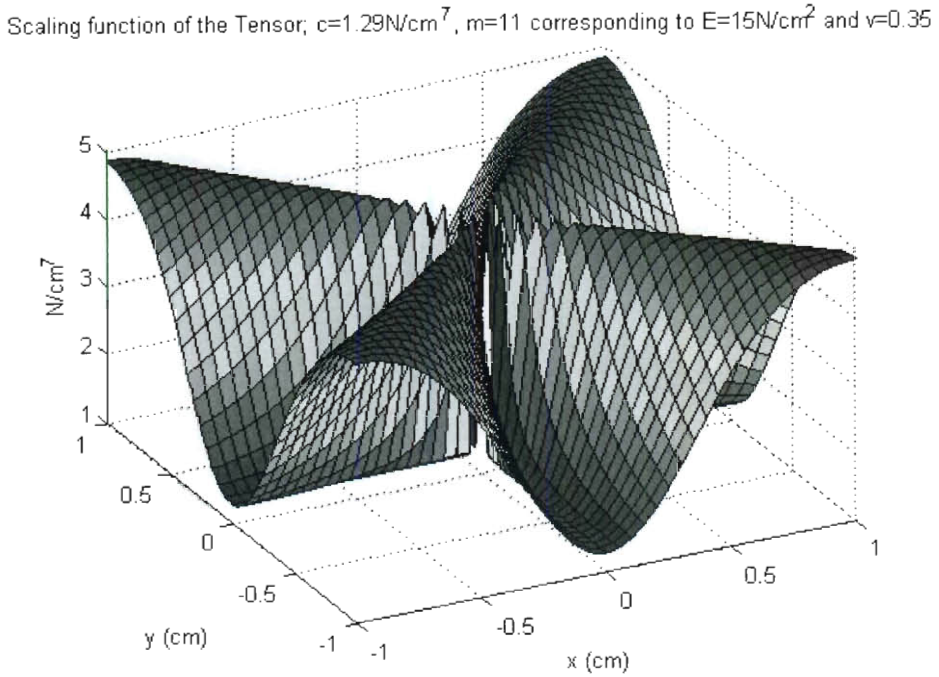

Figure 4.10. The scaling function of the micro-modulus tensor shown in equation (4.37) for specific values of the two parameters c, c_1 corresponding to E=15N/cm^2 and v=0.35 in classical mechanics.

Note that a simple one parameter micro-modulus function would be a cylinder in space.

It is seen that the parameter c determines the modulus E of the peridynamics formulation and thus the deflections on the direction of the stresses. The ratio m determines the Poisson ratio of the peridynamics model. Therefore, for a specific material of given E and v, the fitted parameters of the peridynamics model do not require the solution of a minimization problem. A simple linear example of a plate under uniform tension can be used and the deflections of the model can be plotted against the ratio values m for an arbitrary value c. Then, for the specific Poisson ratio value v the ratio m is obtained. Finally, the deflection of the peridynamics model is equated to the deflection of the classical mechanics model and the

coefficient c is obtained. Conceivably, simple plots such as Figures (4.8) and (4.9) can be used to obtain the coefficients of the peridynamics model for arbitrary values of E and ν. To illustrate the proposed method, consider a 2 dimensional plate of unit thickness, Young's modulus E=15 N/cm^2 and Poisson ratio ν=0.35. Then for a simple tension σ=1N/cm^2 the displacement in the direction of the loading is v=1/15 cm. From Figure (4.8) the ratio m=11 for ν=0.35, and from Figure (4.9) v=0.73cm. Therefore, for a compatible bond-based peridynamics micro-modulus tensor c=14.1N/cm^7/0.73/15=1.29 N/cm^7 and c_1=11*1.29=14.17 N/cm^7. Figure (4.10) shows how the stiffness of the bonds changes with respect to their orientation.

Chapter 5

Illustrative Examples

5.1 Deterministic Case

To illustrate the applicability of the proposed approach developed in chapter 4, a deterministic problem is considered. In this regard, a square 2-D plate of dimensions 1cm x 1cm and bulk modulus $k=1N/cm^2$ under tensile stress is modeled via FEM and peridynamics theory. The tension is of unit amplitude $\sigma=1N/cm^2$ and the displacements obtained by the peridynamics theory are compared to the FEM displacements. Figure (5.1) shows the equivalent modeling of this simple problem via the FEM and the proposed peridynamics theory involving the Kansa collocation method.

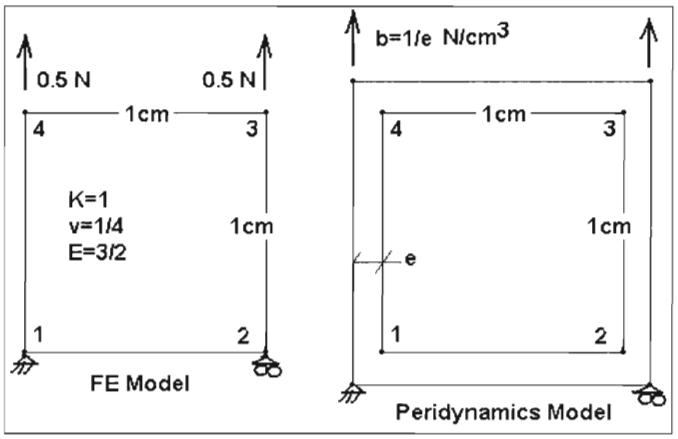

Figure 5.1. A simple 2D plate of unit thickness under tension of $\sigma=1N/cm^2$, modeled via FEM and Peridynamics theory by the Kansa collocation method.

For the FEM, the nodal forces are calculated using the stress applied on that edge. In the peridynamics theory, however, the nodal forces are force densities and $b*e=\sigma$ thus the force density simply depends on the additional layer thickness. The displacements given by the finite element model are compared to the ones

obtained from the proposed formulation in the Table (5.1) below; a layer of thickness e=δ/5 is assumed for the numerical calculations.

Peridynamics via Kansa Collocation Method				
Node	u cm	v cm	ε_x	v
1	-0.027	0.112	-0.160	0.237
2	-0.187	0.112		
3	-0.026	0.787	ε_y	
4	-0.187	0.787	0.674	
FEM Displacements				
Node	u cm	v cm	ε_x	v
1	0	0	-0.167	0.250
2	-0.167	0		
3	0	0.667	ε_y	
4	-0.167	0.667	0.667	

Table 5.1. Comparison of displacements u,v, strains ε_x, ε_y and effective Poisson ratio v for a plate under uniform tension.

As it can be seen in the Table (5.1) the effective Poisson ratio is approximately ¼ as it should theoretically be according to the force-function used in (Silling 2000) and the herein formulation. Next, a cracked element is considered. Figure (5.2) shows a simple patch test used to verify displacements for a cracked square plate under tension.

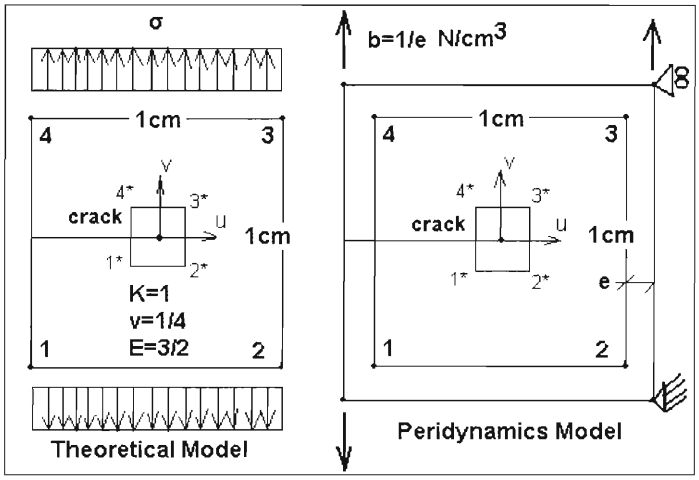

Figure 5.2. A cracked square plate under uniform tension modeled via peridynamics theory and the Kansa collocation method.

The displacements of the analytical solution are given by the closed form equations in Fleming et all (1997) and yield

$$u(\underline{x}) = \frac{k_1}{2\mu}\sqrt{\frac{r}{2\pi}}\cos\left(\frac{\theta}{2}\right)\left[k_2 - 1 + 2\sin\left(\frac{\theta}{2}\right)\right], \tag{5.1a}$$

and

$$v(\underline{x}) = \frac{k_1}{2\mu}\sqrt{\frac{r}{2\pi}}\sin\left(\frac{\theta}{2}\right)\left[k_2 + 1 - 2\cos\left(\frac{\theta}{2}\right)\right]. \tag{5.1b}$$

Taking into account the symmetry of the loading, and transforming the coordinate system, the displacements of the two models are compared for the displacements u and v. The symbol k1 stands for the first mode stress intensity factor, r is the distance from the center of the element, μ stands for the shear modulus, θ is the angle with respect to the initial crack, and k_2 is a parameter depending on the Poisson ratio and the crack geometry. For the element in Figure (5.2) the theoretical displacements are compared to the results of the peridynamics formulation. However, the peridynamics results with this formulation were not accurate. A more accurate approximation of the displacements around the crack tip points is achieved by the enrichment of the basis functions q from Fleming et all (1997) with the basis

$$q_5 = \sqrt{r}\cos\left(\frac{\theta}{2}\right), \tag{5.2a}$$

$$q_6 = \sqrt{r}\sin\left(\frac{\theta}{2}\right), \tag{5.2b}$$

$$q_7 = \sqrt{r}\sin\left(\frac{\theta}{2}\right)\sin\theta, \tag{5.2.c}$$

and

$$q_8 = \sqrt{r}\cos\left(\frac{\theta}{2}\right)\sin\theta\,. \tag{5.2d}$$

The problem of obtaining the displacements around the crack tip was discussed in Fleming et all (1997); the derived results were accurate enough when the basis was expanded with the basis containing the near crack tip displacements. Thus, the linear functions q are enriched by an additional four basis functions for the crack tip. For the simple example shown in Figure (5.2), Table (5.2) summarizes the results for the corners of the square inside the element with side length 0.2cm.

Peridynamics via Kansa Collocation Method		
Node*	u cm	v cm
1	0.128	-0.31
2	0.179	-0.078
3	0.178	0.079
4	0.126	0.31
Theoretical Displacements		
Node*	u cm	v cm
1	0.1354	-0.3269
2	01706	-0.0707
3	0.1706	0.0707
4	0.1354	0.3269

Table 5.2. Comparison of displacements u, v for a cracked plate under uniform tension.

The numerical results obtained prior to the basis enrichment are omitted due to their poor accuracy. However, it is seen that the numerical results, after the basis enrichment are significantly better than the ones obtained without the basis enrichment. Further, there are persistent errors which must be addressed. The

horizon δ that has been used in both examples is δ=1cm and the solution of the first example remains constant for any δ value less than 1cm. The displacements obtained from the cracked domain appear to be dependent on the horizon length for values larger than δ=0.80cm, which is another issue that needs to be addressed. Integration over the horizon for the IMQ basis functions is achieved by implementing the 'visibility' criterion which is extensively described in Fleming et all (1997). That is, the crack interrupts the horizon and thus the values of the g basis functions beyond the crack line are set equal to zero. The same concept holds for all the q basis functions.

5.2 Stochastic Peridynamics Theory

5.2.1 Maximum energy release criterion

The reliability of a structure including a crack or initiating a crack is considered in this section. Specifically, the probability of crack propagation and the direction in which the crack will propagate is of particular interest. For this, the position of the propagating or initiating fracture can be determined by the maximum energy release rate for brittle materials (see E.E. Gdoutos 1990). To obtain the energy release rate, the length of the crack propagation is pre-selected as δα and therefore points to be checked lay on the circular area given by the equation

$$\underline{x}_{test} = \underline{x}_c + \delta\alpha \begin{pmatrix} \cos\phi \\ \sin\phi \end{pmatrix} \tag{5.3}$$

for $\phi \in [0, 2\pi]$, where $\underline{x}_{test}$ is the position of the potential next crack tip and $\underline{x}_c$ is the position of the current crack tip. Since the points on the circle $\underline{x}_{test}$ and the crack tip $\underline{x}_c$ form potential fracture surfaces, the work of all the tensile bonds per unit area of potential fracture can be directly calculated by (see Silling and Askari 2005)

$$G_E = \int_z \int_{V'} w(\underline{\eta}, \underline{\xi}) dV' dz. \tag{5.4}$$

In this equation z denotes the perpendicular distance of a point from the fractured surface and V' is the volume of integration. Figure (5.3) helps to elucidate the concept of the distance z and the volume of integration. For the linearized pair-wise force-function, the work of a single bond yields

$$w(\underline{\eta}, \underline{\xi}) = \frac{1}{2} c s^2 |\underline{\xi}|, \tag{5.5}$$

in conjunction with Equation (4.19) yields the energy per unit surface area of a 2-D plate with unit thickness

$$G_E = \int_0^{\delta} \int_z^{\delta} \int_{-\cos^{-1}(z/r)}^{\cos^{-1}(z/r)} \frac{1}{2} c s^2 r^2 d\hat{\theta} dr dz. \tag{5.6}$$

Further, Figure (5.3) helps visualize the concept of the bonds breaking and forming a cracked surface. Obviously, the energy per unit surface area depends on the initial crack tip, the angle φ, and the length δα, since the stretch s depends on these parameters. From the assumption of linear pair-wise force-function and small rigid body rotations shown in (B.3), the stretch of the bonds can be calculated by a form simpler than Equation (4.12). This form is

$$s(\underline{x},r,\theta)=\frac{1}{r}\begin{bmatrix}\cos\theta & \sin\theta\end{bmatrix}\begin{bmatrix}u(\underline{x})-u(\underline{x}+\underline{r})\\ v(\underline{x})-v(\underline{x}+\underline{r})\end{bmatrix}, \tag{5.7}$$

and Figure (4.2) helps to illustrate this concept. Next, combining Equations (5.7), (5.6), (5.3) and correlating the angles $\widehat{\theta}$, φ and θ through the simple equation

$$\pi/2-\widehat{\theta}+\varphi=\theta \tag{5.8}$$

yields

$$G_E(\delta\alpha,\phi,\underline{x}_c)=\int_0^{\delta}\int_z^{\delta}\int_{\varphi+\sin^{-1}(z/r)}^{\varphi+\pi-\sin^{-1}(z/r)}\left|\underline{\eta}(\theta,\xi,z,\delta\alpha,\phi,\underline{x}_c)\right|^2 d\theta dr dz, \tag{5.9}$$

where $|\underline{\eta}|$ is given for the linearized pair-wise force-function shown in (B.3) as

$$|\underline{\eta}|=s|\underline{\xi}|. \tag{5.10}$$

Naturally, the angle in which the tensile energy per unit area is the maximum can be chosen as the fracture propagation angle; see Gdoutos (1990). Further, in brittle materials the energy release is a measurable quantity and can be used in real applications as a threshold for fracture. Figure (5.3) can be used to clarify this concept; see also Silling and Askari (2005)

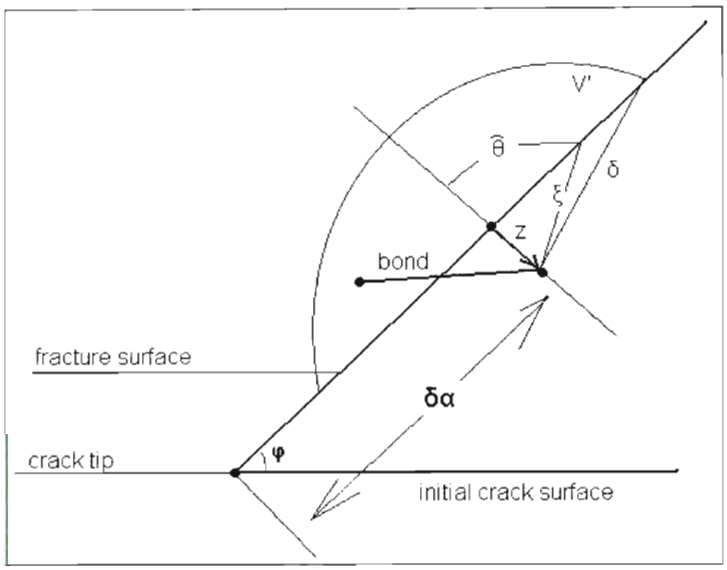

Figure 5.3. The propagating fracture of length δα at angle φ from the initial crack and the calculation of the energy release rate per unit of fractured area.

5.2.2 Stochastic fracture on elastostatic peridynamics theory

Having derived the energy release rate as a function of the crack tip $\underline{x}_c$, propagating crack length δα and propagating crack angle φ, proceed to probabilistically identify the propagation angle. In this context, in classical mechanics, materials with random properties are modeled by expressing the Young's modulus as a random process. However, in the peridynamics approach this must be modified. Obviously, each node is connected to a large number of points belonging in the node's horizon. Thus, the random process which represents the micro-modulus of the bonds must depend both on the angle θ and on the distance r in the polar coordinates system. Herein, the bond micro-modulus is treated as a random process depending only on the distance from the node r. Therefore, the micro-modulus coefficient c is a random process $c(r, \vartheta)$ where ϑ

is the random parameter. Further, the loading of the structure involves uncertainties which are specified in terms of a random variable. The probability density function (PDF) of the energy release rate G_E given in Equation (5.9) must be calculated for the reliability of the crack propagation to be calculated. Naturally the PDF of the coefficients for the static case can be obtained by utilizing Equation (4.35), which yields

$$\begin{bmatrix} a_{11} \\ d_{11} \\ \dots \\ a_{21} \\ d_{21} \\ \dots \end{bmatrix} = \begin{bmatrix} \sum_i K_{Gi} & \sum_j K_{Qi} \\ \sum_j Q_j{}^T & 0 \end{bmatrix}^{-1} \begin{bmatrix} b \\ 0 \end{bmatrix}. \tag{5.11}$$

Obviously, the above equation includes a random matrix inversion and a multiplication by a random forcing vector. In this context, Equation (5.10) combined with Equation (5.7) can be cast in the form

$$|\underline{\eta}| = \sum_{i=1}^{n} \alpha_i \beta_i , \tag{5.12}$$

where $\alpha_i = [a \quad \dots \quad d]$ is the set of the random coefficients, and $\beta_i = [G_1(\underline{x}_{test} + \underline{z}, \underline{r})\cos\theta \quad \dots \quad Q_4(\underline{x}_{test} + \underline{z}, \underline{r})\sin\theta]$ is the set of the deterministic functions which depend on the angle φ and the length δα. Clearly,

$$|\underline{\eta}|^2 = \sum_{i=1}^{n} (\alpha_i \beta_i)^2 + 2\sum_{i=1}^{n-1} \sum_{l}^{n} \alpha_i \alpha_l \beta_i \beta_l \tag{5.13}$$

where l>i. In this case, the probability density function (PDF) of the energy release at a given orientation can be determined by combining Equation (5.13) and (5.9) and yields

$$G_E(\delta\alpha,\phi,x_c)=\int_0^{\delta}\int_z^{\delta}\int_{\varphi+\sin^{-1}(z/r)}^{\varphi+\pi-\sin^{-1}(z/r)}\left[\beta_1(\theta,r,z)^2 \quad \ldots \quad \beta_n(\theta,r,z)^2\right]d\theta dr dz\begin{bmatrix}\alpha_1^2\\ \ldots\\ \alpha_n^2\end{bmatrix}$$

$$+2\int_0^{\delta}\int_z^{\delta}\int_{\varphi+\sin^{-1}(z/r)}^{\varphi+\pi-\sin^{-1}(z/r)}\left[\beta_1\beta_2(\theta,r,z) \quad \ldots \quad \beta_{n-1}\beta_n(\theta,r,z)\right]d\theta dr dz\begin{bmatrix}\alpha_1\alpha_2\\ \ldots\\ \alpha_{n-1}\alpha_n\end{bmatrix}. \tag{5.14}$$

Equation (5.14) involves a summation of products of deterministic coefficients multiplied by random variables and yields the energy release rate for a given probable fracture surface. Having samples of the random variables, leads to the determination of the energy release rate PDF for any direction of propagation and length since the deterministic coefficients depend only on φ, δα and $\underline{x}_c$.

Assuming now that the micro-modulus function is of the form of Equation (4.31), the coefficient c of Equation (4.15) can be taken as a random process such as

$$c(r,\vartheta)=\tilde{c}_0+\hat{c}(r,\vartheta), \tag{5.15}$$

where $\tilde{c}_0$ is the mean value.

The calculation of the stiffness density from Equations (4.33) and (4.34) involves integration over the horizon δ. In this context, the random process can be represented by the Karhunen-Loeve expansion in a manner described extensively in stochastic finite element methods (SFEM) in Ghanem and Spanos (1991). In

this study, the Monte Carlo Simulations (MCS) technique is adopted for the determination of the energy PDF, and thus, the random process shown in Equation (5.15) is sampled for the construction of the stiffness density. Due to the computational demand of the Monte Carlo Simulations (MCS), only the static case with initial fracture inside the domain is addressed in this study. In this context, Equation (5.11), which involves the inversion of a random matrix, is obtained using the inverse Neumann expansion used in SFEM (Ghanem and Spanos 1991). This yields

$$\begin{bmatrix} a_{11} \\ d_{11} \\ \cdots \\ a_{21} \\ d_{21} \\ \cdots \end{bmatrix} = \sum_{j=0}^{Ne} \left[\begin{bmatrix} \sum_i \widetilde{K}_{Gi} & \sum_j \widetilde{K}_{Qi} \\ \sum_j Q_j^{\,T} & 0 \end{bmatrix}^{-1} \begin{bmatrix} \sum_i K_{Gi} & \sum_j K_{Qi} \\ \sum_j Q_j^{\,T} & 0 \end{bmatrix} \right]^j \begin{bmatrix} \sum_i \widetilde{K}_{Gi} & \sum_j \widetilde{K}_{Qi} \\ \sum_j Q_j^{\,T} & 0 \end{bmatrix}^{-1} \begin{bmatrix} b \\ 0 \end{bmatrix}, \quad (5.16)$$

where N_e is the order of the Neumann expansion, $\widetilde{K_G}$, $\widetilde{K_Q}$ is the average stiffness density corresponding to the mean value of the random field, and K_G, K_Q is the stiffness density corresponding to the zero mean random field. Note that a quite large sample of the coefficients must be calculated by pertinent Monte Carlo simulations for the PDF of the energy release rate to be available for all lengths and angles of the crack propagation.

5.2.3 Monte Carlo Application

For the example shown in Figure 10 with initial crack of 2mm in the middle of the domain, $\delta\alpha$=1mm, the PDF of the energy release rate at angles $\varphi=\pi$ and $\varphi=3\pi/4$ is calculated by extensive Monte Carlo simulations of Equations (5.13) and (5.16). Gaussian white noise is used for the random process describing the micro-modulus coefficient c with mean value obtained from equation (4.16) for bulk modulus k=1N/cm^2. The horizon is discretized using 100 points, and thus 100 identical independent Gaussian random variables are considered. The inversion of the random matrix is obtained by a 4th order Neumann expansion and the loading is perturbed by an additional white Gaussian noise with standard deviation 20% of the mean value which is taken to be equal to 1N/cm^2.

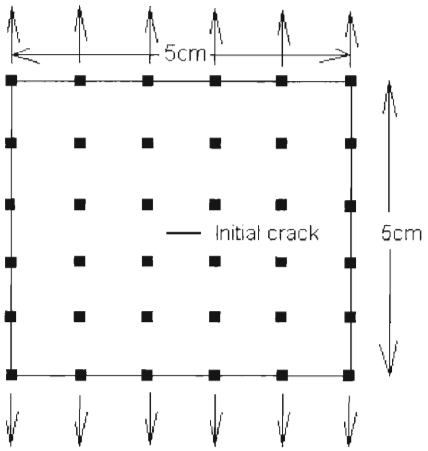

Figure 5.4. A 5cm x 5cm plate under tension including an initial crack in the center.

After a large enough sample of the coefficients is obtained by pertinent Monte Carlo Simulation (MCS) of equation (5.16), the probability density function of fracture in omni directional propagation orientations can be calculated by the deterministic integration of the coefficients of Equation (5.14) for any angle φ,

propagation length $\delta\alpha$ and initial crack tip point $\underline{x}_c$. Figure (5.5) shows one realization of the random micro-modulus coefficient with standard deviation equal to 20% of the mean value shown in equation (5.15). Figure (5.6) summarizes the results for the two approaches. The state of the art mesh-free numerical method is considered in Silling and Askari, (2005). The grid used for the mesh-free numerical method is Δx=0.01cm and thus 10201 nodes are used. The horizon $\delta=5\Delta x$ and the force constant c is sampled from a Gaussian distribution.

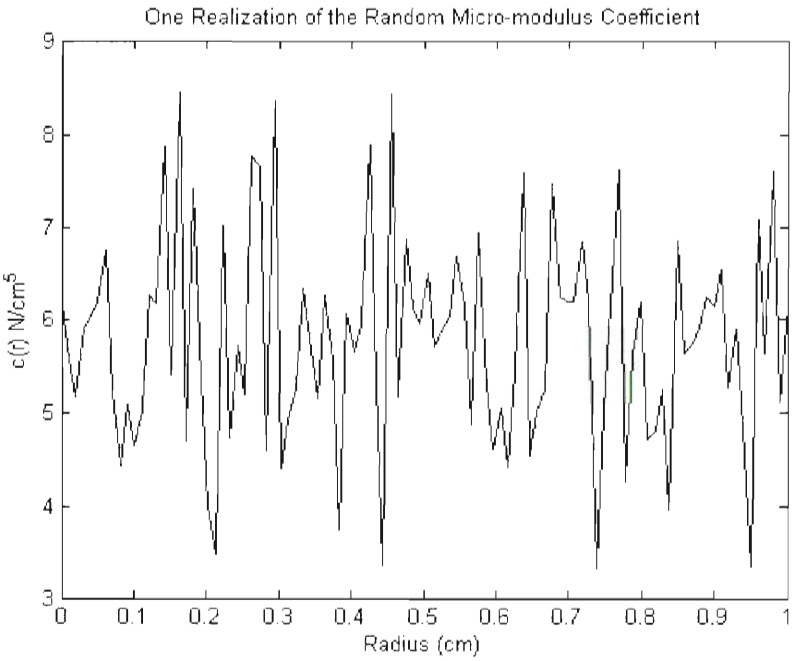

Figure 5.5. Random micro-modulus coefficient spanning the horizon from 0 to δ.

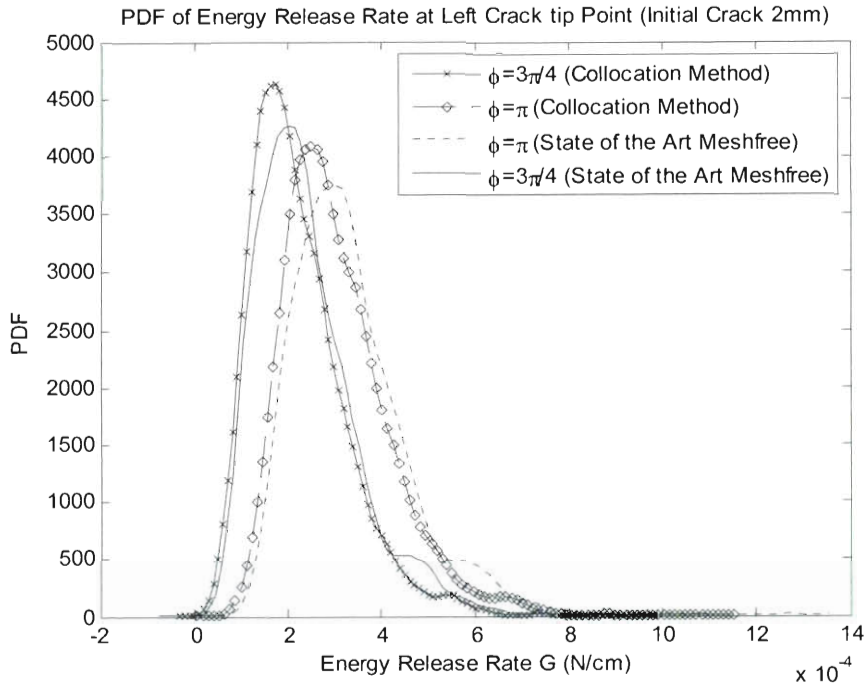

Figure 5.6. The PDF of the energy release rate for the left crack tip point estimated by 6000 Monte Carlo simulations.

The probability density functions obtained from 6000 M.C. simulations using the two methods are in reasonable agreement. However, the difference of the probability density functions shown in Figure (5.6) is attributed to the fact that the methods do not produce identical results around the crack tip. Obviously, a finer grid of nodes will produce more accurate results for the Kansa collocation method. Further, for slightly different cracks inside the element the results deviate from the ones obtained by closed form solutions. A possible resolution of this issue involves the refinement of the grid by adding more nodes on the cracked element. However, in this thesis, the introduction of a novel spatial discretization for deterministic/stochastic peridynamics modeling is the primary concern, and further work is warranted towards the direction of specifically describing the

enrichment efficiency vis a vis the node refinement. In this model, node refinement is not considered due to the nature and simplicity of the numerical example, and due to the fact that the enrichment of the q basis (see Fleming et all 1997) provides quite accurate results for the specific example. However, for more elaborate cracks and medium shapes, node refinement is the most convenient option to achieve accuracy at the expense of additional computation cost.

Chapter 6

Stochastic Meshless Perspective

6.1 Introduction

In many respects, the finite element method (FEM) revolutionized the field of applied mechanics and the manner in which solutions of ordinary and partial differential equations are obtained. The finite element method is used in diverse areas of engineering and applied mathematics and it has evolved into a powerful computational tool that can treat static/dynamic and linear/nonlinear problems. Of course, there are two major challenges in dealing with the FEM. First, the domain of the differential equation must be discretized in smaller parts, and usually the more refined the discretization is the better the solution becomes. Further, in many problems the meshing of the domain is a much more copious step of the method vis a vis the solution steps of the problem. Second, once the domain is discretized and the solution is obtained at the nodes, displacements and derivatives inside the discretized domain are obtained from the shape functions and the nodal displacements. However, at the boundary of two adjacent elements between two nodes some measures can be discontinuous from one element to the other. These two major challenges have been addressed in the formulation of meshless techniques in the pioneering work of Belytschko et all (1994), where the element free Galerkin approach is introduced and the shape functions are spanning the entire domain (see Cyron et all 2010). Specifically, the nodes are distributed inside the domain at the points of interest. This formulation leads to an equivalent stiffness matrix of the degrees of freedom represented by the nodes and

circumvents the laborious meshing of the domain. From then on, an extensive and rich literature can be found in meshless techniques. In Rao and Rahman (2001) the same technique has been applied in fracture and crack propagation and has been correlated with the well established FEM. Due to this formulation the domain can be treated partly as FE and partly as mesh free. In Belytschko et all (2000) the dynamic fracture of concrete has been considered. In Ponthot and Belytschko (1998) the Arbitrary Lagrangian-Eulerean (ALE) formulation was used, and has allowed the nodes to be continuously relocated and thus, providing enhanced performance for crack propagation problems. Besides the Galerkin approach, problems involving differential equations can also be solved by collocation methods. However, before proceeding to the collocation method used herein, the ongoing research of stochastic mesh free methods is briefly reviewed.

As the concept of the FE method was expanded to deal with stochastic material properties and stochastic excitations, the mesh free formulation was expanded to deal with probabilistic mechanics and reliability. In the FE method a spectral approach of the stochastic counterpart has been introduced in the work by (Spanos and Ghanem 1989, Ghanem and Spanos 1990). In this work, the random field was discretized using the Karhunen-Loeve expansion and the random variables that are introduced by this decomposition where projected on the homogeneous polynomial chaos. Other innovative work has been done in this field by (Vanmarcke and Grigoriu 1983, Der Kiureghian and Liu 1986, Deodatis 1991). Further, in the mesh free formulations, the stochastic counterpart has been introduced in Rahman and Rao (2001) for solving linear elastic problems with

stochastic material properties. In (Rao and Rahman 2002, Rahman and Rao 2002) the stochastic mesh free Galerkin based method has been applied in fracture mechanics, and in (Rao and Rahman 2003; Arun et all 2010) the mesh free Galerkin based method has been applied in elastic-plastic cracked structures. Specifically, the statistics of the response in the first two papers have been obtained by the perturbation method. This limits the quality of the solution near the expansion points. In the rest, the first order reliability method (FORM) has been used. In the stochastic mesh free methods the statistics of the response are obtained by inverting a stochastic matrix. This task poses non trivial numerical challenges. Due to this difficulty, in this section the linear elastic problem with stochastic material properties is revisited. Using the Kansa mesh free collocation method, the random field is sampled at the collocation points and yields known random variables at the nodes (see Kansa 1981; Kansa 1990; Xiao et all 2005; Kansa and Hon 2000; Kansa et all 2004, 2009; Sharan et all 1997). This formulation leads to a number of correlated random variables equal to the number of the collocation points. In contrast, the Karhunen-Loeve expansion of the random field would derive a smaller number of uncorrelated random variables independent from the collocation points.

Kansa (1990) in two consecutive papers introduced a quite powerful enhanced multi-quadrics scheme that has been initially developed for spatial approximations. In this context, first a grid of points has been used inside the domain of the differential equation. Second, a set of radial basis functions that can represent any kind of surfaces and bodies in arbitrary dimensions has been used.

These multi-quadric functions are continuously differentiable and integrable, and thus they are quite good for capturing arbitrary order derivatives inside a domain. Further, the Arbitrary Lagrangian-Eulerean (ALE) remapping scheme is available as it is in all the preceding described techniques. Next, the multi-quadrics radial basis functions are used as interpolation functions and the solution is obtained in terms of displacements on the collocation nodes. Note that, the critical concept of this collocation method comes related to another sequence of pioneering publications. Hardy (1975), used the multi-quadric approach to resolve mapping problems in topography, Tarwater (1985) used multi-quadrics as a scattered data interpolation technique and Michelli (1986) investigated the numerical conditioning of the matrices used in these approximations. In his second paper Kansa (1990) solved several parabolic, hyperbolic and elliptic partial differential equations with remarkable accuracy showing how powerful this approach can be. In fact, in Franke and Schaback (1998) the convergence order estimates of the radial basis functions have been rigorously presented.

In the preceding context, for structural problems with stochastic material properties the formulation of an equivalent stochastic stiffness matrix is achieved by the use of the mesh free Kansa collocation method. Further, due to this specific formulation the random matrix can be decomposed as a product of a diagonal random matrix with a full deterministic matrix. Note that the diagonal stochastic matrix is significantly easier to invert than a full matrix. Therefore, the initial system is transformed into an equivalent deterministic system under stochastic

excitation. Utilizing linear algebra and probability theory, the joint probability function of the nodal displacements can be computed.

6.2 Mesh-free Kansa Collocation Method

Linear elastic structures operating under static excitation are considered herein. Proceeding to implement the Kansa mesh free collocation method, a series of nodes is distributed inside the domain forming a grid of points. Next, for simplicity consider the solution of a 1-dimensional differential equation as a function u(x), where x is the position in the 1 dimension space. The method involves approximating the solution function u(x) by a linear combination of radial basis functions f and appropriate auxiliary functions q. Note that the functions q must be compatible with the essential boundary conditions. Next, for a set of $N = L/\Delta x + 1$ equally spaced grid points of distance Δx, the approximation can be cast in the form

$$u(x) = \sum_{k=1}^{N} b_k f_k(x) + \sum_{j=1}^{M} \gamma_j q_j(x). \tag{6.1}$$

In this equation, the multi-quadrics radial basis functions are used, as defined by Kansa (1990)

$$f_k(x) = \sqrt{(x - x_k)^2 + r_k^2}\,, \tag{6.2}$$

where the distance r is a fictitious distance regulating the shape of the basis, M is the number of the additional arbitrary functions, k is the number of the grid point; and b, γ are the unknown expansion coefficients. Large values of the r coefficient contribute to smoother shapes and provide quite accurate approximations of flat

and slowly varying solutions (Kansa 1990). On the contrary, small coefficients represent sharper shapes and are particularly good for peaks and steep slopes (Kansa 1990). Proceeding, the p^{th} order derivative of the displacements can be approximated using Equation (6.1) as

$$\frac{\partial^p u(x)}{\partial x^p} = \sum_{k=1}^{N} b_k \frac{\partial^p f_k(x)}{\partial x^p} + \sum_{j=1}^{M} \gamma_j \frac{\partial^p q_j(x)}{\partial x^p}. \tag{6.3}$$

Equation (6.1) discretized on the grid yields the matrix form equation

$$\begin{bmatrix} u(0) \\ u(\Delta x) \\ \dots \\ 0 \\ 0 \end{bmatrix} = \begin{bmatrix} f_0(0) & \dots & f_N(0) & q_0(0) & \dots \\ f_0(\Delta x) & \dots & f_N(\Delta x) & q_0(\Delta x) & \dots \\ \dots & \dots & \dots & \dots & \dots \\ q_0(0) & q_0(\Delta x) & q_0(2\Delta x) & 0 & 0 \\ \dots & \dots & \dots & 0 & 0 \end{bmatrix} \begin{bmatrix} b_0 \\ \dots \\ b_N \\ \gamma_0 \\ \dots \end{bmatrix}; \tag{6.4}$$

the last M rows represent the regularization equations of the coefficients which state that

$$\sum_{k=1}^{N} q_j(x_k) b_k = 0 \text{ for j=1...M.} \tag{6.5}$$

Next, Equation (6.4) can be cast in the following simpler matrix form

$$\begin{bmatrix} u(x) \\ 0 \end{bmatrix} = \begin{bmatrix} f(x) & q(x) \\ q^T(x) & 0 \end{bmatrix} \begin{bmatrix} b \\ \gamma \end{bmatrix}. \tag{6.6}$$

Thus,

$$\begin{bmatrix} u(x,t) \end{bmatrix} = \begin{bmatrix} f(x) & q(x) \end{bmatrix} \begin{bmatrix} b(t) \\ \gamma(t) \end{bmatrix}. \tag{6.7}$$

The above equation is the basis upon which the solution of the differential equation can be built. Any linear operator L_x applied on the displacements is applied on the expansion functions and is given by the equation

$$\begin{bmatrix} L_x\{u(x)\} \\ 0 \end{bmatrix} = \begin{bmatrix} L_x\{f(x)\} & L_x\{q(x)\} \\ q^T & 0 \end{bmatrix} \begin{bmatrix} b \\ \gamma \end{bmatrix}, \tag{6.8}$$

where the linear operator $L_x\{.\}$ expresses the formulation of the governing differential equation in the space domain.

6.3 Random Field

Since the finite element method is not used, there is no need of integration in the domain, and therefore no immediate need to decompose the random process. Using this collocation method allows imposing the governing differential equation only at the collocation points and then interpolation is used for the solution in between the points. Therefore, instead of choosing nodes to approximate the random field and nodes of the grid to build the solutions on, the same grid points can be used for both. Each fixed node of the grid constitutes a random variable of the random process with fully known probability distribution function. Therefore, the linear operator will operate on the deterministic grid points with correlated random variables of known characteristics. It will be seen that the governing differential equation on the collocation points can be represented as a product of a random diagonal matrix with a full deterministic matrix. Obviously, for non-correlated random variables on the diagonal which correspond to white noise processes, no decomposition of the random field is necessary. However, for correlated random variables on the diagonal the moments are quite copiously obtained, and thus the random process is expanded on the homogenous polynomial chaos. Next, the moments can be readily obtained

through the Neumann expansion (Spanos and Ghanem 1989, Ghanem and Spanos 1990, Ghanem and Spanos 1993). Further, due to this formulation the stochastic matrix remains diagonal and its Neumann expansion is significantly easier to obtain than any other formulation such as (Spanos and Ghanem 1989, Rahman and Rao 1991, Rahman and Rao 2001) where the stochastic matrix is a full NxN matrix where N is the number of nodes.

6.4 Linear Static Response

For the case of static excitation, consider a typical elastic problem in the 2D domain Ω. The associated differential equation with the natural and essential boundary conditions is of the form

$$\nabla\sigma - s = 0 \text{ in } \Omega, \tag{6.9a}$$

$$\sigma \cdot n = \tilde{t} \text{ on } \Gamma_t, \tag{6.9b}$$

and

$$u = \tilde{u} \text{ on } \Gamma_u. \tag{6.9c}$$

In this equation σ is the stress vector, s is the force vector, n in the unit normal to the domain of the partial differential equation, $\tilde{t}, \tilde{u}$ are the traction and displacement field of the natural Γ_t and essential Γ_u boundary conditions, and $\nabla = (\partial/\partial x_1, \partial/\partial x_2)$ is the gradient operator. For this equation to be solved one needs the second set of equations

$$\sigma = D\varepsilon \tag{6.10a}$$

and

$$\varepsilon = \nabla u, \tag{6.10b}$$

where D denotes the material properties matrix and ε the strain vector. Assuming now that the material property matrix D can be represented as the product of a random process multiplied by a proper deterministic matrix, and substituting the set of Equation (6.10) into the set (6.9), yields

$$\nabla\left(D\left(\nabla u\right)\right) - s = 0 \text{ in } \Omega, \tag{6.11a}$$

and

$$u = \tilde{u} \text{ on } \Gamma_u . \tag{6.11b}$$

Note that in the above set of equations the gradient is applied on the random process D. Therefore, with any other formulation, one needs to employ the Karhunen-Loeve expansion of the random process and to differentiate the deterministic eigenfunctions with respect to x. In (Ghanem and Spanos 1990, Spanos and Ghanem 1989) the formulation of the finite elements method in stochastic regime was accomplished by applying the Karhunen-Loeve expansion of the random field. However, due to this collocation method the governing equation is imposed only on the collocation points and the random process denoted as D(θ,x) is sampled at each point yielding one random variable for each collocation point. Obviously, these random variables can be correlated or uncorrelated depending on the random field. Having to solve the stochastic counterpart of the equation

$$D\left(\nabla^2 u\right) - s = 0 \text{ in } \Omega \tag{6.12a}$$

$$u = \tilde{u} \text{ on } \Gamma_u, \tag{6.12b}$$

on the collocation points renders a series of advantages that can be exploited. Since the field of the displacements is approximated by the basis functions spanning the entire domain, the second order gradient of the displacements is applied on the expansion functions. Next, utilizing Equation (6.8) the governing equation can be cast in the form

$$\begin{bmatrix} D\nabla^2 u \\ 0 \end{bmatrix} = \begin{bmatrix} D\nabla^2 f & D\nabla^2 q \\ q^T & 0 \end{bmatrix} \begin{bmatrix} b \\ \gamma \end{bmatrix} = \begin{bmatrix} s \\ 0 \end{bmatrix}, \tag{6.13}$$

where the linear operation operates on the shape functions and the governing equation is now formed in a matrix form. The method handles the boundary conditions by replacing the proper rows of the matrix and the entries of the forcing vector to account for any natural and essential boundary conditions. Next, the random process D(θ,x) representing the random field is applied as a linear operator on the above equation. This, yields

$$\begin{bmatrix} D(x_0)\nabla^2 u(x_0) \\ \cdots \\ D(x_N)\nabla^2 u(x_N) \end{bmatrix} = \begin{bmatrix} D(x_0)\nabla^2 f(x_0) & D(x_0)\nabla^2 q(x_0) \\ \cdots & \cdots \\ D(x_N)\nabla^2 f(x_N) & D(x_N)\nabla^2 q(x_N) \end{bmatrix} \begin{bmatrix} b \\ \gamma \end{bmatrix} = \begin{bmatrix} s(x_0) \\ \cdots \\ s(x_N) \end{bmatrix}, \tag{6.14}$$

where the f and q represent the matrix rows, and the random parameter θ has been omitted for simplicity. Since the random variables are scaling the rows of the matrix, they can be grouped out of the matrix as a diagonal matrix. Therefore, Equation (6.14) becomes

$$\begin{bmatrix} D_m & 0 \\ 0 & I \end{bmatrix} \begin{bmatrix} \nabla^2 f & \nabla^2 q \\ q^T & 0 \end{bmatrix} \begin{bmatrix} b \\ \gamma \end{bmatrix} = \begin{bmatrix} s \\ 0 \end{bmatrix}, \tag{6.15}$$

where

$$D_m = \begin{bmatrix} D(\theta, x_0) & \dots & 0 \\ \dots & \dots & 0 \\ 0 & 0 & D(\theta, x_N) \end{bmatrix} \tag{6.16}$$

and the matrix D_m represents the stochastic diagonal matrix of correlated random variables.

Multiplying both sides of Equation (6.16) by a combination of the inverse of the random matrix and the identity matrix yields

$$\begin{bmatrix} \nabla^2 f & \nabla^2 q \\ q^T & 0 \end{bmatrix} \begin{bmatrix} b \\ \gamma \end{bmatrix} = \begin{bmatrix} D_m^{-1} s \\ 0 \end{bmatrix}. \tag{6.17}$$

Note that, the matrix representing the stiffness is a deterministic matrix, and the random matrix inverse is now applied at the loading. Inverting the deterministic matrix one obtains the coefficients b and γ

$$\begin{bmatrix} b \\ \gamma \end{bmatrix} = \begin{bmatrix} \left[\nabla^2 f\right]^{-1} \left(I - \left[\nabla^2 q\right] C\right) \\ C \end{bmatrix} \left(D_m^{-1} s\right), \tag{6.18a}$$

where

$$C = \left(\left[q^T\right]\left[\nabla^2 f\right]^{-1}\right)\left(\left[q^T\right]\left[\nabla^2 f\right]^{-1}\left[\nabla^2 q\right]\right)^{-1}. \tag{6.18b}$$

The gradients and the symbols f and q denote matrices built by the values that the gradients of the functions f and q attain on the collocation points. The above equation represents a well established problem, of a deterministic linear system under stochastic excitation and it is solved by carrying out the associated calculations. Unlike other meshless approaches and the finite elements method, the coefficients do not represent nodal displacements but rather coefficients of the

basis functions. Therefore, the displacements are obtained using Equation (6.18) in conjunction with Equation (6.7). In this context, the response of a system with random properties is transformed into another equivalent system with deterministic properties under random excitation. However, the random excitation involves a non linear operation on the random properties of the system, and perhaps a closed formed solution can be obtained. Every random variable that appears in the diagonal of the D_m matrix has fully known probability density function and auto correlation function since it belongs to a fully known random process fixed at a specific point of the grid. Specifically, assume a joint probability distribution function of the random variables appearing in the diagonal of the matrix D_m. Then, the PDF of the vector of random variables is given as

$$Y_{\hat{x}}(\hat{x}), \text{ where } \hat{x} = \begin{bmatrix} D(\theta, x_1) \\ \dots \\ D(\theta, x_N) \end{bmatrix}. \tag{6.19}$$

The random vector of Equation (6.17) denotes the applied load y and yields

$$D_m^{-1} s = \begin{bmatrix} \frac{s_1}{\widehat{x}_1} & \dots & \frac{s_N}{\widehat{x}_N} \end{bmatrix}^T = y. \tag{6.20}$$

Further, the PDF of the random variables $\hat{x}$ is known, and the distribution of the inverse of D_m is sought. The general formula for the determination of the PDF of a vector variable is used (Stark and Woods 2002) as follows

$$\begin{bmatrix} \widehat{x_1} \\ \dots \\ \widehat{x_N} \end{bmatrix} = \begin{bmatrix} \varphi_1(y_1, y_2, \dots, y_N) \\ \dots \\ \varphi_N(y_1, y_2, \dots, y_N) \end{bmatrix}, \tag{6.21}$$

where the set of functions φ_i is

$$\varphi_i = \frac{s_i}{y_i} \tag{6.22}$$

and the joint probability distribution of the vector random variable y is given by the equation

$$Y_y(y) = \sum_{j=1}^{N} Y_{\hat{x}}(\hat{x})^{(j)} \left|J\right|^{(j)}, \tag{6.23}$$

where $(\hat{x})^{(j)} \left|J\right|^{(j)}$ denotes the value of the Jacobian and of the random variables at the poles of equation φ. Clearly, the Jacobian yields

$$\left|J\right| = \begin{vmatrix} \frac{s_1}{y_1^{\,2}} & 0 & 0 \\ 0 & \dots & 0 \\ 0 & 0 & \frac{s_N}{y_N^{\,2}} \end{vmatrix}, \tag{6.24}$$

and the roots of Equation (6.22) yield

$$y_1 - g(\hat{x_1}) = 0 \text{ where } g = \varphi^{-1}. \tag{6.25}$$

Since the functions g and φ are the reciprocal of each other, there is one pole for every entry of the vector random variable thus Equation (6.23) yields

$$Y_y(y) = \left|J\right| Y_{\hat{x}}(\hat{x}). \tag{6.26}$$

Having the joint probability function of the vector random variable acting as loads, Equation (6.17) is used to obtain the joint probability function of the displacement. Next, the same procedure is followed for the vector random variables y and the displacements are obtained by the equation

$$\begin{bmatrix} u(x_0) \\ \cdots \\ u(x_N) \end{bmatrix} = [A][y], \tag{6.27}$$

where the matrix A is of dimensions NxN and is obtained by

$$[A] = [f \quad q] \begin{bmatrix} [L(f)]^{-1}\left(I - [L(q)]L_C\right) \\ L_C \end{bmatrix}, \tag{6.28a}$$

with

$$L_C = \left(\left[q^T\right][L(f)]^{-1}\right)\left(\left[q^T\right][L(f)]^{-1}[L(q)]\right)^{-1} \tag{6.28b}$$

and L{.} is the linear operator. The matrix A can be thought of as a flexibility matrix which is calculated once. Having the displacements in terms of the loading yields

$$\begin{bmatrix} u(x_0) \\ \cdots \\ u(x_N) \end{bmatrix} = \begin{bmatrix} \tilde{g}_0(y_1, y_2, y_3, \ldots y_N) \\ \cdots \\ \tilde{g}_N(y_1, y_2, y_3, \ldots y_N) \end{bmatrix}, \tag{6.29}$$

where the $\tilde{g}$ functions are the inner products of the rows of the matrix A with the vector random variable representing the loading y. Thus,

$$\tilde{g}_i(y_1, y_2, y_3, \ldots, y_N) = \sum_{j=1}^{N} A_{ij} y_j. \tag{6.30}$$

Since the matrix A is invertible, the columns of the matrix are linearly independent. Thus, the random variables will be functionally independent (Stark and Woods 2002) which guarantees only one pole for the functions $\tilde{g}$. Therefore, the joint probability density function of the response is obtained as

$$Y_u(u) = |J| Y_y(y), \tag{6.31}$$

where the Jacobian in this case is obtained by the equation

$$J = \begin{vmatrix} \frac{\partial \tilde{g}_1^{-1}}{\partial u_1} & .. & \frac{\partial \tilde{g}_1^{-1}}{\partial u_N} \\ .. & .. & .. \\ \frac{\partial \tilde{g}_N^{-1}}{\partial u_1} & .. & \frac{\partial \tilde{g}_N^{-1}}{\partial u_N} \end{vmatrix}. \tag{6.32}$$

Obviously, any order of moments can be obtained by integration of the joint probability function. However, it is clear that the calculations involve a mathematically intractable closed form solution. Therefore, the joint probability function is handled numerically. In this context, for the numerical evaluation of the statistics of the response there is no need for the calculation of the above joint probability functions. Having the PDF of the random variables, the statistics of the response u can be readily evaluated utilizing the joint probability function of the random variables at the nodes. In this regard, the mean displacement value of the i^{th} degree of freedom of the system yields

$$E\{u_i\} = E\{\tilde{g}_i(\underset{\sim}{\underset{x_1}{s_1}}, \underset{\sim}{\underset{x_2}{s_2}}, ..., \underset{\sim}{\underset{x_N}{s_N}})\}, \tag{6.33}$$

where the $\tilde{g}$ function is given in Equation (6.30) and E{.} denotes the operation of expectation. Therefore, combining Equation (6.30) with Equation (6.33) the expectation at the i^{th} collocation point yields

$$E\{u_i\} = \sum_{j=0}^{N} A_{ij} s_j E\{\underset{\sim}{\underset{x_j}{1}}\}, \tag{6.34}$$

where A_{ij} is the element i^{th} row and j^{th} column of the matrix A. Equivalently the variance of the same degree of freedom is obtained by the equations

$$E\{(u_i - \tilde{u_i})(u_i - \tilde{u_i})\} = E\{u_i^2\} - E\{u_i\}^2, \tag{6.35}$$

and

$$E\{u_i^2\} = E\{\tilde{g}_i(\frac{s_1}{\underset{\sim}{x}_1}, \frac{s_2}{\underset{\sim}{x}_2}, ..., \frac{s_N}{\underset{\sim}{x}_N})^2\}. \tag{6.36}$$

Combining Equation (6.36) with Equation (6.30) yields

$$E\{u_i^2\} = E\{\left(\sum_{j=0}^{N} A_{ij} \frac{s_j}{\underset{\sim}{x}_j}\right)^2\}. \tag{6.37}$$

Further developing the square one obtains

$$E\{\left(\sum_{j=0}^{N} A_{ij} \frac{s_j}{\underset{\sim}{x}_j}\right)^2\} = E\{\sum_{j=0}^{N}\left(A_{ij} \frac{s_j}{\underset{\sim}{x}_j}\right)^2 + 2\sum_{j=0}^{N}\sum_{l=0}^{j}\left(A_{ij} \frac{s_j}{\underset{\sim}{x}_j}\right)\left(A_{il} \frac{s_l}{\underset{\sim}{x}_l}\right)\}, \tag{6.38}$$

which is amenable to numerical treatment. Combining Equation (6.38), Equation (6.35) and Equation (6.34) yields the variance of the i^{th} collocation point. Equivalently, higher order moments can be obtained in the same way.

6.5 Polynomial Chaos Approach

Obviously, Equations (6.38) and (6.34) are quite demanding computationally when the random variables are correlated. Specifically, the numerical evaluation of the mean and variance becomes impractical due to the dimensionality curse. The approach followed by (Spanos and Ghanem 1989, Ghanem and Spanos 1993, Ghanem and Spanos 1990) seems to be a viable

technique especially with this formulation of the mesh free method. First, the random process describing the material properties can be expanded onto the homogenous polynomial chaos basis and then the inverse Neumann expansion can approximate the probability distribution of the response. Due to this mesh free approach the stochastic matrices are diagonal and, therefore, the Neumann expansion will consist of only diagonal matrices. For low orders of polynomial chaos expansion and Neumann expansion, the mean and the variance of the response can be readily obtained by estimating the mean and variance of the polynomial chaos functions and tabulating them for future use. In this context, expanding the random process yields

$$D(\theta,x) = \tilde{D}(\theta,x) + \sum_{i=1}^{m} \Psi_i(\theta) d_i(x), \tag{6.39}$$

where $\tilde{D}(\theta,x)$ is the mean value in order for the zero mean random process to be expanded on the polynomial chaos, Ψ_i denotes the Hermite polynomials and d_i the deterministic eigenfunctions. Equation (6.15) now yields

$$\begin{bmatrix} s \\ 0 \end{bmatrix} = \left(\begin{bmatrix} \tilde{D}_m & 0 \\ 0 & I \end{bmatrix} + \sum_{i=1}^{m} \Psi_i(\theta) \begin{bmatrix} d_{i,m} & 0 \\ 0 & I \end{bmatrix} \right) \begin{bmatrix} \nabla^2 f & \nabla^2 q \\ q^T & 0 \end{bmatrix} \begin{bmatrix} b \\ \gamma \end{bmatrix}, \tag{6.40a}$$

where

$$\widetilde{D}_m = \begin{bmatrix} \widetilde{D}(\theta,x_0) & \dots & 0 \\ \dots & \dots & 0 \\ 0 & 0 & \widetilde{D}(\theta,x_N) \end{bmatrix}, \tag{6.40b}$$

and

$$d_{i,m} = \begin{bmatrix} d_i(\theta, x_0) & \dots & 0 \\ \dots & \dots & 0 \\ 0 & 0 & d_i(\theta, x_N) \end{bmatrix}. \tag{6.40c}$$

Next, utilizing the Neumann expansion for the inverse of the stochastic matrix yields

$$\begin{bmatrix} \nabla^2 f & \nabla^2 q \\ q^T & 0 \end{bmatrix} \begin{bmatrix} b \\ \gamma \end{bmatrix} = \sum_{j=0}^{\infty} (-1)^j \left(\sum_{i=1}^{m} \Psi_i(\theta) \begin{bmatrix} \tilde{D}_m & 0 \\ 0 & I \end{bmatrix}^{-1} \begin{bmatrix} d_{i,m} & 0 \\ 0 & I \end{bmatrix} \right)^j \begin{bmatrix} \tilde{D}_m & 0 \\ 0 & I \end{bmatrix}^{-1} \begin{bmatrix} s \\ 0 \end{bmatrix}. \tag{6.41}$$

Since all the stochastic matrices at the right hand side of Equation (6.41) are diagonal, the inverse of the random variable at each collocation point x_l yields

$$\frac{1}{D(\theta, x_l)} = \left(\frac{1}{\tilde{D}(\theta, x_l)} \right) \sum_{j=0}^{\infty} (-1)^j \left(\frac{\sum_{i=1}^{m} \Psi_i(\theta) d_i(x_l)}{\tilde{D}(\theta, x_l)} \right)^j, \tag{6.42}$$

which can be directly used in conjunction with Equation (6.32) to obtain an approximation of the PDF of the response. The 1st and 2nd order moments can be readily obtained utilizing the tabulated expectations of the Hermite polynomials (Spanos and Ghanem 1989; Ghanem and Spanos 1993).

6.6 Euler-Bernoulli Beam Under Distributed Load and Stochastic Material Properties

6.6.1 Preliminary results

In this section the solution of an Euler-Bernoulli beam, of length L, derived by the proposed approach is presented with distributed load and stochastic material properties. First, the differential equation of the beam is given as

$$M(x) = -\overline{E}(\theta, x) I \frac{\partial^2 u(x)}{\partial x^2}, \tag{6.43}$$

and

$$\frac{\partial^2 M(x)}{\partial x^2} = -p(x), \tag{6.44}$$

where M(x) denotes the moment of the beam at the point x, $\overline{E}$ the Young's modulus, I the moment of inertia, and p(x) the distributed load. Next, combining the above equations and samples the random field on the collocation points yields

$$\overline{E}I(\theta, x_j) \left. \frac{\partial^4 u(x)}{\partial x^4} \right|_{x=x_j} = p(x_j) \tag{6.45}$$

where x_j is the position of the node. Equation (6.45) can be cast in vector form

$$\begin{bmatrix} \overline{E}I(\theta, x_0) \left. \frac{\partial^4 u(x)}{\partial x^4} \right|_{x=x_0} \\ \overline{E}I(\theta, x_1) \left. \frac{\partial^4 u(x)}{\partial x^4} \right|_{x=x_1} \\ \cdots \\ \overline{E}I(\theta, x_N) \left. \frac{\partial^4 u(x)}{\partial x^4} \right|_{x=x_N} \end{bmatrix} = \begin{bmatrix} p(x_0) \\ p(x_1) \\ \cdots \\ p(x_N) \end{bmatrix}. \tag{6.46}$$

Further, utilizing Equation (6.15), Equation (6.46) yields

$$\begin{bmatrix} p \\ 0 \end{bmatrix} = \begin{bmatrix} \overline{EI}(\theta, x_0) & 0 & 0 & 0 \\ 0 & \dots & 0 & 0 \\ 0 & 0 & \overline{EI}(\theta, x_N) & 0 \\ 0 & 0 & 0 & \hat{I} \end{bmatrix} \begin{bmatrix} \frac{\partial^4}{\partial x^4} f & \frac{\partial^4}{\partial x^4} q \\ q^T & 0 \end{bmatrix} \begin{bmatrix} b \\ \gamma \end{bmatrix}, \tag{6.47}$$

where $\hat{I}$ denotes the identity matrix of MxM dimensions. The fourth derivative of the Multi Quadrics radial basis functions is obtained from Equation (6.3) as

$$\frac{\partial^4 f_k(x)}{\partial x^4} = \frac{-15(x - x_k)^4}{\left((x - x_k)^2 + r_k^2\right)^{7/2}} + \frac{18(x - x_k)^2}{\left((x - x_k)^2 + r_k^2\right)^{5/2}} - \frac{3}{\left((x - x_k)^2 + r_k^2\right)^{3/2}}. \tag{6.48}$$

For the q functions, sinusoids are assumed compatible with the boundary conditions. Thus, for a clumped beam these functions can be chosen as

$$q_k(x) = \sin(\frac{(k+1)\pi}{L} x). \tag{6.49}$$

Then, the fourth derivative becomes

$$\frac{\partial^4}{\partial x^4} q_k(x) = \left(\frac{(k+1)\pi}{L}\right)^4 \sin(\frac{(k+1)\pi}{L} x). \tag{6.50}$$

In the matrix of Equation (6.14) the boundary conditions must be implemented as defined in (Kansa 1990). Therefore, at the clumped bar the moments at the ends need to be zero, and thus Equation (6.14) uses the second derivative. Obviously from Equation (6.3) the second order derivative yields

$$\frac{\partial^2}{\partial x^2} f_k(x) = \frac{(x - x_k)^2}{\left((x - x_k)^2 + r_k^2\right)^{3/2}} + \frac{1}{\sqrt{(x - x_k)^2 + r_k^2}}, \tag{6.51}$$

and the second order derivative of q yields

$$\frac{\partial^2}{\partial x^2} q_k(x) = \left(\frac{(k+1)\pi}{L} \right)^2 \sin\left(\frac{(k+1)\pi}{L} x \right). \tag{6.52}$$

Utilizing the formulation of the matrix form with the initial conditions embedded yields

$$\begin{bmatrix} u(0) \\ \frac{\partial^2}{\partial x^2} u(0) \\ \frac{\partial^4}{\partial x^4} u(2\Delta x) \\ \dots \end{bmatrix} = \begin{bmatrix} f_0(0) & \dots & q_0(0) & \dots \\ \frac{\partial^2}{\partial x^2} f_0(0) & \dots & \frac{\partial^2}{\partial x^2} q_0(0) & \dots \\ \frac{\partial^4}{\partial x^4} f_0(2\Delta x) & \dots & \frac{\partial^4}{\partial x^4} q_0(2\Delta x) & \dots \\ \dots & \dots & \dots & \dots \end{bmatrix} \begin{bmatrix} b_0 \\ b_1 \\ \dots \\ b_N \\ \gamma_0 \\ \dots \end{bmatrix}. \tag{6.53}$$

It is obvious from the above equation that the first and last 2 nodal displacements have been used to satisfy the boundary conditions, and thus from the specific formulation the displacements of the 2nd and N-1 node can not be computed readily. However, having the coefficients b and γ one can calculate these displacements subsequently. Also note that the forcing vector must change at the first and last two entries to accommodate the boundary conditions; its values at these specific entries must be set equal to zero. The problem now can be cast in the form

$$\begin{bmatrix} s \\ 0 \end{bmatrix} = \begin{bmatrix} D_m & 0 \\ 0 & I \end{bmatrix} \begin{bmatrix} F & Q \\ q^T & 0 \end{bmatrix} \begin{bmatrix} b \\ \gamma \end{bmatrix}, \tag{6.54}$$

where

$$F=\begin{bmatrix} f_0(0) & \cdots & f_N(0) \\ \frac{\partial^2}{\partial x^2} f_0(0) & \cdots & \frac{\partial^2}{\partial x^2} f_N(0) \\ \frac{\partial^4}{\partial x^4} f_0(0) & \cdots & \frac{\partial^4}{\partial x^4} f_N(0) \\ \cdots & \cdots & \cdots \end{bmatrix}, \tag{6.55}$$

$$Q=\begin{bmatrix} q_0(0) & \cdots & q_M(0) \\ \frac{\partial^2}{\partial x^2} q_0(0) & \cdots & \frac{\partial^2}{\partial x^2} q_M(0) \\ \frac{\partial^4}{\partial x^4} q_0(0) & \cdots & \frac{\partial^4}{\partial x^4} q_M(0) \\ \cdots & \cdots & \cdots \end{bmatrix}, \tag{6.56}$$

and

$$q^T=\begin{bmatrix} q_1(x_1) & \cdots & q_1(x_N) \\ \cdots & \cdots & \cdots \\ q_M(x_1) & \cdots & q_M(x_N) \end{bmatrix}, \tag{6.57}$$

with the loading s given in the vector form by

$$s=\begin{bmatrix} 0 & 0 & p(x_2) & \cdots \end{bmatrix}^T. \tag{6.58}$$

6.6.2 Random material properties modeled as Gaussian white noise

An Euler-Bernoulli beam of length L=10 meters with the material property $\bar{E}I$ being a random process constructed by a mean value $\mu=1000\text{N/m}^2$ over the entire length of the beam and an additional white noise of variance σ. The functions q are chosen as

$$q_0(x)=1, \tag{6.59a}$$

$$q_1(x) = x, \tag{6.59b}$$

$$q_2(x) = \sin(\frac{\pi}{L}x), \tag{6.59c}$$

$$q_3(x) = \sin(\frac{2\pi}{L}x), \tag{6.59d}$$

and dx=0.05 meters which leads to N=201 nodes on the beam of which the displacements of the 199 are readily obtained from the above formulation. Next, two cases are considered in this section, first the beam is simply supported at the two ends, and secondly the beam is fixed on a solid wall creating a cantilever; Figure 1 shows the configuration. The loading in both cases is a distributed load of unitary amplitude.

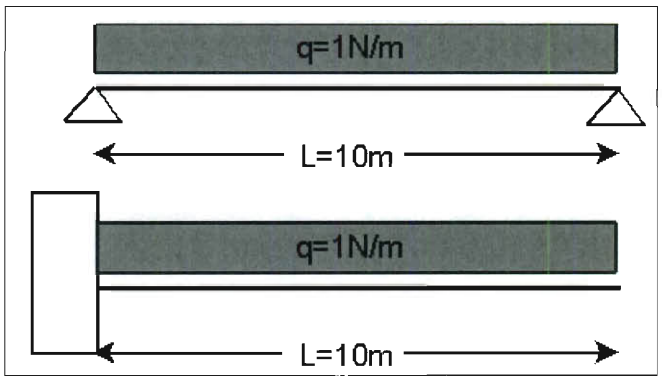

Figure 6.1. A simply supported and a cantilever Euler-Bernoulli beam under distributed loading of unitary amplitude.

Figures (6.2), (6.3), (6.4) and (6.5) show the mean value and the standard deviation at the collocation points for the two cases of Figure (6.1).

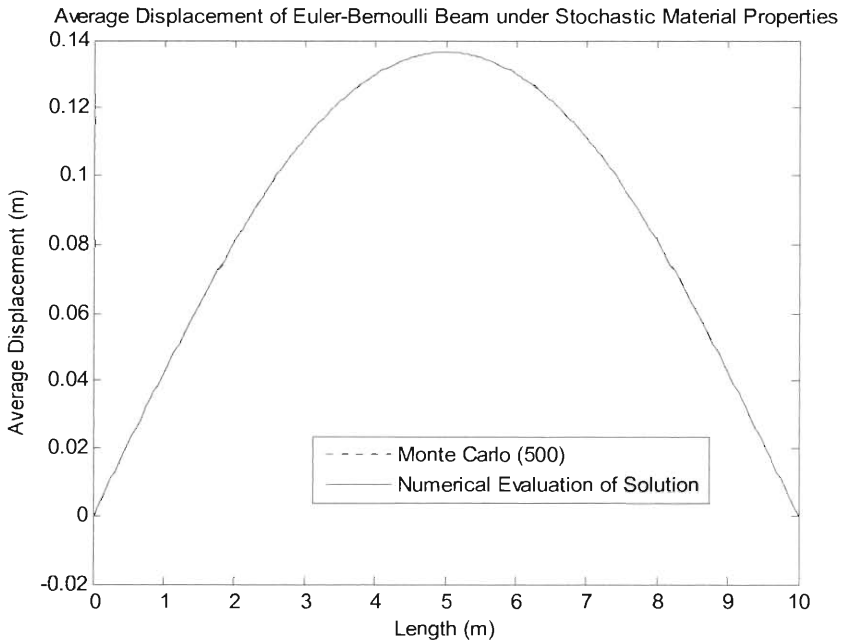

Figure 6.2. Average displacement of the 201 nodes on a simply supported beam under unitary load and random material properties of μ=1000N/m^2 and σ=200N/m^2.

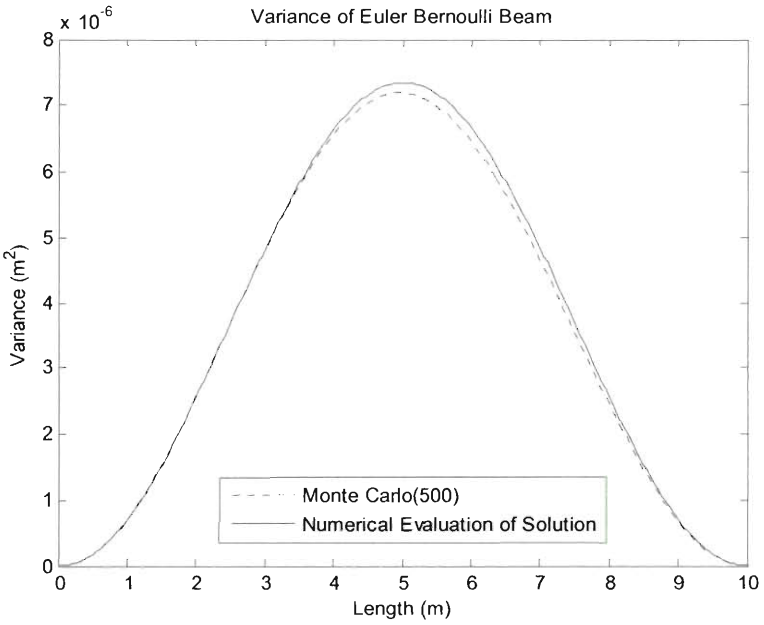

Figure 6.3. Variance of the 201 nodes on a simply supported beam under unitary load and random material properties of μ=1000 N/m^2 and σ=200 N/m^2.

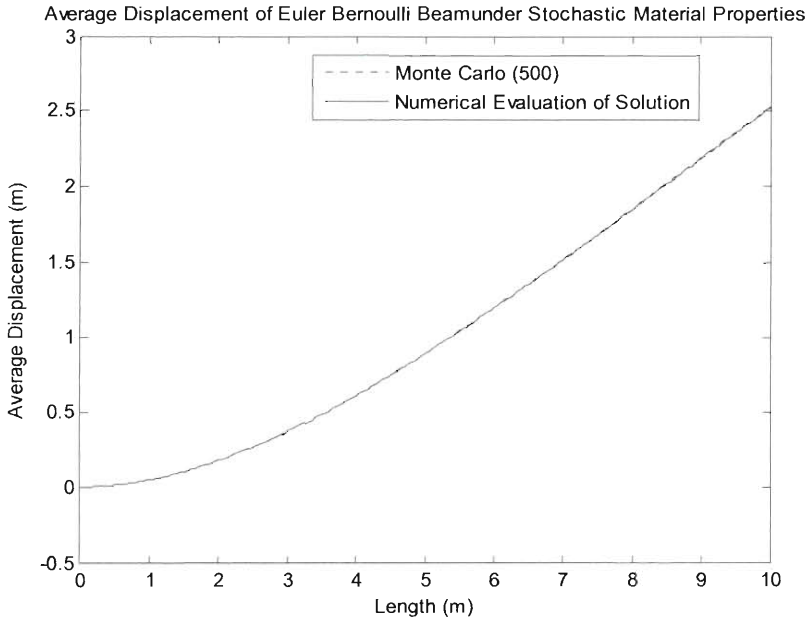

Figure 6.4. Average displacement of the 201 nodes on a cantilever beam under unitary load and random material properties of μ=500 N/m^2 and σ=50 N/m^2.

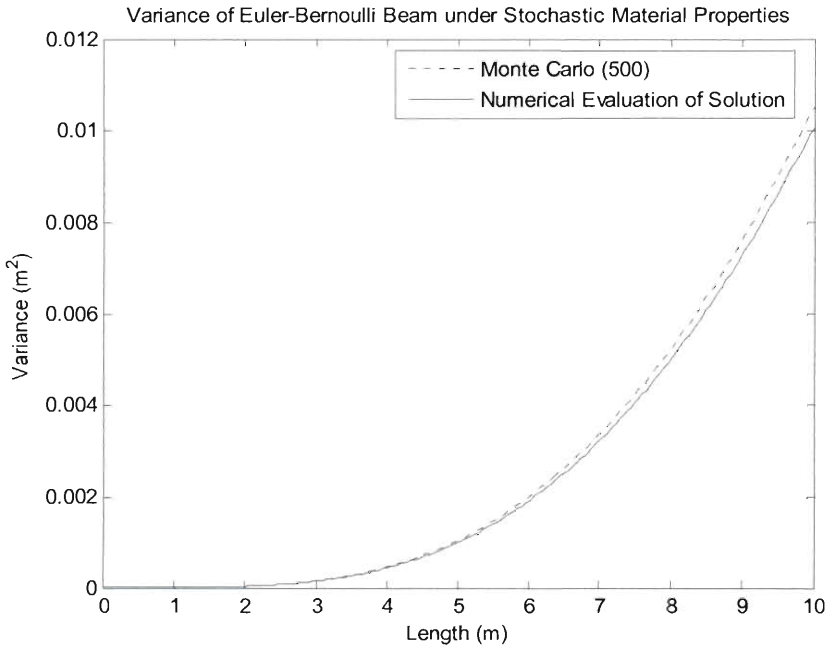

Figure 6.5. Variance of the 201 nodes on a cantilever beam under unitary load and random material properties of μ=500 N/m^2 and σ=50 N/m^2.

6.6.3 Random material properties modeled as non stationary random process made of 4th order polynomial chaos basis functions

For illustration purposes the polynomial chaos expansion of the 4th order is used. The Neumann expansion is truncated at the 3rd order, and therefore the expectations of the polynomials can be calculated fairly easily using a symbolic toolbox such as Mathematica. The expectations $E\left\{\Psi_i(\theta)\Psi_j(\theta)\Psi_k(\theta)\right\}$ are calculated for i,j and k such as $i,j,k=0,...,4$ which have $\binom{5}{3}=10$ possible combinations.

The idea comes from (Ghanem and Spanos 1993) where the expectations of the Hermite polynomials up to the fourth order where tabulated through the MACSYMA symbolic toolbox. Equivalently, the variance $E\left\{\Psi_i(\theta)\Psi_j(\theta)\Psi_k(\theta)\Psi_{i1}(\theta)\Psi_{j1}(\theta)\Psi_{k1}(\theta)\right\}$ which has limited combinations since 5<6 is obtained. The random process is constructed from the polynomial chaos basis in order not to increase the error from the polynomial chaos expansion. Thus, the Hermite polynomials are used with a normalized Gaussian random variable for argument with zero mean and standard deviation one. Next, the space functions of Equation (6.39) are chosen to be

$$d_0(x)=\mu, \tag{6.60a}$$

$$d_1(x)=\sin(\frac{\pi x}{L}), \tag{6.60b}$$

$$d_2(x) = \sin(\frac{2\pi x}{L}), \tag{6.60c}$$

$$d_3(x) = \sin(\frac{3\pi x}{L}), \tag{6.60d}$$

$$d_4(x) = \sin(\frac{4\pi x}{L}), \tag{6.60e}$$

where for this process, the mean value is set to μ and is held constant over the entire domain x. Results are obtained for the tabulated polynomial chaos expectations of the 4th order and 3rd order Neumann expansion. Specifically, first the covariance function of the non stationary random process is shown in Figure (6.9) to describe the random process.

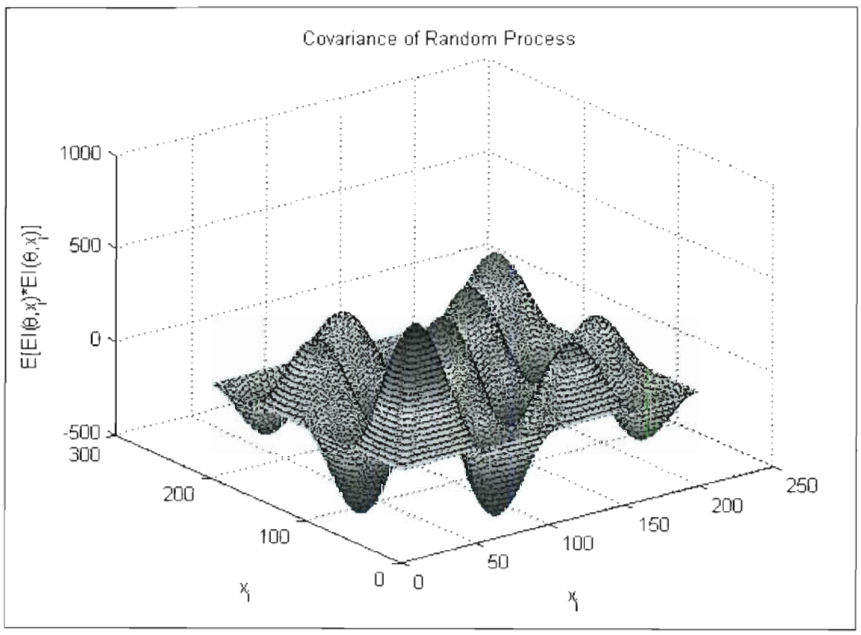

Figure 6.6. Covariance of the artificially built non stationary random process; i,j={1..N,1..N}.

For the non stationary random field described by the covariance shown in Figure (6.6), the results for the mean value and standard deviation of the response for the examples shown in Figure (6.1) are shown in Figures (6.7), (6.8), (6.9) and (6.10).

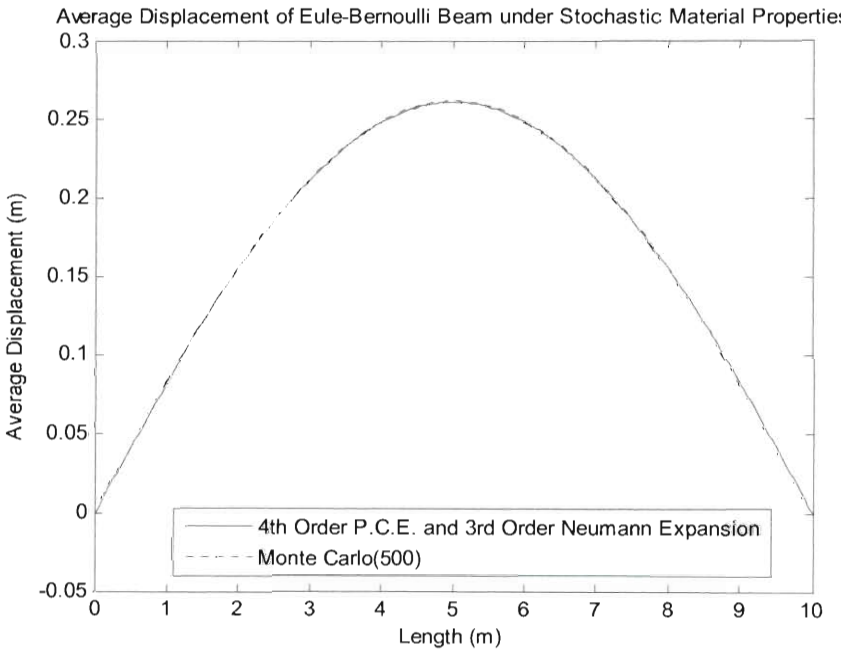

Figure 6.7. Average displacement of the 201 nodes on a simply supported beam under unitary load and random material properties of μ=500 N/m^2 and covariance shown in Figure (6.6).

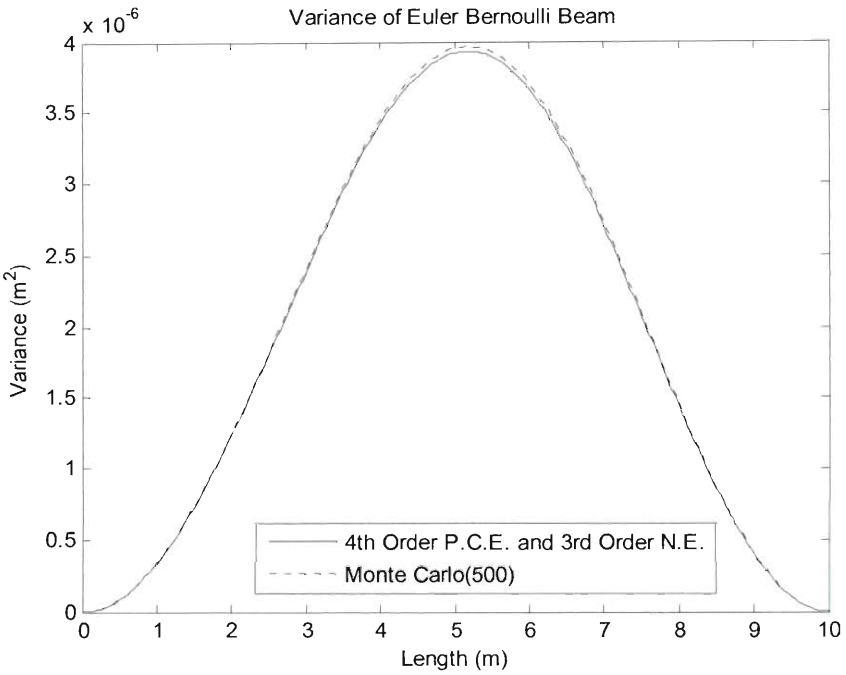

Figure 6.8. Variance of the 201 nodes on a simply supported beam under unitary load and random material properties of μ=500 N/m^2 and covariance shown in Figure (6.6).

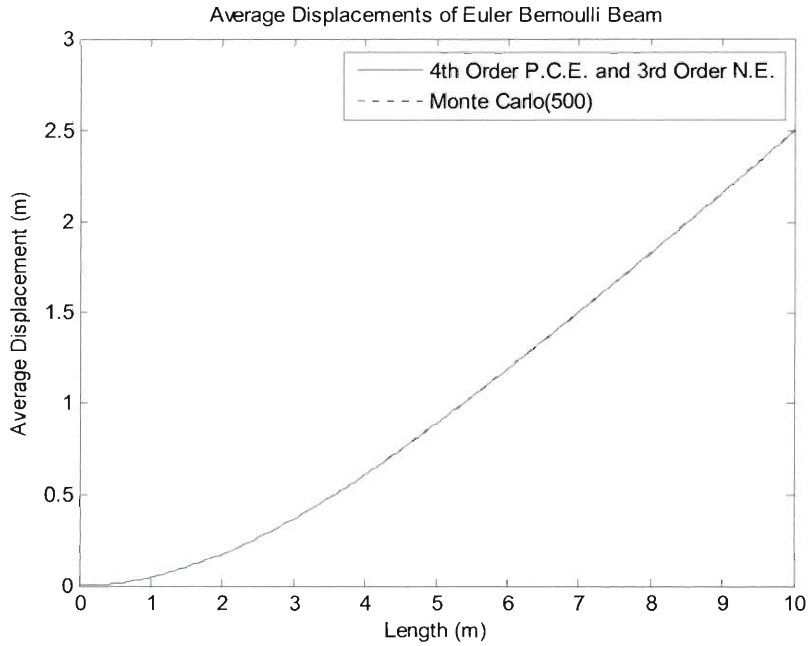

Figure 6.9. Average displacement of the 201 nodes on a cantilever beam under unitary load and random material properties of μ=500 N/m^2 and covariance shown in Figure (6.6).

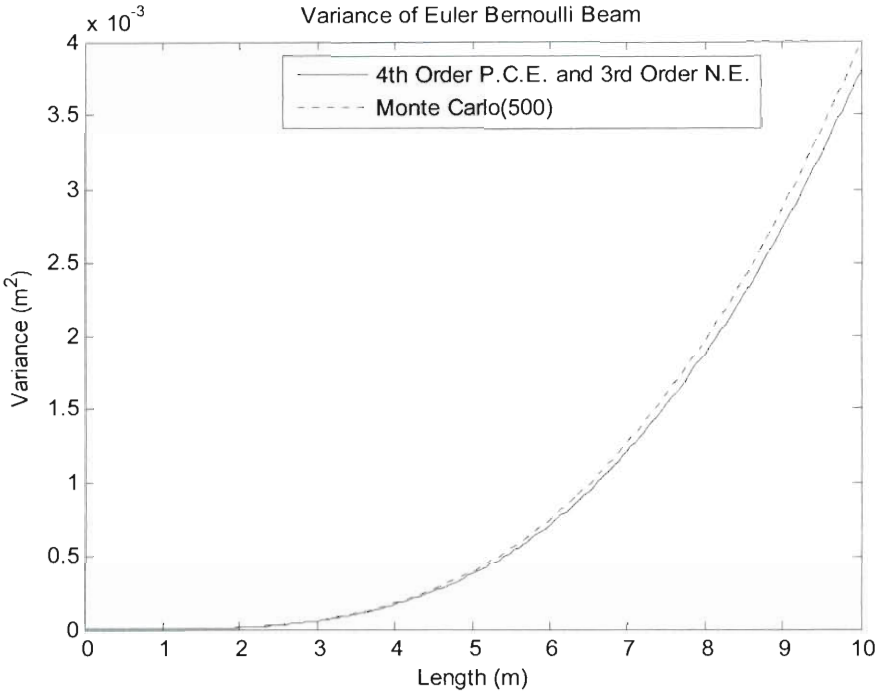

Figure 6.10. Variance of the 201 nodes on a cantilever beam under unitary load and random material properties of μ=500 N/m^2 and covariance shown in Figure (6.6).

Chapter 7

Concluding Remarks

The main conclusions of this thesis are summarized herein. Future directions of expansion of the proposed concepts of each chapter are also discussed.

In chapter 1, the concept of using fractional derivatives to model viscoelastic materials was introduced. Next, the frontier problem of modeling complex materials and specifically polyester ropes operating in service conditions was presented, and the importance of accurately capturing polyester's behavior was noted. Further, the concept of peridynamics modeling of fracture initiation and propagation was discussed and the main disadvantages of this approach were noted. In this context, numerical methods that have been developed to treat partial differential equations and integrodifferential equations arising from the peridynamics theory of mechanics were discussed. Specifically, the mesh-free Galerkin method and the radial basis function (RBF) collocation method were extensively studied. Also, the stochastic extension of the radial basis function (RBF) collocation method was considered for enhanced efficiency in treating stochastic partial differential equations.

In chapter 2, viscoelastic models were introduced to capture the behavior of frequency dependent materials. Specifically the Maxwell, Kelvin-Voigt and Zener models were discussed in addition to their generalized counterparts that involve fractional derivative terms. Next, oscillatory systems were considered,

that incorporate viscoelastic elements governed by fractional derivatives. In this context, the benchmark numerical integration algorithm to integrate the governing fractional differential equation of motion in time was presented (see e.g. Podlubny, 1999) and a Newmark scheme was also presented to treat non linear restoring forces in the system (see Spanos and Evangelatos 2010). Further, an efficient determination of the response of single or multi –degree-of-freedom systems endowed with restoring terms governed by fractional derivatives was pursued. For this purpose the Grunwald-Letnikov representation of the fractional derivative was adopted; this representation involves several past terms of the process itself. Thus, the numerical evaluation of fractional derivatives requires a high number of computations due to their memory effect. A modified Newmark algorithm that includes a correction on the excitation was used to numerically solve the equation. It was shown that a dual meshing technique in the time domain in conjunction with the Taylor expansion and the Grunwald-Letnikov fractional derivative representation yields an efficient extension of the Newmark time integration scheme for the determination of the response of non linear oscillators comprising fractional derivative terms. In this context, the governing equation of motion can be transformed into a second order differential equation using new effective values of mass, damping, and stiffness without any fractional terms involved. The effective values are calculated once by a vector representing the GL coefficients and the connectivity matrix representing the Taylor expansion. Next, this equation was solved for an excitation corrected by the contribution of few past terms. The new scheme has been used to obtain

simulation results for linear systems under seismic excitation which was validated by the solution derived by frequency domain techniques. Further, extensive numerical simulations were employed to provide a numerical proof of convergence of the proposed scheme. Further, the results of the newly proposed scheme were compared vis-à-vis the benchmark algorithm involving the truncated Grunwald-Letnikov representation and provided quite accurate results (see Spanos and Evangelatos 2009; Evangelatos and Spanos 2011). Future work relating to efficient numerical integration of fractional differential equations may utilize Pade approximants instead of Taylor expansion. Further, a rigorous mathematical identification of the error bounds and convergence order may be pursued for a more precise determination of the requisite value of the j parameter. This parameter relates the backward Taylor expansion and influences critically the accuracy of the developed numerical scheme.

In chapter 3, a procedure was devised for utilizing iterative solutions of catenary equations to determine the effective length and modulus of elasticity of polyester mooring ropes in service conditions. For the determination of the modulus of elasticity of polyester the data acquired during the hurricane Katrina on 25^{th}-28^{th} of August 2005 were used. Next, the modulus was decomposed into a 'static' part and a 'dynamic' part, and the recorded data, in conjunction to a mathematical model based on the catenary equations, allowed the determination of the solution of the two nonlinear equations with two unknowns. These unknowns were the initial length of the particular mooring line and the effective modulus of elasticity of the polyester rope under calm 'static' conditions. Further,

the devised mathematical model allowed the determination of an effective modulus of elasticity of the mooring line material under dynamic conditions. For this, the mathematical model was utilized in conjunction with data pertaining to the fairlead tension time histories to derive estimates of the underlying strains of the polyester ropes. Next, the tension and strain time histories were used to fit a non linear viscoelastic model. This model is a non linear extension of a Zener model and has good modeling capabilities due to the arbitrary order of fractional derivatives that incorporates. The non linear extension of the Zener model is of the polynomial kind, and the parameters of the model were obtained by a non linear regression method. The tension results obtained by the non linear viscoelastic model were compared vis a vis the actual tension calculated by utilizing the data and iteratively solving the catenary equations. Next, the proposed model results were found in a good agreement with pertinent experimental data. The fact that the model accurately captures the polyester behavior at the peak of the hurricane, where the maximum tension and displacement was recorded, supports the robustness of this model for further use in the design process of polyester mooring systems. Future work may focus on utilizing other kinds of models such as the Preisach hysteretic model and the Bouc-Wen model. Specifically, the Preisach hysteretic model is perhaps capable of capturing the highly complex hysteretic loops of polyester that are attributed to relaxation, creep, and frequency dependent phenomena.

In chapter 4, the application of the peridynamics modeling on stochastic systems incorporating discontinuities was considered. Proceeding to this task, a

novel approach for the spatial discretization of the integrodifferential equation arising from the peridynamics theory that allows for stochastic extension was devised. This spatial discretization is based on the inverse multi-quadric (IMQ) radial basis functions (RBF) enriched with polynomials from the finite element method. Due to this formulation the stochastic problem can be solved in a manner similar to the one of stochastic finite element method, with some minor differences arising from the peridynamics stiffness density formulation. Following a path similar to the finite element method, the stiffness density of each element surrounded by four nodes was constructed incorporating fracture inside. The discontinuity inside the element was handled by applying the 'visibility' criterion and by changing the integration limits in the polar coordinate system. After formulating the stiffness density of the healthy and cracked elements, the global stiffness density matrix on the collocation points was assembled and the system has become readily solvable (see Spanos and Evangelatos 2010; Evangelatos and Spanos 2011).

Having established an effective spatial discretization of the governing equation, the strong limitation regarding the Poisson ratio of the bond-based peridynamics formulation was addressed. It is theoretically proven that the bond-based peridynamics model with the simple forcing function yields a Cauchy crystal material with locked Poisson ratio of $\nu=1/4$. This limitation has been addressed by introducing an enhancement of the micro-modulus tensor such that, it allows the modeling of arbitrary Poisson ratio values. For this, a simple, symmetric, scaled sinusoidal function is added having an additional parameter c_1.

Thus, it transforms the one parameter bond based micro-modulus into a two parameter model dependent on c and c_1. Further, this function is a positive symmetric function and, therefore, the derived 2^{nd} order tensor remains symmetric. Obviously, the determination of these parameters is based on the values of the Young's modulus E and Poisson ratio ν of the classical mechanics approach. It was shown, that the Young's modulus depends on a linear manner on the c parameter, and that the Poisson ratio depends on a non linear manner on the parameter c_1/c. Therefore, the proposed identification of the model parameters is based on solving a simple linear system for several ratios c_1/c and for a fixed arbitrary coefficient c. Upon identifying the non linear relationship of the Poisson ratio with respect to the ratio c_1/c, the deflection of the peridynamics model is equated to the deflections of the classical mechanics model and the second parameter c can be determined using its linear relationship. In this context, the coefficients are not obtained by the use of energy equations but rather by the use of a linear displacement field. Further, the herein devised micro-modulus tensor leads in a more complex micro-potential function which is intractable for analytic calculations. However, the energy potential of the bonds is not needed for the calibration of the parameters, and any use of this function for the determination of the energy release rate in the case of cracks can be obtained numerically. In this regard, extensive simulations were conducted for purely shear loads on a peridynamics element modeled by this approach, and the results did not capture the theoretical model results accurately. This can be partially attributed to the fact that, shear loading on a square element is a much more complex kind of loading

that applies tension in a diagonal direction, compression in the other diagonal direction, and shear combinations inside the element. Thus, the bond-based peridynamics approach must be extensively refined to accurately capture the deformation. Further, shear deformations implicitly impose rotations of the bonds and the linearized micro-potential tensor used herein is by definition deficient in capturing large rotations.

In chapter 5, having derived an effective approach to circumvent the Poisson ratio limitation of the bond based peridynamic formulation in conjunction to a spatial discretization to treat the underlying integrodifferential equation, a crack inclusion was considered in the material. Since a continuous approximation is available for the displacements inside the domain, the energy release rate was calculated progressively around the crack tip. Therefore, the notion that the crack propagates in such a way that the energy release rate attains its maximum value was adopted. For systems with random material properties under random excitations the PDF of the energy release rate was obtained by Monte Carlo simulations of the requisite Neumann expansion. Further, having the PDF of the energy release for the area around the crack tip determines whether the crack propagates, and in which direction with respect to the initial crack surface. Note that this is the first work correlating the peridynamics formulation with reliability of failure. Specifically, stochastic fracture propagation and stochastic response of systems modeled utilizing the peridynamics formulation was presented and pertinent results demonstrated the effectiveness of the proposed approach (see Evangelatos and Spanos 2010). Further, it is the first work to utilize a micro-

modulus tensor enhancement to circumvent the Poisson ratio restriction arising in bond-based peridynamics formulation. It is pointed out that the alternative formulation (see e.g. Silling et all, 2007) is based on non ordinary peridynamics states, and thus, it is fundamentally different from the bond-based concept.

Future work on this area may focus on applying the proposed tensor enhancement on the non linearized peridynamics micro-modulus tensor for modeling purely shear loading. Further, substituting the spring-kind potential of the bonds by a Lennard-Jones potential yields readily molecular dynamics formulations (see e.g. Kalinichev and Kirkpatrick 2002; Huang et all 2011) and, thus, many possibilities in capturing micro cracks and fracture propagation in the nano-scale arise. Specifically, the application of the peridynamics formulation in concrete fracture may be of considerable research interest. Concrete is a non homogeneous material and its fracture behavior is significantly different than that of fatigued steels and ceramics. Specifically, for concrete, two parameters are required to predict fracture, the energy release rate G_F originating from Griffith's criterion, and the cohesive crack energy release rate G_f (see Bazant and Giraudon 2002; Bazant and Novak 2000). Accurate calculation of the Griffith's energy release rate is feasible by the peridynamics formulation. However, the energy from the cohesive cracks has not been considered thus far. In this regard, future applications may focus on modifications of the current bond based peridynamic formulation to accurately capture non homogeneous materials and concrete, in particular.

In chapter 6, the linear elastic response of structures under deterministic loading with stochastic material properties was considered. For this purpose, the Kansa mesh free collocation method of multi-quadrics (MQ) radial basis functions (RBF) was used to obtain the solution of the governing differential equation. In this context, a set of grid points is distributed inside the domain, and the solution is represented by the radial basis functions (RBF). Next, the stochastic material properties were assumed to constitute a random field spanning the domain of the differential equation, and have been sampled at the nodes as fully known random variables. In this regard, it was shown that the random matrix resulting from this formulation has a clearly described pattern. The jointly distributed random variables are scaling the rows of a deterministic matrix. Thus, the random matrix can be obtained as a product of a random diagonal matrix multiplied by a full deterministic matrix (see Evangelatos and Spanos 2010). Since, a random diagonal matrix can be readily inverted by inverting the elements on the diagonal, the problem yields a deterministic system under stochastic excitation. Having the fully known probability function of the random variables at the diagonal of the random matrix, the probability density function of the inverse can be obtained in a closed form solution. Even though the closed form solutions exist, these solutions for correlated random variables become intractable and even a numerical evaluation can become quite laborious. For this reason, the polynomial chaos expansion was used to decompose each random variable onto the orthogonal space created by the Hermite polynomials. Next, the Neumann series expansion was used to obtain the inverse of the diagonal stochastic matrix.

Thus the probability density function (PDF) of the response can be obtained by Monte Carlo simulations. Due to the diagonal stochastic matrices, the Neumann series expansion yields only diagonal matrices. Therefore, the calculations can be conducted with drastically reduced computational cost. Note that, to the stochastic meshless via the Galerkin approach, and to the stochastic finite elements method (SFEM) the stochastic matrices are full NxN matrices that ultimately must be inverted. Further, for the mean and standard deviation of the response, the expectations of the polynomial chaos functions can be calculated and tabulated once using their known properties. After this is done for a relatively low order of polynomial chaos and Neumann series expansions the mean and variance of any system can be obtained readily using the tabulated 1^{st} and 2^{nd} order moments of the Hermite polynomials (see Ghanem and Spanos 1991, Evangelatos and Spanos 2010). The effectiveness of the herein proposed approach was demonstrated by comparing the obtained results with pertinent Monte Carlo simulations.

The binding element of the developments of this thesis has been the objective of addressing non-locality and randomness features in mechanics problems in a somewhat integrated format. Clearly, the tools of fractional derivatives and peridynamics horizons are viable options which deserve additional attention. In a somewhat similar context, the versatility of the family of radial basis functions should be more addressed as they afford to circumvent the strict locality of traditional finite elements and have global support over the solution space; this comment is applicable both for deterministic and stochastic formulations.

Appendices

Appendix A: Offshore Platform Anchored by Polyester Mooring Lines

A.1: Latin symbols

BS: Breaking strength of polyester rope (4261 Kips)

D_e: Estimated depth from the platform to the anchoring point of the multi-component line

D_r: Actual or 'real' depth from the platform to the anchoring point of the multi-component line

g: Gravitational acceleration

L_0: The zero stress length of all the polyester segments installed in a multi-component line after the initial construction stretch has been released

p_k: Search direction towards the minimum of the Gauss Newton minimization algorithm at the k^{th} step

R: Error vector of the end tip point of the multi-component line in a 2D Cartesian coordinate system aligned with the underlying 2D plane of the multi-component line

r_x: Rotation around the x axis (pitch)

r_y: Rotation around the y axis (roll)

r_z: Rotation around the z axis (yaw)

s: Integration variable for the length of a polyester segment

S_e: Estimated horizontal distance from the platform to the anchoring point of the multi-component line

S_r: Actual or 'real' horizontal distance from the platform to the anchoring point of the multi-component line

T: Tension at a given point of the line

T': Tension at a given point of the line after the water pressure force is subtracted

w: Submerged weight of polyester rope of unitary length

x: Integration variable of the horizontal distance from the platform to the anchoring point of the multi-component line

z: Integration variable of the depth from the platform to the anchoring point of the multi-component line

A.2: Greek symbols

EA: Product of Young modulus with the cross section area of the polyester rope

φ: Angle of the normal vector of the cross section area of the polyester rope with respect to the horizontal line

θ_i: Initial angle of the i^{th} polyester segment

ρ: Water density

τ_x: Translation along the x axis (surge)

τ_y: Translation along the y axis (sway)

τ_z: Translation along the z axis (heave)

A.3: Definitions

Catenary: is the theoretical shape of a hanging chain assuming that it is supported from its two ends while its own weight alone is acting as a force

Connector: Metallic connecting device that connects polyester rope with another rope or a chain

Chain Jacks: Metal wheels in which the chain is wrapped around and locked at the one end

Fairleads: A device to guide a line, rope or cable around an object or stop it from moving laterally

Fairlead centerline: The center of an imaginary circle that has all the fairlead points on its circumference

Hull: is the watertight body of a ship or a vessel

Mooring line: The anchoring line that comprises several polyester ropes, chains and connectors

Northings-Eastings: is the output of a GPS and it is the geographic Cartesian coordinates of a point on the earth

A.4: Fairlead motion translations

The GPS system is placed in an elevated known position on the platform and provides 'Northings' and 'Eastings'. Angular data are also provided by equipment on board (pitch, roll, yaw). Figure (A.1) shows the 3 degrees of freedom corresponding to translations (surge, sway and heave) and 3 degrees of

freedom corresponding to rotations (pitch, roll and yaw) and their orientation in a global axis system

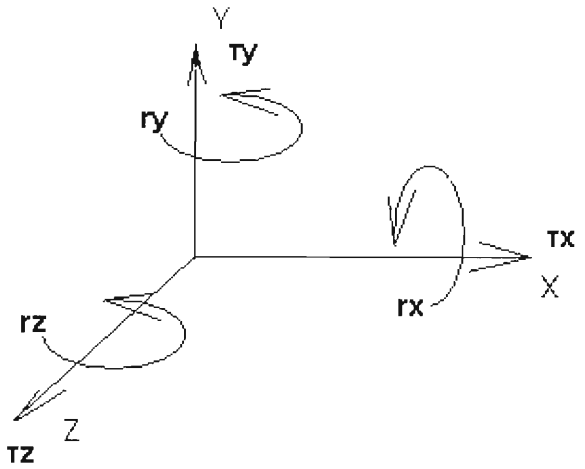

Figure A.1. The 6 degrees of freedom of a vessel and their orientation, the X and Y axis are lying at the sea level with the Z axis rising up perpendicular to the sea.

Initially from the GPS antenna one can calculate the 'Northings' and 'Eastings' at the fairlead center line from Equation (A.1)

$$\begin{pmatrix} \tau_x \\ \tau_y \end{pmatrix}_{GPS} = \begin{bmatrix} \cos(r_z) & -\sin(r_z) \\ \sin(r_z) & \cos(r_z) \end{bmatrix} \begin{bmatrix} Northings* \\ Eastings* \end{bmatrix} - \begin{bmatrix} \sin(r_x) \\ \sin(r_y) \end{bmatrix} h \qquad \text{(A.1)}$$

where h is the relative height of the antenna with respect to the fairlead center line.

Accelerometers provide the surge sway and heave acceleration and can be integrated twice and be translated to the fairlead center line. That is,

$$\begin{bmatrix} \tau_x \\ \tau_y \\ \tau_z \end{bmatrix} = \iint \begin{bmatrix} \ddot{\tau}_x \\ \ddot{\tau}_y \\ \ddot{\tau}_z \end{bmatrix} dt^2 + \begin{bmatrix} \cos(r_z) & -\sin(r_z) & 0 \\ \sin(r_z) & \cos(r_z) & 0 \\ 0 & 0 & 1 \end{bmatrix} \begin{bmatrix} 1 & 0 & 0 \\ 0 & \cos(r_x) & -\sin(r_x) \\ 0 & \sin(r_x) & \cos(r_x) \end{bmatrix} \begin{bmatrix} \cos(r_y) & 0 & -\sin(r_y) \\ 0 & 1 & 0 \\ \sin(r_y) & 0 & \cos(r_y) \end{bmatrix} \vec{r}_p$$

(A.2)

where, the vector $\vec{r}_p$ is the relative position of the fairlead centerline with respect to the accelerometers' position. Integration in time can be done in the frequency domain using multiplication. The translations are obtained from the fidelity region of each instrument and yield

$$\mathbb{F}\begin{Bmatrix}\tau_x\\ \tau_y\\ \tau_z\end{Bmatrix} = \mathbb{F}\begin{Bmatrix}\tau_x\\ \tau_y\\ \tau_z\end{Bmatrix}_{GPS\ for\_f\in(0,f_{ac})} + \mathbb{F}\begin{Bmatrix}\tau_x\\ \tau_y\\ \tau_z\end{Bmatrix}_{Accelerometers\ for\_f\in(f_{ac},f_{niquist})} \tag{A.3}$$

where F denotes the Fourier transform. f_{ac} is the given frequency up to which the GPS provides accurate measurements and beyond that value accelerometers are considered more accurate. Thus,

$$\begin{Bmatrix}\tau_x\\ \tau_y\\ \tau_z\end{Bmatrix} = \mathbb{F}^{-1}\left\{\mathbb{F}\begin{Bmatrix}\tau_x\\ \tau_y\\ \tau_z\end{Bmatrix}\right\}. \tag{A.4}$$

Equation (A.4) provides the fused Fourier transform of the surge sway and heave and is given in terms of the inverse Fourier transform. Fairlead displacements can be obtained from Equation (A.2) using the appropriate $\vec{r}_p$ vector corresponding to each fairlead with respect to the fairlead centerline.

Appendix B: Spatial Discretization of Partial Integrodifferential Equations (PIDE) Using Radial Basis Functions (RBF)

B.1: Numerical integration for stiffness determination

For elements that do not include fracture or any kind of discontinuity the integrations of Equation (4.33) are carried out by Gaussian quadrature using 2x2 points. Figure (B.1.1) shows the Gaussian quadrature points.

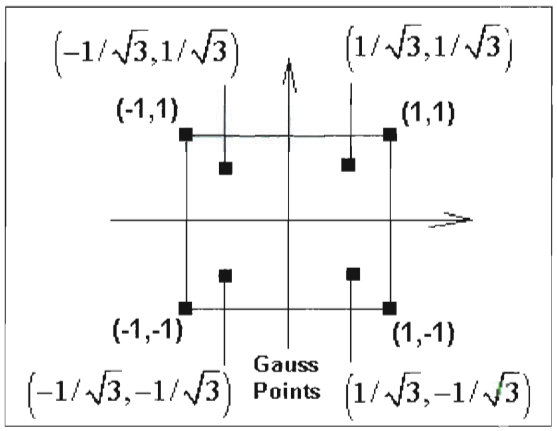

Figure B.1.1 Gaussian quadrature of 2x2 points of weight 1

Integrating function $f(r,\theta)$ on a 2-D rectangular domain $H=[\theta_1,\theta_2]x[r_1,r_2]$ yields

$$\int_{r_1}^{r_2}\int_{\theta_1}^{\theta_2} f(r,\theta)drd\theta = \frac{r_2-r_1}{2}\frac{\theta_2-\theta_1}{2}\int_{-1}^{1}\int_{-1}^{1} f\left(\frac{r_2-r_1}{2}\hat{r}+\frac{r_2+r_1}{2},\frac{\theta_2-\theta_1}{2}\hat{\theta}+\frac{\theta_2+\theta_1}{2}\right)d\hat{r}d\hat{\theta}\,. \tag{B.1.1}$$

Applying Gaussian quadrature of 2x2 points for the numerical integration of equation (B.1.1) yields

$$\int_{r_1}^{r_2}\int_{\theta_1}^{\theta_2} f(r,\theta)drd\theta = \frac{r_2-r_1}{2}\frac{\theta_2-\theta_1}{2}\sum_{i,j=1}^{2}\left(\frac{r_2-r_1}{2}\hat{r}_i + \frac{r_2+r_1}{2}, \frac{\theta_2-\theta_1}{2}\hat{\theta}_i + \frac{\theta_2+\theta_1}{2}\right).$$

(B.1.2)

Next, for elements including fracture and discontinuity, numerical integration on a refined grid of points is needed. Figure (B.1.2) shows an example of a refined grid.

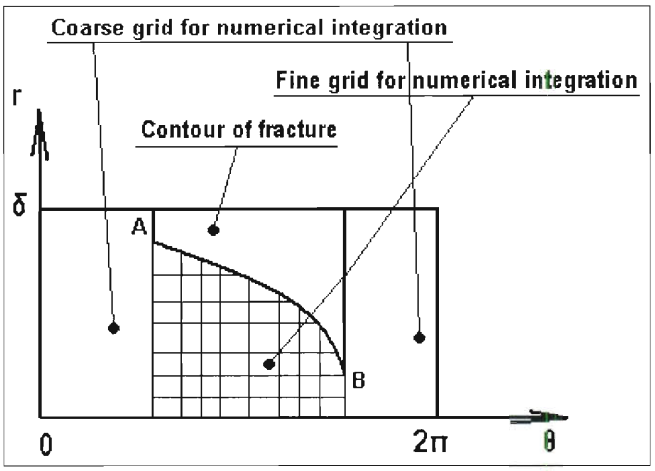

Figure B.1.2. Refined discretization for the numerical evaluation of the stiffness density of a fractured element

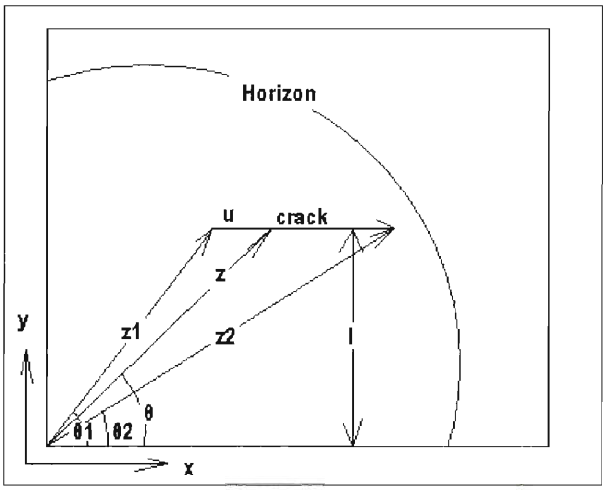

Figure B.1.3 Determination of the fractured contour of a cracked element

The accurate determination of the fracture contour in polar coordinates is considered herein and specifically the determination of the curve AB shown in Figure (B.1.2). For elucidation purposes consider an initial crack shown in Figure (B.1.3). Next, the position of the initial crack is known, therefore the vectors shown in Figure (B.1.3) can be obtained, $\underline{z}_1$, $\underline{z}_2$ are the vectors from the node of interest to the crack tips and $\underline{u}$ is the vector aligned with the crack with orientation from one crack tip to the other. The tangent of the angle of a vector $\underline{z}$ shown in Figure (B.1.3) is given by

$$\tan\theta(a) = \frac{l}{\left(|\underline{z}_1|\cos\theta_1 + a|\underline{u}|\right)}, \tag{B.1.3}$$

where a is a coefficient such that $\alpha \in [0,1]$. Next, the partial derivative of Equation (B.1.3) with respect to the coefficient α yields

$$\frac{d\theta}{d\alpha}\frac{1}{\cos^2\theta(a)} = -\frac{l|\underline{u}|}{\left(|\underline{z}_1|\cos\theta_1 + a|\underline{u}|\right)^2}. \tag{B.1.4}$$

Carrying out the calculations, yields a simplified expression for Equation (B.1.4) as

$$d\theta = -\frac{l|\underline{u}|}{\left(|\underline{z}_1|\cos\theta_1 + a|\underline{u}|\right)^2 + l^2}d\alpha. \tag{B.1.5}$$

Obviously, as the vector $\alpha \bullet \vec{u}$ approaches the crack tip on the right, the rate of the angle is changing. Thus, the curve AB shown in Figure (B.1.2) is obtained numerically by fixing the dα value. Specifically, for a certain $d\alpha$ value, a_j is defined as

$$a_j = j \cdot d\alpha, \tag{B.1.6}$$

where $j = 1,..,1/d\alpha$ and thus $d\theta_j$ is defined as

$$d\theta_j = -\frac{l|\underline{u}|}{\left(|\underline{z}_1|\cos\theta_1 + a_j|\underline{u}|\right)^2 + l^2} d\alpha. \tag{B.1.7}$$

Numerically integrating Equation (B.1.7) by fixing $d\alpha$ yields

$$\theta_j = \theta_1 - \sum_j \frac{l|\underline{u}|}{\left(|\underline{z}_1|\cos\theta_1 + a_j|\underline{u}|\right)^2 + l^2} d\alpha. \tag{B.1.8}$$

Next, the corresponding length r_j to the angle θ_j shown in Figure (B.1.2) yields

$$r_j = \left|\underline{z}_1 + a_j\underline{u}\right|. \tag{B.1.8}$$

In this way the curve AB is obtained as points θ_j and r_j for $\alpha_j \in [0,1]$, and thus, the contour of integration is determined for the numerical integration. For elucidation purposes, points A and B in Figure (B.1.2) correspond to the crack tips $\underline{z}_2$ and $\underline{z}_1$ shown in Figure (B.1.3). In the same way Equation (4.34) is numerically evaluated for elements including cracks. However, for healthy elements, polynomial functions q, and micro-modulus function shown in Equation (4.31), the integration has closed form solution. Specifically, consider the first four linear functions of the FEM as the q functions

$$\begin{aligned} q_1(\underline{x}) &= 1 \\ q_2(\underline{x}) &= x \\ q_3(\underline{x}) &= y \\ q_4(\underline{x}) &= xy \end{aligned}. \tag{B.1.9}$$

Combining Equation (4.29), (4.34) and Equation (B.1.9) yields

$$K_Q = c\int_0^{\delta}\left[\int_0^{2\pi}\begin{bmatrix}\cos^2\theta & \cos\theta\sin\theta\\ \cos\theta\sin\theta & \sin^2\theta\end{bmatrix}\begin{bmatrix}0 & r\cos\theta & r\sin\theta & (x+r\cos\theta)(y+r\sin\theta)-xy\end{bmatrix}d\theta\right]dr$$

(B.1.10)

expanding Equation (B.1.10) yields

$$K_Q = c\begin{bmatrix}K_{Q1} & K_{Q2} & K_{Q3} & K_{Q4}\end{bmatrix}, \tag{B.1.11}$$

where

$$K_{Q1} = \begin{bmatrix}0 & 0\\ 0 & 0\end{bmatrix}, \tag{B.1.12}$$

$$K_{Q2} = \begin{bmatrix}\dfrac{\cos^2\theta\sin\theta}{3}+\dfrac{2\sin\theta}{3} & -\dfrac{\cos^3\theta}{3}\\ -\dfrac{\cos^3\theta}{3} & \dfrac{\sin^3\theta}{3}\end{bmatrix}\Bigg|_0^{2\pi}\frac{r^2}{2}\Bigg|_0^{\delta}, \tag{B.1.13}$$

$$K_{Q3} = \begin{bmatrix}-\dfrac{\cos^3\theta}{3} & \dfrac{\sin^3\theta}{3}\\ \dfrac{\sin^3\theta}{3} & \dfrac{\cos\theta\sin^2\theta}{3}-\dfrac{2\cos\theta}{3}\end{bmatrix}\Bigg|_0^{2\pi}\frac{r^2}{2}\Bigg|_0^{\delta}, \tag{B.1.14}$$

and finally

$$K_{Q4} = \begin{bmatrix}-\dfrac{\cos^4\theta}{4} & -\dfrac{\sin^2\theta\cos^3\theta}{4}+\dfrac{\theta}{8}+\dfrac{\sin 2\theta}{16}\\ -\dfrac{\sin^2\theta\cos^3\theta}{4}+\dfrac{\theta}{8}+\dfrac{\sin 2\theta}{16} & \dfrac{\sin^4\theta}{4}\end{bmatrix}\Bigg|_0^{2\pi}\frac{r^3}{3}\Bigg|_0^{\delta} + xK_{Q3} + yK_{Q2}.$$

(B.1.15)

Equivalently, for K_Q^1, the matrix yields

$$K_Q^1 = \int_0^{\delta}\left[\int_0^{2\pi}\begin{bmatrix}\cos^4\theta\sin^2\theta & \cos^3\theta\sin^3\theta\\ \cos^3\theta\sin\theta & \sin^4\theta\cos^2\theta\end{bmatrix}\begin{bmatrix}0 & r\cos\theta & r\sin\theta & (x+r\cos\theta)(y+r\sin\theta)-xy\end{bmatrix}d\theta\right]dr$$

(B.1.16)

expanding Equation (B.1.16) yields

$$K_Q^1 = \begin{bmatrix} K_{Q1}^1 & K_{Q2}^1 & K_{Q3}^1 & K_{Q4}^1 \end{bmatrix} \tag{B.1.17}$$

where

$$K_{Q1}^1 = \begin{bmatrix} 0 & 0 \\ 0 & 0 \end{bmatrix}, \tag{8.1.18}$$

$$K_{Q2}^1 = \left[\begin{matrix} \frac{\sin^3(\theta)}{840}(157+108\cos(2\theta)+15\cos(4\theta) & \frac{\cos^5(\theta)}{70}(-9+5\cos(2\theta)) \\ \frac{\cos^5(\theta)}{70}(-9+5\cos(2\theta)) & \frac{\sin^5(\theta)}{70}(9+5\cos(2\theta) \end{matrix} \right]_0^{2\pi} \left. \frac{r^2}{2} \right|_0^{\delta}, \tag{8.1.19}$$

$$K_{Q3}^1 = \left[\begin{matrix} \frac{\cos^5(\theta)}{70}(-9+5\cos(2\theta)) & \frac{\sin^5(\theta)}{70}(9+5\cos(2\theta) \\ \frac{\sin^5(\theta)}{70}(9+5\cos(2\theta) & -\frac{\cos^3(\theta)}{840}(157-108\cos(2\theta)+15\cos(4\theta)) \end{matrix} \right]_0^{2\pi} \left. \frac{r^2}{2} \right|_0^{\delta}, \tag{8.1.20}$$

and finally

$$K_{Q4}^1 = \left[\begin{matrix} \frac{1}{10240}(120\theta+20\sin(2\theta)-40\sin(4\theta) & -\frac{5\cos(2\theta)}{512}+\frac{5\cos(6\theta)}{3072}-\frac{\cos(10\theta)}{5120} \\ -10\sin(6\theta)+5\sin(8\theta)+2\sin(10\theta)) & \\ -\frac{5\cos(2\theta)}{512}+\frac{5\cos(6\theta)}{3072}-\frac{\cos(10\theta)}{5120} & \frac{1}{10240}(120\theta-20\sin(2\theta)-40\sin(4\theta) \\ & +10\sin(6\theta)+5\sin(8\theta)-2\sin(10\theta)) \end{matrix} \right]_0^{2\pi} \left. \frac{r^3}{3} \right|_0^{\delta} + xK_{Q3}^1 + yK_{Q4}^1 \tag{8.1.21}$$

B.2: Kansa collocation method

The Kansa collocation method in 1-D for a set of $N = L/\Delta x + 1$ equally spaced grid points of distance Δx, yields the equations in the following form

$$\begin{bmatrix} u(0) \\ u(\Delta x) \\ u(2\Delta x) \\ \dots \\ 0 \\ 0 \end{bmatrix} = \begin{bmatrix} g_1(0) & g_1(0) & \dots & g_N(0) & q_0(0) & \dots \\ g_1(\Delta x) & g_1(\Delta x) & \dots & g_N(\Delta x) & q_0(\Delta x) & \dots \\ g_1(2\Delta x) & g_1(2\Delta x) & \dots & g_N(2\Delta x) & q_0(2\Delta x) & \dots \\ \dots & \dots & \dots & \dots & \dots & \dots \\ q_1(0) & q_1(\Delta x) & q_1(2\Delta x) & \dots & 0 & 0 \\ \dots & \dots & \dots & \dots & 0 & 0 \end{bmatrix} \begin{bmatrix} a_{11} \\ a_{12} \\ \dots \\ a_{1N} \\ a_{21} \\ \dots \end{bmatrix}. \tag{B.2.1}$$

The last M rows represent the regularization equations of the coefficients which state that

$$\sum_{k=1}^{N} q_j(\underline{x}_k) d_{2k} = 0 \text{ and } \sum_{k=1}^{N} q_j(\underline{x}_k) d_{2k} = 0 \text{ for j=1...M,} \tag{B.2.2}$$

where M is the number of the additional basis functions q.

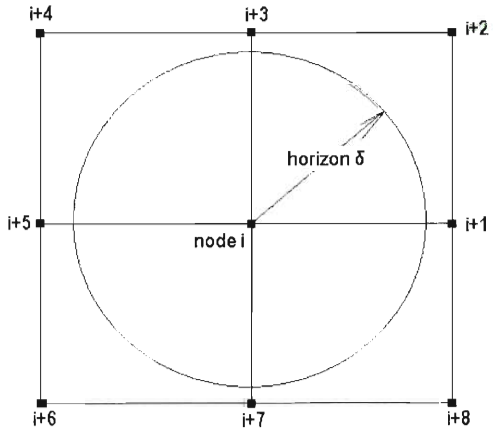

Figure B.2.1. The horizon of one node over four elements, the stiffness density of the node i is calculated through Equations (4.33) and (4.34)

Assuming that the displacements of a point in the domain of Figure B.2.1 can be approximated by the adjacent nodes, Equation (4.26) yields the displacement for a point inside the upper right square and yields

$$\begin{aligned} u(\underline{x}_i + \underline{r}) &= \sum_{k=i}^{i+3} a_{1k} g_k(\underline{x}_i + \underline{r}) + \sum_{j=1}^{M} a_{2j} q_j(\underline{x}_i + \underline{r}) \\ v(\underline{x}_i + \underline{r}) &= \sum_{k=i}^{i+3} d_{1k} g_k(\underline{x}_i + \underline{r}) + \sum_{j=1}^{M} d_{2j} q_j(\underline{x}_i + \underline{r}) \end{aligned} \quad . \qquad \text{(B.2.3)}$$

Figure (B.2.2) shows the IMQ function for the same node, both for a 'healthy' and a cracked four node element. It can be seen that the visibility criterion is applied on the cracked element since the crack disrupts the horizon of the node.

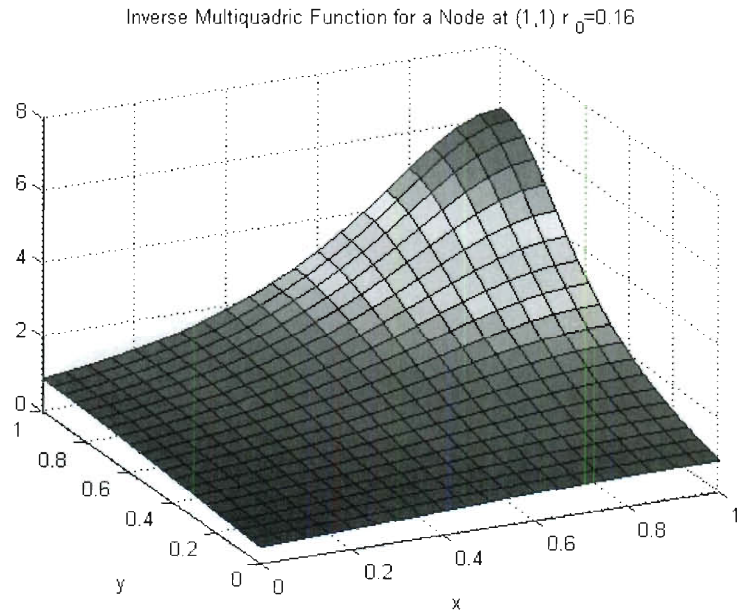

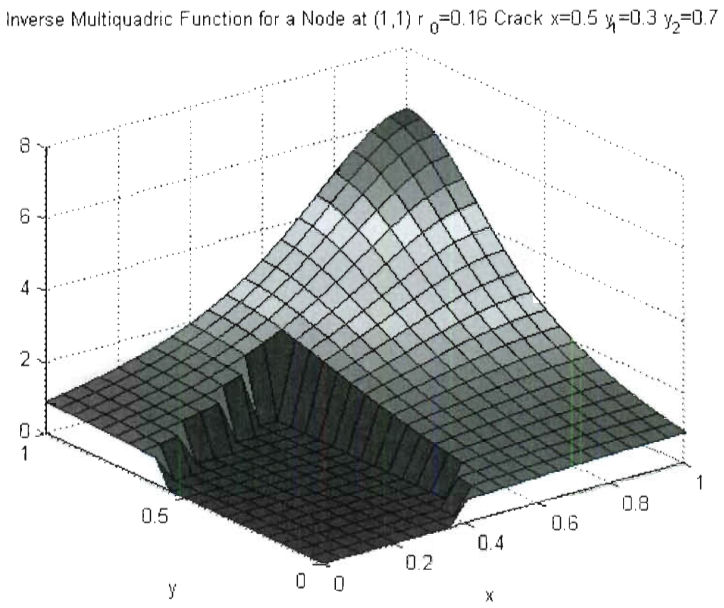

Figure B.2.2. The IMQ basis function of the corresponding node on a four node element with and without crack inside the horizon

B.3: Linearized pair-wise force-function

The linearized pair-wise force-function as introduced in [1] imposes an implicit assumption of small rigid body rotations. Specifically, consider Equation (4.12) that defines the stretch of a bond. Carrying out the calculations yields

$$s = \left| 1 + \frac{\underline{\eta}}{\underline{\xi}} \right| - 1. \tag{B.3.1}$$

Next, using complex notation of the vectors yields

$$\underline{\eta} = \left|\underline{\eta}\right| \left(\cos\theta_{\eta} + i \sin\theta_{\eta} \right), \tag{B.3.2}$$

and

$$\underline{\xi} = \left|\underline{\xi}\right| \left(\cos\theta_{\xi} + i \sin\theta_{\xi} \right), \tag{B.3.3}$$

where θ_η, θ_ξ are the angles of the vectors with respect the orthogonal reference system. Figure (B.3.1) helps elucidate the concept. Next, combining (B.3.2) and (B.3.3) yields

$$\frac{\underline{\eta}}{\underline{\xi}} = \frac{|\underline{\eta}|}{|\underline{\xi}|}\left(\cos\left(\theta_\eta - \theta_\xi\right) + i\sin\left(\theta_\eta - \theta_\xi\right)\right). \tag{B.3.4}$$

Obviously the angles of the vectors determine if the vector division yields a vector or a scalar. For the case of

$$\theta_\eta \simeq \theta_\xi, \tag{B.3.5}$$

Equation (B.3.4) yields

$$\frac{\underline{\eta}}{\underline{\xi}} \simeq \frac{|\underline{\eta}|}{|\underline{\xi}|}, \tag{B.3.6}$$

and Equation (B.3.1) becomes

$$s \simeq \frac{|\underline{\eta}|}{|\underline{\xi}|}. \tag{B.3.7}$$

Equation (B.3.7) implicitly assumes that the deformation of the bond is collinear with the bond's initial orientation or that the bond exhibits small rotation which can be neglected.

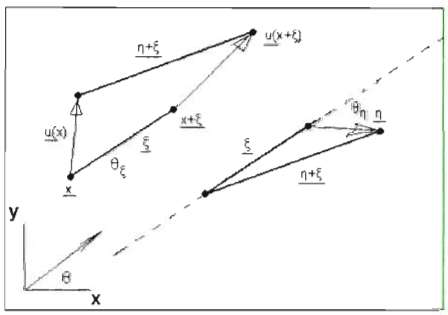

Figure B.3.1. One bond before and after deformation

References

Nutting PG (1921) '*A new general law deformation*', Journal of the Franklin Institute 191:678-685.

Scott-Blair GW, Gaffyn JE (1949) '*An application of the theory of quasi-properties to the treatment of anomalous strain-stress relations*', The philosophical Magazine 40:80-94.

Caputo M (1974) '*Vibrations on an infinite viscoelastic layer with a dissipative memory*', Journal of the Acoustical Society of America 56(3):897-904.

Bagley RL, Torvik PJ (1986) '*On the fractional calculus model of viscoelastic behavior*', Journal of Rheology 30(1):133-155.

Almeida LB (1994) '*The fractional Fourier transform and time frequency representation, IEEE Trans*', Signal Processing 42:3084-3091.

Namias V (1998) '*The fractional order fourier transform and its application to the quantum mechanics*', Journal of the Institute of Mathematics and its Applications 25:241-265.

Pei SC, Yeh MH, Tseng CC (1999) '*Discrete fractional Fourier transform based on orthogonal projections*', IEEE Transactions Signal Processing 47:1335-1348.

Barnsley MF *(1988) 'Fractals everywhere*', Academic Boston.

Chao M, Nikias CL (1993) '*Signal processing with fractional lower order moment: Stable processes and their applications*', Proceedings IEEE 81:986-1010.

Galucio AC, Deu JF, Ohayon R (2004) '*Finite element formulation of viscoelastic sandwich beams using fractional derivative operators*', Computational Mechanics 33:282-291

Bossemayer H (2001) '*Evaluation technique for dynamic moduli*', Mechanics Time-Dependent Materials 5:273-291.

Adolfsson K, Enelund M, Olson P (2005) '*On the fractional order model of viscoelaticity*', Mechanics Time-Dependent Materials 9:15-24.

Lu CY (2006) '*Fractional derivative viscoelastic model for frequency-dependent compex moduli of automotive elastomers*', International Journal of Mechanics and Materials in Design 3:329-336.

Enelund M, Olsson P (1999) '*Damping described by fading memory analysis and application to fractional derivative models*', International Journal of Solid and Structures 36:939-970.

Zaid O (2006) '*Approximations of fractional integrals and Caputo fractional derivatives*', Applied Mathematics and Computation 178:527-533.

Murio DA (2006) '*On the stable numerical evaluation of Caputo fractional derivatives*', Computers and Mathematics with Applications 51:1539-1550.

Schmidt A, Gaul L (2002) '*Finite element formulation of viscoelastic constitutive equations using fractional time derivatives*', Non Linear Dynamics 29:37-55.

Podlubny PA (1999) '*On Solving fractional differential equations'*, Mathematics in Science and Engineering volume 198, Academic Press.

Gemant A (1936) '*A method of analyzing experimental results obtained by elasto-viscous bodies*', Physics 7:311-317.

Gemant A (1938) '*On fractional differentials*', The Philosophical Magazine 25:540-549.

Grunwald, A (1867) '*Uber begrenzte derivationen und deren anwendung*', Zeitschrift fur Angewandte Mathematik und Physik 12:441-480.

Gerolymatou E, Vardoulakis I, Hilfer R (2006) '*Modeling infiltration by means of a non linear fractional diffusion model*', Journal of Physics, Applied Physics 39:4104-4110.

Makris N, Dargush GF, Constantinou MC (1993) '*Dynamic analysis of generalized viscoelastic fluid'*, Journal of Engineering Mechanics 119(8).

Hwang JS, Wang JC (1998) '*Seismic response prediction of high damping rubber bearings fractional derivative Maxwell model*', Engineering Structures 20(9):849-856.

Koh CG, Kelly LM (1990) '*Application of fractional derivatives to seismic analysis of base isolated models*', Earthquake Engineering and Structural Dynamics 19(2): 229-241.

Makris N (1994) '*Complex parameter Kelvin model for elastic foundations*', Earthquake Engineering and Structural Dynamics 23:251-264.

Makris N, Constantinou MC (1991) '*Fractional derivative Maxwell model for viscous dampers*', Journal of Structural Engineering ASCE 117(9):2708-2724.

Oldham KB and Spanier J. '*The fractional Calculus*', Mathematics in Science and Engineering, Vol III Academic Press, New York N.Y.

Makris N, Constantinou MC. '*Viscous dampers: Testing, modeling and application in vibration and seismic isolation*', Technical report NCEER-90-0028. National Center for Earthquake Engineering Research. State University of New York at Buffalo.

Katsikadelis JT (2009) '*Numerical solution of multi term fractional differential equations*', Journal of Applied Mathematics and Mechanics ZAMM 89(7):593-608. Wiley.

Rossikhin YA, Shitikova MV (2001) '*A new method for solving dynamic problems of fractional derivative viscoelasticity*', International Journal of Engineering Science 39:149-176.

Fukunaga M, Shimizu N (2004) '*Analytical and numerical solutions for fractional viscoelastic equations*', International Journal of Japan Society of Mechanical Engineering 47(1):251-259.

Ochmann M, Malakov S (1993) '*Representations of the absorption of nonlinear waves by fractional derivatives*', Journal of American Acoustical Society 94(6):3392-3401.

Zhang W, Shimizu N (1999) '*Damping properties of the viscoelastic material described by fractional Kelvin-Voigt model*', International Journal of Japan Society of Mechanical Engineers 42(1):1-9.

Trigeassou JC, Maamri N (2011) '*Initial conditions and initialization of linear fractional differential equations*', Signal Processing 91:427-436.

Kenneth S. Miller and Bertram Ross (1993) '*An Introduction to Fractional Calculus and Fractional Differential Equations*', John Wiley & Sons.

Spanos PD, Evangelatos (2010) *'Response of a non linear system with damping forces governed by fractional derivatives-Time domain simulation and statistical linearization solution',* Soil Dynamics and Earthquake Engineering 30:811-821.

Childres MA (1973) '*Mooring Systems for hostile waters*', Petroleum Engineer 58-70.

Childres MA (1974) '*Deep water mooring part I, environmental factors control station keeping methods*', Petroleum Engineer 10:36-58.

Childres MA (1974) '*Deep water mooring part II, the ultra deep water spread mooring system*', Petroleum Engineer 2:108-118.

Childres MA (1975) '*Deepwater mooring part part III, equipment for handling the ultra deep water spread mooring system*', Petroleum Engineer 5:114-132.

Niedwecki TE, Casarella MJ (1975) '*On the design of mooring lines for deep water applications*', ASME No 75-WA/OCE-1.

Nath JH, Felix MP (1970) '*Dynamics of single point mooring in deep water*', J. Waterways, Harbours & Costal Engineering Div. Proc ASCE 815-853.

Wilson BW, Garbaccio DH (1969) '*Dynamics of ship anchor-lines in waves and currents*', J Waterways & Harbors Div. Proc ASCE 449-465.

Peyrot AH. Goulois AM (1979) '*Analysis of cable structures*', Computers and Structures 10:805-813.

Tuah H, Leonard JW (1990) '*Dynamic response of viscoelastic cable elements*', Ocean Engineering 17(1.2):23-34.

Ansari KA, Khan NU (1986) '*The effect of cable dynamics on the station keeping response of a moored offshore vessel*', ASME Journal of Energy Resources Technology 108:52-58.

Remery GFM, Van Oortmersson G (1973) '*The mean wave, wind and current forces on offshore structures and their role in the design of mooring systems*', Proceedings of The Offshore Technology Conference, Houston Paper OTC-1741:1169-1184.

Olsen OA, Loken AE, Namork J (1981) '*On the effects of non linearities in mooring of offshore structures- the use of physical models in their design, GST*', Armer and FK. Gores The Constant Press 239-249.

Chakrabarty SK. (1987) '*Hydrodynamics of offshore structures*', Computational Mechanics Publications: Springer-Verlag 4:86-127.

Wilson JF (1984) '*Dynamics of offshore structures*', John Wiley Publications 6:154-177.

Schellin TE, Scharrer M, Mathies HG (1982) '*Analysis of vessel moored in shallow unprotected waters*', Offshore Technology Conference OTC-4243 May.

Mehernosh BI, Johnson RP, Emmett GW (2001) '*FPSO responses to wind, wave and current loading*', Proceedings of OMAE 2001 June OFT-1023.

Kim MH, Ran Z, Zheng W (2001) '*Hull mooring coupled dynamic analysis of a truss in time domain*', International Journal of Offshore and Polar Engineering Vol 11 March 2001.

Minsuk K, Zun Z, Yu D (2004) '*Numerical simulation of a spar interacting with polyester mooring system'*, OMAE 5122. Proceedings of the 23rd International Conference on Offshore Mechanics and Arctic Engineering. Vancouver, British Columbia.

Hooker J, Bosman RLM (1999) '*The elastic modulus characteristic of polyester mooring rope'*, Proceedings of the Offshore Technology Conference OTC10779, Houston TX.

Flory JF (1999) *'Deep star CTR-4400 vessel risers and moorings: taut leg mooring polyester rope test program*', Technical Report, Tension Technology International, Morristown New Jersey.

Petruska D, Geyer J, Macon R, Craig M, Ran A, Schulz N (2005) '*Polyester mooring for the mad dog spar design issues and other considerations*', Ocean Engineering 32:767-782.

Herbich JB. '*Developments in offshore engineering with wave phenomena and offshore topics*', Gulf Publishing Company 1999 Houston, Texas.

Faltinsen QM (1990) '*Sea loads on ships and offshore structures'*, Ocean Technology Series, Cambridge University Press 2,3:13-101.

Nocedal J. Wright SJ. '*Numerical Optimization*', Springer Series in Operations Research, Springer 2nd Edition.

Chopra AK (1995) *'Dynamics of Structures, Theory and Applications to Earthquake Engineering'*, Prentice Hall, New Jersey 07632.

Casey NF, Banfield SJ. (2005) '*Factors affecting the measurement of axial stiffness of polyester deepwater mooring rope under sinusoidal loading*', Offshore Technology Conference, 2-5 May 2005 Houston Tx, USA.

Fernandes AC, Del Vecchio CJM, Castro GAV (1999) '*Mechanical properties of polyester mooring cables*', International Journal of Offshore and Polar Engineering vol 9 No 3 September 1999.

Fernandes AC, Rossi RR (2005) '*Distorted polyester lines for model testing of offshore moored platforms*', Ocean Engineering 32:817-825.

Huntley M. Polyester mooring rope: *Length determination and static modulus*. IEEE 2006

Crudu LI, Obreja DC, Stoicescu LD (1997) '*Experimental research on the dynamic behavior of mooring lines*', OMAE 1997 vol I-A Offshore Technology ASME 1997

Fernandes AC, Rossi RR (2002) '*On the model scaling of polyester mooring lines for offshore applications*', OMAE 2002-28547, 23-28 Oslo Norway.

Tahar A, Kim MH (2008) '*Coupled-dynamic analysis of floating structures with polyester mooring lines*', Ocean Engineering 35:1676-1685.

Kim M. Ding Y. (2004) '*Numerical simulation of a spar interacting with polyester mooring system*', OMAE 2004-51222, June 20-25 Vancouver British Colombia.

Silling SA. (2000) '*Reformulation of elasticity theory for discontinuities and long range forces*', Journal of the Mechanics and Physics of Solids 48:175-209.

Silling SA, Zimmermann M, Abeyaratne R (2003) '*Deformation of a peridynamic bar*', Journal of Elasticity 73:173-190.

Silling SA, Epton M, Weckner O, Xu J, Askari E. (2007) '*Peridynamic states and constitutive modeling*', Journal of Elasticity 88:151-184.

Bobaru F, Yang M, Alves LF, Silling SA, Askari E, Xu J (2009) '*Convergence adaptive refinement and scaling in 1D peridynamics*', International Journal for Numerical Methods in Engineering 77:852-877.

Warren TL, Silling SA, Askari A, Weckner O, Epton MA, Xu J (2009) '*A non ordinary state based peridynamic method to model solid material deformation and fracture*', International Journal of Solids and Structures 46:1186-1195.

Macek RW, Silling SA (2007) '*Peridynamics via finite element analysis*', Finite Elements Analysis and Design 43:1169-1178.

Bobaru F (2007) '*Influence of Van der Waals forces on increasing the strength and toughness in dynamic fracture of nano-fiber networks: a*

peridynamic approach', Modelling and Simulation in Materials Science and Engineering 15:397-417.

Silling SA, Askari E (2005) '*A mesh-free method based on the peridynamic model of solid mechanics*', Computers and Structures 83:1526-1535.

Belytchko T, Lu YY, Gu L (1995) '*Crack propagation by element-free Galerkin methods*', Engineering fracture mechanics 51(2):295-315

Belytchko T, Gu L, Lu YY (1994) '*Fracture and crack growth by element-free Galerkin methods*', Modeling and Simulation in Material Science and Engineering 2:519-534.

Kroner E (1967), '*Elasticity theory of materials with long range cohesive forces*', International Journal of Solids and Structures 3:731-742.

Eringen EC, Speziale CG, Kim BS (1977) '*Crack tip problem in non local elasticity*', Journal of Mechanics and Physics of Solids 25:339-355.

Edelen DGB (1969) '*Non-local variational mechanics-I, stationarity conditions with one unknown'*, International Journal of Engineering Sciences 7:269-285.

Edelen DGB (1969) '*Non-local variational mechanics-II, properties of the non local Lagrange operator'*, International Journal of Engineering Sciences 7:287-293.

Edelen DGB (1969) '*Non-local variational mechanics-III, linear operators and variational imbedding with one unknown'*, International Journal of Engineering Sciences 7:373-389.

Edelen DGB (1969) '*Non-local variational mechanics-IV, stationarization with several dependent variables'*, International Journal of Engineering Sciences 7:391-399.

Edelen DGB (1969) '*Non-local variational mechanics-V,variational imbedding adjoint theorem and existence'*, International Journal of Engineering Sciences 7:401-415.

Edelen DGB (1969) '*Non-local variational mechanics-VI, momentum energy invariance and integration'*, International Journal of Engineering Sciences 7:677-688.

Edelen DGB (1969) '*Non-local variational mechanics-VII, stationarization with constrains'*, International Journal of Engineering Sciences 7:843-847.

Edelen DGB (1970) '*Non-local variational mechanics-VIII, unrestricted non locality'*, International Journal of Engineering Sciences 8:517-520.

Edelen DGB (1975) '*Non-local variational mechanics-IX, lagrangians with multiple interactions'*, International Journal of Engineering Sciences 13:861-867.

Emmrich E, Weckner O (2007) '*The peridynamic equation and its spatial discretization*', Mathematical Modelling and Analysis 12:17-27.

Fleming M, Chu YA, Moran B, Belytschko T (1997), '*Enriched element-free Galerkin methods for crack tip fields*', International journal for numerical methods in engineering 40:1483-1504.

E.E. Gdoutos (1990) '*Fracture Mechanics Criteria and Applications'*, Kluwer Academic Publishers.

Emmrich E, Weckner O (2007), '*On the well-posedness of the linear peridynamic model and its convergence towards the Navier equation of linear elasticity*', Communications in Mathematical Sciences 5(4):851-864.

Zi G, Belytschko T (2003), *'New crack tip elements for X-FEM and applications to cohesive cracks'*, International Journal of Numerical Methods in Engineering 57(15):2221-2240.

Zhou K, Du Q (2010), *'Mathematical and numerical analysis of linear peridynamic models with non local boundary conditions'*, Society for Industrial and Applied Mathematics 48 (5) 1759-1780.

Wei P, Wang MY, Xing X. (2010) '*A study on X-FEM in continuum structural optimization using level set model'*, Computer Aided Design 42:708-719.

DiPaola M, Faila G, Zingales M (2009) '*Physically based approach to the mechanics of strong non local linear elasticity theory'*, Journal of Elasticity 97:103-130.

DiPaola M, Zingales M (2008) '*Long range cohesive interactions of non-local continuum faced by fractional calculus'*, International Journal of Solids and Structures 45:5642-5659.

Faila G, Santini A, Zingales M (2010) '*Solution for 1D elastic continuum with long-range interactions smooth and fractional decay'*, Mechanics Research Communications 37:13-21.

Bazant ZP, Novak D (2000) *'Probabilistic nonlocal theory for quasibrittle fracture initiation and size effect. I:Theory'*, Journal of Engineering Mechanics 126(2):166-174.

Bazant ZP, Novak D (2000) *'Probabilistic nonlocal theory for quasibrittle fracture initiation and size effect. II:Application'*, Journal of Engineering Mechanics 126(2):175-185.

Bazant ZP, Giraudon EB (2001) *'Statistical prediction of fracture parameters of concrete and implications for choice of testing standard'*, Cement and Concrete Research 12:529-556.

Huang D, Zhang Q, Qiao P (2011) *'Molecular dynamics evaluation of strain rate and size effects on mechanical properties of FCC nickel nanowires'*, Computational Material Science 50:903-910.

Kalinichev AG, Kirkpatrick RJ (2002) *'Molecular dynamics modeling of chloride binding to the surfaces of calcium hydroxide, hydrated calcium aluminate, and calcium silicate phases'*, Chemical Materials, American Chemical Society 15:3539-3549.

Stolarska M, Chopp DL, Moes N, Belytschko T (2001) '*Modeling crack growth by level sets in the extended finite element method'*, International Journal for Numerical Methods in Engineering 51:943-960.

Chessa J, Belytschko T (2004) '*Arbitrary discontinuities in space-time finite element by level sets and X-FEM'*, International Journal for Numerical Methods in Engineering 61:2595-2614.

Belytschko T, Lu YY, Gu L (1994) '*Element-free Galerkin methods*', International Journal for Numerical Methods in Engineering 37:229-256.

Rao BN, Rahman S (2001) '*A coupled meshless finite element method for fracture analysis of cracks'*, International Journal of Pressure Vessels and Piping 78:647-657.

Belytschko T, Organ D, Gerlach C (2000) '*Element free Galerkin methods for dynamic fracture in concrete*', Computational Methods and Applied Mechanics in Engineering 187:385-399.

Ponthot JP, Belytschko T (1998) '*Arbitrary Lagrangian-Eulerian formulation for element free Galerkin method'*, Computational Methods and Applied Mechanics in Engineering 152:19-46.

Vanmarcke R, Grigoriu M (1983) '*Stochastic finite element analysis of simple beams'*, ASCE Journal of Engineering Mechanics 109:22-41.

Der Kiureghian A, Liu PL (1986) '*Structural reliability under incomplete probability information*', ASCE Journal of Engineering Mechanics 112:85-104.

Deodatis G, (1991) '*Weighted integral method. I: stochastic stiffness matrix*', ASCE Journal of Engineering Mechanics 117:1851-1864.

Rahman S, Rao BN (2001) '*A perturbation method for stochastic meshless analysis in elastostatics*', International Journal of Numerical Methods in Engineering 50:1969-1991.

Rahman S, Rao BN (2001) '*An element free Galerkin method for probabilistic mechanics and reliability*', International Journal of Solids and Structures 38:9313-9330.

Rao BN, Rahman S (2002) *'Probabilistic fracture mechanics by Galerkin meshless methods-part I: rates of stress intensity factors'*, Computational Mechanics 28:351-364.

Rahman S, Rao BN (2002) *'Probabilistic fracture mechanics by Galerkin meshless methods-part II: reliability analysis'*, Computational Mechanics 28:365-374.

Rao BN, Rahman S (2003) *'Stochastic meshless analysis of elastic plastic cracked structures'*, Computational Mechanics 32:199-213.

Kansa EJ (1990) *'Multiquadrics-A scattered data approximation scheme with applications to computational fluid dynamics –I'*, Computers and Mathematical Applications 19:127-145.

Kansa EJ (1990) *'Multiquadrics-A scattered data approximation scheme with applications to computational fluid mechanics-II, solutions to parabolic, hyperbolic and elliptic partial differential equations'*, Computers and Mathematical Applications 19:147-161.

Hardy RL (1975) *'Research results in the application of multiquadric equations to surveying and mapping problems'*, Surveying and Mapping 35:321-332.

Micchelli CA (1986) *'Interpolation of scattering data: distance matrices and conditionally positive definite functions'*, Constructive Approximation 2:11-22.

Franke C, Schaback R (1998) *'Convergence order estimates of meshless collocation methods using radial basis functions'*, Advances in Computational Mathematics 8:381-399.

Spanos PD, Ghanem R (1989) '*Stochastic finite element expansion for random media'*, ASCE Journal of Engineering Mechanics 109:1035-1053.

Rao BN, Rahman S (2000) '*An efficient meshless method for fracture analysis of cracks'*, Computational Mechanics 26:398-408.

Arun CO, Rao BN, Shrinivasan SM (2010) '*Stochastic mesh-free method for elastic-plastic damage analysis'*, Computer Methods in Applied Mechanics and Engineering 199:2590-2606.

Ghanem R, Spanos PD (1993) '*A stochastic Galerkin expansion for nonlinear random vibration analysis'*, Probabilistic Engineering Mechanics 8:255-264.

Ghanem R, Spanos PD, (1990) '*Polynomial chaos in stochastic finite elements'*, ASME Journal of Applied Mechanics 57:197-202.

Henry Stark, John W. Woods (2002) '*Probability and random process with applications to signal processing'*, Third Edition Prentice Hall, New Jersey.

Ghanem R, Spanos PD (1991) '*Stochastic finite elements: A spectral approach'*, Springer New York.

Tarwater AE (1985) *'A parameter study of Hardy's multiquadric method for scattered data interpolation'*, UCRL-54670.

Cyron CJ, Nissen K, Gravemeier V, Wall WA (2010) '*Stable mesh-free methods in fluid mechanics based on Green's functions'*, Computational Mechanics 46:287-300.

Xiao JR, Gama BA, Gillespie JW, Kansa EJ (2005) '*Meshless solutions of 2D contact problems by subdomain variational inequality and MLPG method with radial basis functions'*, Engineering Analysis with Boundary Elements 29:95-106.

Sharan M, Kansa EJ, Gupta S (1997) '*Application of the multiquadric method for numerical solution of elliptic partial differential equations'*, Applied Mathematics and Computation 84:275-302.

Ling L, Kansa EJ (2004) '*Preconditioning for radial basis functions with domain decomposition methods,* Mathematical and Computer Modeling 40:1413-1427.

Kansa EJ, Aldredge RC, Ling L (2009) '*Numerical simulation of two-dimensional combustion using mesh-free methods'*, Engineering Analysis with Boundary Elements 33:940-950.

Kansa EJ, Power H, Fasshauer GE, Ling L (2004) '*A volumetric integral radial basis function method for time dependent partial differential equations. I. Formulation'*, Engineering Analysis with Boundary Elements 28:1191-1206.

Kansa EJ, Hon YC (2000) '*Circumventing the ill-conditioning problem with multiquadric radial basis functions: applications to elliptic partial differential equations'*, Computers and Mathematics with Applications 39:123-137.

Kansa EJ (1981) '*An algorithm for multidimensional combusting flow problems'*, Journal of Computational Physics 42:152-194.

Rodenas JJ, Gonzales-Estrada OA, Diez P, Fuenmayor FJ (2010) '*Accurate recovery-based upper error bounds for the extended finite element framework'*, Computer Methods in Applied Mechanics and Engineering 199:2607-2621.

Khoei AR, Taheri-Mousavi SM (2010) '*Modeling of large deformation-large sliding contact via the penalty x-fem technique'*, Computational Materials Science 48:471-480.

Dreau K, Chevaugeon N, Moes N (2010) '*Studied X-FEM enrichment to handle material interfaces with higher order finite element'*, Computer Methods in Applied Mechanics and Engineering 199:1922-1936.

Baietto MC, Pierres E, Gravouil A (2010) '*A multi-model X-FEM strategy dedicated to frictional crack growth under cyclic fretting fatigue loadings'*, International Journal of Solids and Structures 47:1405-1423.

Fedoseyev AI, Friedman MJ, Kansa EJ (2002) *'Improved multiquadric method for elliptic partial differential equations via PDE collocation on the boundary'*, Computers and Mathematics with Applications 43:439-455.

P.D. Spanos and G.I. Evangelatos (2009) *'Response of a Non Linear System with Damping Forces Governed by Fractional Derivatives-Monte Carlo Simulation and Statistical Linearization'*, Symposium on Recent Advances in Mechanics; Athens Greece September 16-19 2009.

P.D. Spanos and G.I. Evangelatos (2010) *'Stochastic Modeling and Uncertainties in Solid Mechanics'*, PACAM XI; Foz do Iguacu PR, Brazil, January 4-8 2010.

G.I. Evangelatos and P.D. Spanos (2010) *'A Multiquadrics Approach in Stochastic Meshless Elastostatics Using Polynomial Chaos Expansion'*, 6th

Computational Stochastic Mechanics Conference; Rhodes Greece June 11-14 2010.

G.I. Evangelatos and P.D. Spanos (2010) *'A Stochastic Collocation Approach on Peridynamic Modeling of Fracture Using Multiquadric Enriched Basis Functions'*, ASCE, Engineering Mechanics Institute (EMI) Conference; University of Southern California, Los Angeles, California 8-11 August 2010.

G.I. Evangelatos and P.D. Spanos (2011) *'A collocation Approach for Spatial Discretization of Stochastic Peridynamics Modeling of Fracture'*, Journal of Mechanics of Materials and Structures, article in press, available online.

G.I. Evangelatos and P.D. Spanos (2011) *'An Accelerated Newmark Scheme for Solving the Equation of Motion in the Time Domain of Systems Comprising Dampers Governed by Fractional Derivatives'*, A.N. Kounadis and E.E. Gdoutos, Recent Advances in Mechanics, Springer Publications.